TABLE OF CONTENTS

Page

Page

Page

# LIST OF TABLES

Table Page

# LIST OF FIGURES

Figure Page

Figure Page

Figure Page

Figure Page

Figure Page

Figure Page

# 1. INTRODUCTION

Automobile noise is one of the most annoying environmental noise problems since the number of automobiles has increased dramatically for the last few decades. It is now known that tire/road noise is a major contributor to exterior automobile noise [1-5] and establishes the background noise level in many environments: the other types of noise generated by an automobile, such as engine noise, muffler noise, aerodynamic noise, and so on, can be relatively easily controlled since various noise control techniques directed at them have been successfully developed. Thus, the reduction of tire/road noise source would result in a reduction of environmental stress and improvement in quality of life. To control tire/road noise, tire noise mechanisms must first be identified. Numerous mechanisms have already been identified [6-20], but it is still difficult to decide which ones are the most significant in terms of tire noise generation. Therefore, it is worthwhile to review here the various tire noise mechanisms reported in the literature.

## 1.1 Tire Noise Mechanisms

Noise can be generated by fluid flow, such as a whistle, or from a vibrating surface such as a drum: the former is referred to as an aeroacoustic noise mechanism and the latter as a structural noise mechanism [12,21]. The same categorization can be applied to the tire noise problem. Note also that tire noise can be amplified by acoustical resonances or acoustical impedance matching. Thus, acoustical amplification mechanisms will also be considered here.

### 1.1.1 Aeroacoustic Noise Mechanisms

Aerodynamic noise and air-pumping noise belong to this category. The former is the

noise associated with the turbulent airflow around tire: it can be ignored when the speed of the automobile is within a typical operation speed range [13,14]. Air-pumping noise is generated by the tread pattern acting like a "suction cup" that is applied to and then removed from a smooth surface. That is, air in the "air pockets" within the tire tread pattern or road surface is compressed or leaks away at the leading edge of the contact patch, and then is expanded or sucked into the pockets at the trailing edge. It is known that air-pumping noise is significant at the frequency range 1 kHz to 6 kHz and that it can be reduced by removing the air pockets from the tire tread pattern [15]. In the case of a "well-designed" tire, whose tread patterns are well "ventilated", and for "normal" road surfaces, which are not very smooth and do not have many air pockets, air-pumping noise may be insignificant.

### 1.1.2 Structural Noise Mechanisms

Noise generated by the tire vibration is referred to as structural noise. Tire carcass vibration is one of important tire noise source: i.e., a tire's tread block hits the road surface, and then the underlying reinforcing belts vibrate owing to the force transmitted through the tread block, resulting in sound radiation from the vibrating tire surface. Local deformation of tread blocks near the contact patch also generates structural noise; for example, when the tread block of a tire is compressed at the leading edge and then released at the trailing edges. Note also that friction phenomena near the contact patch area generate noise that is usually referred to as "squeal". It is know that squeal can be reduced by changing tire's rubber compounds and road microtexture: i.e., the friction coefficient between the tire/road interface should be as high as possible [16,17].

### 1.1.3 Acoustical Amplification Mechanisms

Groove patterns in the shape of a line or curve can be considered as pipes in the contact patch region resulting in "pipe resonance" [12]. For the purpose of designing a quiet tire, such a groove pattern should be avoided. Note also that the pipe length and the boundary condition (e.g., open or closed condition) at the ends of the pipe can be controlled to prevent undesirable noise components from being amplified by the pipe resonance.

Tire noise can also be amplified by the tire's acoustic cavity (i.e., the interior of the tire) at specific frequencies determined by the cavity geometry. This mechanism can be referred to as "cavity resonance" [18,19].

Finally, the horn shape consisting of the road surface and the treadband near the contact patch area can effectively radiate sound as a result of impedance matching: this phenomenon is referred to as the "horn effect" [20].

## 1.2 Problem Approach

Among the numerous tire noise mechanisms described above, tire carcass vibration has been extensively investigated as a primary noise source [22-35]. Once the characteristics of tire vibration are identified, the vibration response for an input force that may be used to model cavity resonance or tire/road interaction can be calculated: the cavity resonance can be considered as an acoustical pressure acting on the inner surface of a tire and the tire/road interaction as point-forces or a distributed force acting at the contact patch area. Note that tire tread pattern and road surface roughness mainly control the tire/road interaction force.

The vibration response can then be used as the input of a sound radiation analysis: horn effects can also be considered by simulating the road surface as an acoustical impedance boundary condition (normally as a rigid boundary condition).

## 1.3 Overview

Nearfield Acoustical Holography (NAH) is a useful tool for identifying sound sources since it allows sound fields represented by acoustical pressure, velocity, or intensity to be visualized in three-dimensional spaces. The NAH procedure was here applied to a rolling tire for the purpose of identifying dominant tire noise sources (see Chap. 2). A compensation procedure for source non-stationarity in multi-reference, scan-based NAH was introduced and applied to the rolling tire experiment yielding enhanced acoustical images in narrow frequency bands. An optimal virtual reference procedure was also introduced and used to separate total sound fields into several partial fields, each associated with sidewall, or leading or trailing edges near the contact patch area.

The subject of Chap. 3 is the measurement of stationary tire vibration. In the

experiment to be described here, a tire was driven radially at a point on its treadband by using a small shaker. Measurements of the resulting radial treadband vibration were then made around the treadband circumference using a laser Doppler velocimeter. Then, both non-parametric and parametric wave number decomposition techniques were applied to the experimental data. From the wave number domain representation of stationary tire vibration, the low frequency, flexural wave characteristics resulting in efficient sound radiation are observed. It is also shown that there exist fast, in-plane waves that are potentially significant sound radiators at high frequencies.

In an attempt to understand the experimental results shown in Chap. 3 in details, the tire treadband was modeled as a ring-like, circular cylindrical shell with air pressure acting on its interior surface: this work is described in Chap. 4. The model makes allowance for general boundary conditions at the lateral edges of the ring, and the sidewall of the tire is modeled as a distribution of springs and dampers. Both analytical and finite element methods were applied to obtain the vibration response. This shell model was found to explain the propagation characteristics of the waveguide modes that are visible in the experimental results. In addition to the simple circular cylindrical shell model, a full FE model having a cross-sectional shape almost identical to that of a real tire was analyzed. Although the major vibration characteristics of a tire could be reproduced by using the simple model, the full FE model can provide detailed information that is useful for sound radiation analysis.

Since a tire can be modeled as a lossy waveguide in which decaying waves propagate in the circumferential direction, it may be computationally efficient to analyze tire vibration by using hybrid, two-dimensional finite elements: i.e., the cross-section of a tire is approximated by two-dimensional finite elements, while a wave-like solution is assumed in the circumferential direction. In particular, the hybrid, 2-D element model for high frequency analysis may be very useful since a full, 3-D element model requires both a large number of finite elements and significant computational resources. In Chap. 5, a hybrid finite element formulation based on composite shell theory is described. The inflation pressure acting on the inner surface was included in the model. The full FE model described in Chap. 4 was also analyzed by using the hybrid, 2-D finite elements and the resulting dispersion relations were compared with those obtained by using a full, 3-D finite elements.

To identify the effects of tire rotation on wave propagation, the rotation of a shell about a fixed axis that simulates the axle of a car is considered in Chap. 6. The equations of motion of a rotating circular cylindrical shell were derived in a fixed

reference frame. From those equations, the analytical vibration response was obtained assuming wave solutions. It is shown that at typical rotational speeds, a stationary analysis of the circular cylindrical shell model of a tire treadband could be used to approximately predict the characteristics of the rotating tire treadband after a simple kinematic compensation is performed. Finally, conclusions are presented in Chap. 7.

# 2. NEARFIELD ACOUSTICAL HOLOGRAPHY APPLIED TO A ROLLING TIRE

In this chapter, the application of a multi-reference, scan-based Nearfield Acoustical Holography (NAH) procedure to a rolling tire for the purpose of identifying dominant tire noise sources is described. A compensation procedure for source non-stationarity was introduced and applied to the rolling tire experiment yielding enhanced acoustical images in narrow frequency bands. An optimal virtual reference procedure is also described in this chapter. That procedure was used to decompose the total sound field radiated by the composite sound source of the rolling tire into physically meaningful partial sound fields.

## 2.1 Compensation for Source Non-Stationarity

Multi-reference, scan-based Nearfield Acoustical Holography is a useful measurement tool that can be applied when an insufficient number of microphones is available to make measurements on a complete hologram surface simultaneously. The scan-based procedure can be used to construct a complete hologram by joining together sub-holograms captured using a relatively small, roving scan array and a fixed reference array. For the procedure to be successful, the source levels must remain stationary for the time taken to record the complete hologram: that is unlikely to be the case in practice, however. Usually, the reference signal levels measured during each scan differ from each other with the result that spatial noise is added to the hologram. A procedure to suppress the effects of source level, and hence reference level, variations is proposed here. The procedure is based on a formulation that explicitly features the acoustical transfer functions between the sources and both the reference and scanning, field microphones. When it is assumed that source level changes do not affect the sources' directivity, a non-stationarity compensation procedure can be derived that is based on measured transfer functions between the reference and field microphones. It has been verified both experimentally and in numerical simulations that the proposed procedure

can help suppress spatially distributed noise caused by the type of source level non-stationarity that is characteristic of realistic sources.

### 2.1.1 Introduction

Nearfield Acoustical Holography (NAH) is a useful tool for identifying noise sources and reconstructing sound fields in a three-dimensional space [36]. The holographic projection and reconstruction process is based on a phase-coherent, spatial wave field transformation that in turn requires the sound field on the hologram aperture to be fully coherent. However, in many practical cases, the sound field is created by a combination of incoherent or partially coherent sources with the result that the sound field at the hologram aperture is only partially spatially correlated.

When the sound field represents the superposition of fields radiated by incoherent or partially coherent sources, the total measured field must be decomposed into a set of spatially coherent partial fields (which are themselves mutually incoherent) before application of the holographic process to each of the partial fields in turn [40]. The projected partial fields are then added quadratically on the reconstruction surface to give the quadratic properties of the total field (e.g., sound power passing through the hologram aperture). When performing partial field decomposition, reference signals that are linearly related to source signals must be used instead of the "source" signals themselves, since in the case of most mechanical and flow noise sources, those signals cannot be directly measured. The number of fixed-location reference transducers must be equal to or greater than the number of incoherent sources to effect the partial field decomposition and to ensure that the quadratic sum of the partial fields accurately represents the quadratic properties of the total field.

Multi-reference, scan-based NAH as described above was introduced by Hald [40]: that procedure is referred to as Spatial Transformation of Sound Fields (STSF). The latter procedure is based on the use of spectral matrix relations linking the reference and field signals and makes use of principal reference signals identified using Singular Value Decomposition (SVD). The STSF procedure can be used to construct a complete hologram by joining together sub-holograms measured on each scan sector by using a relatively small scan array, provided only that the sound sources are stationary during the complete measurement: i.e., the measured reference spectra should be consistent from scan to scan. However, in practice, source levels vary during a measurement.

The effect of field level variation from scan to scan is to add spatially distributed noise to the hologram. That spatial noise can be reduced to some extent by using long averaging times, and by the application of low pass, wave number filtering to eliminate high spatial frequencies resulting from discontinuities at the edges of the sub-holograms. However the latter procedure cannot effectively eliminate spurious low wave number components that are generated when the scan array is relatively large in at least one dimension.

To develop a procedure for suppressing source non-stationarity effects, a detailed consideration of the signal and system relations between source, reference, and field data is required [39]. Based on such an investigation, a method to compensate for source non-stationarity is introduced here. The procedure is based on identifying the acoustical transfer functions that should be calculated on a scan-by-scan basis and the cross-spectral matrices that should be averaged across all the scans.

### 2.1.2 General Approach to Multi-Reference, Scan-Based NAH

The theory of NAH is based on the use of the Kirchhoff-Helmholtz integral equation to describe the sound field in a volume that encloses the sound sources [36]. The holographic projection and reconstruction procedure can be expressed in matrix form as [40]:

$$\mathbf{y}' = \mathbf{H}_{\mathrm{y'y}}\mathbf{y}\,, \tag{2.1}$$

where $\mathbf{y}$ and $\mathbf{y}'$ represent the temporally Fourier transformed acoustic fields, e.g., pressure or velocity, on the hologram and reconstruction surfaces, respectively. The matrix $\mathbf{H}_{\mathrm{y'y}}$ represents the NAH projection procedure relating the sound field on the hologram surface to that on the reconstruction surface. Equation (2.1) can be applied most directly to coherent sound fields. However, when data is measured over portions of the hologram aperture in sequence, it is necessary to use reference transducers to provide phase references. In the latter case, it is convenient to begin from a statistical description of the sound field, in which case the holographic procedure can be expressed as [40],

$$\mathbf{S}_{\mathrm{y'y'}} = \mathrm{E}\left\{\mathbf{y}'\mathbf{y}'^{\mathrm{H}}\right\} = \mathbf{H}_{\mathrm{y'y}}\mathrm{E}\left\{\mathbf{y}\mathbf{y}^{\mathrm{H}}\right\}\mathbf{H}_{\mathrm{y'y}}^{\mathrm{H}} = \mathbf{H}_{\mathrm{y'y}}\mathbf{S}_{\mathrm{yy}}\mathbf{H}_{\mathrm{y'y}}^{\mathrm{H}}\,, \tag{2.2}$$

where E denotes the expectation operator, the superscript H denotes the Hermitian transpose, and $\mathbf{S}_{\mathrm{yy}}$ and $\mathbf{S}_{\mathrm{y'y'}}$ are the cross-spectral matrices on the hologram and

reconstruction surfaces, respectively. The reconstructed fields, in the magnitude sense, are then the diagonal terms of the cross-spectral matrix on the reconstruction surface. Since the cross-spectral matrices in Eq. (2.2) comprise the auto- and cross-spectra formed amongst the complete set of field signals on the hologram or reconstruction surfaces, the measurement and calculation of the cross-spectral matrices can be very time consuming given that a measurement may involve hundreds or thousands of field points. To simplify the hologram measurement and attendant calculation of the spectral matrices, a multi-reference method was developed [40,41].

When the sound field is generated by a finite number of sources, the field signals can be expressed as a linear combination of a set of reference signals when the number of reference signals is equal to or larger than the number of sources and when the reference signals span the complete source signal space. In that case, the hologram cross-spectral matrix can be calculated indirectly when both the cross-spectral matrix of a suitable set of reference signals and the cross-spectra between the reference and field signals are known [40]. Once the complete hologram cross-spectral matrix is estimated using a multi-reference method, the hologram cross-spectral matrix must be decomposed into a set of coherent, but mutually incoherent, partial fields before the holographic projections can be performed: either SVD or partial coherence procedures may be used for that purpose [39,41]. Note that the partial fields are not unique and that their natures depend on both the decomposition procedure used and the reference microphone locations with respect to the sources. In general, the decomposed partial fields do not coincide with the physical partial fields radiated by the independent noise sources: the identified partial fields can themselves, however, be expressed as linear combinations of the physical partial fields.

As well as reducing the time taken to measure and compute the cross-spectral matrices, the multi-reference method has the advantage that it makes it possible to use a reduced set of scan microphones to measure the sound field on sectors of the hologram surface in sequence when the field can be assumed stationary. That is, the field signals are gathered step-by-step using a scanning microphone array that is smaller than the hologram aperture. During such a measurement, the location of the reference transducers must be fixed in space with respect to the various sources.

### 2.1.3 Source and Signal Relations

Here, the “source” signals are considered to be mutually uncorrelated signals that

represent distinct physical source mechanisms. Next, assume that the total sound field generated by the collection of physical sound sources is completely sensed by a set of reference transducers: i.e., it is assumed that the number of references is equal to or larger than the number of sound sources and that one or more of the reference transducers measures a signal linearly related to each of the component sources. The reference and sound field signals can then be expressed as a linear combination of the source signals multiplied by appropriate acoustical transfer functions.

As an example, the sound field radiated by two independent sources operating simultaneously can be represented by the system model illustrated in Fig. 2.1 [39]. In Fig. 2.1, $g_{ij}$ represents the transfer function between source $j$ and reference $i$, $g_{yj}$ denotes the transfer function between source $j$ and a field point, and $h_{yi}$ denotes the transfer function between reference $i$ and the field point. Note that when representing the system in terms of source signals and transfer functions, the transfer functions, $g_{ij}$ and $g_{yj}$, depend both on the geometry of the source and field point arrangement, and on the radiation characteristics of the sources: e.g., their directivity. Here it is assumed that the physical sources' radiation characteristics are not affected by source level fluctuations, and therefore remain constant through an entire holographic measurement: i.e., the transfer function $g_{ij}$ and $g_{yj}$ are assumed to be the same during each scan.

For the general case of $N$ incoherent sources and $M$ references where $M \geq N$, the reference signals can be expressed in vector-matrix form as [39],

$$\mathbf{r} = \mathbf{G}_{\mathbf{rs}}\mathbf{s}, \tag{2.3}$$

where $\mathbf{r}$ and $\mathbf{s}$ are the $M$ by 1 reference signal vector and the $N$ by 1 source signal vector, respectively, and $\mathbf{G}_{\mathbf{rs}}$ is the $M$ by $N$ transfer function matrix that relates the source and reference signals. The field signals on the hologram surface can also be represented as the product of a transfer function matrix and the source signal vector: i.e.,

$$\mathbf{y} = \mathbf{G}_{\mathbf{ys}}\mathbf{s}, \tag{2.4}$$

where $\mathbf{y}$ is the field signal vector on the hologram surface and $\mathbf{G}_{\mathbf{ys}}$ is the transfer function matrix relating the source and field signals. From Eqs. (2.3) and (2.4), the cross-spectral matrix relating the reference and field signals can be expressed as

$$\mathbf{S}_{\mathbf{ry}} = \mathrm{E}\left\{\mathbf{r}\mathbf{y}^{\mathrm{H}}\right\} = \mathbf{G}_{\mathbf{rs}}\mathbf{S}_{\mathbf{ss}}\mathbf{G}_{\mathbf{ys}}^{\mathrm{H}}, \tag{2.5}$$

where $\mathbf{S}_{\mathbf{ry}}$ is the cross-spectral matrix between the reference and field signals and $\mathbf{S}_{\mathbf{ss}}$ is the source signal cross-spectral matrix which, under the conditions prescribed above, is diagonal (the diagonal components being the auto-spectra of the source signals). By

using Eq. (2.3), the reference spectral matrix can be also written as

$$\mathbf{S}_{\mathbf{rr}} = \mathrm{E}\left\{\mathbf{r}\mathbf{r}^{\mathrm{H}}\right\} = \mathbf{G}_{\mathbf{rs}}\mathbf{S}_{\mathbf{ss}}\mathbf{G}_{\mathbf{rs}}^{\mathrm{H}}, \tag{2.6}$$

where $\mathbf{S}_{\mathbf{rr}}$ is the reference cross-spectral matrix. Note that any source level variation appearing in the source auto-spectra on the right-hand side of Eq. (2.6) translates directly into variation of the reference cross-spectral matrix through the transfer function matrix, $\mathbf{G}_{\mathbf{rs}}$.

### 2.1.4 Description of Multi-Reference NAH

The field signals on the hologram surface can be expressed as a linear combination of the reference signals multiplied by appropriate transfer functions: i.e.,

$$\mathbf{y} = \mathbf{H}_{\mathbf{yr}}\mathbf{r}, \tag{2.7}$$

where $\mathbf{r}$ is the reference signal vector, and $\mathbf{H}_{\mathbf{yr}}$ is the transfer matrix that relates the reference and field signals on the hologram surface. By multiplying each side of Eq. (2.7) by $\mathbf{r}^{\mathrm{H}}$ and then finding the expectation of the result, an equation for the latter transfer function matrix can be obtained: i.e.,

$$\mathbf{H}_{\mathbf{yr}} = \mathbf{S}_{\mathbf{ry}}^{\mathrm{H}}\mathbf{S}_{\mathbf{rr}}^{-1}, \tag{2.8}$$

where the inverse of the reference cross-spectral matrix represents a generalized inverse to accommodate situations in which the reference cross-spectral matrix is rank-deficient. Similarly, the cross-spectral matrix on the hologram surface can be expressed as

$$\mathbf{S}_{\mathbf{yy}} = \mathbf{H}_{\mathbf{yr}}\mathbf{S}_{\mathbf{ry}}. \tag{2.9}$$

By substituting Eq. (2.8) into Eq. (2.9), the hologram cross-spectral matrix can be estimated by using the reference cross-spectral matrix in combination with the cross-spectral matrix relating the reference and field signals on the hologram surface: i.e.,

$$\mathbf{S}_{\mathbf{yy}} = \mathbf{S}_{\mathbf{ry}}^{\mathrm{H}}\mathbf{S}_{\mathbf{rr}}^{-1}\mathbf{S}_{\mathbf{ry}}. \tag{2.10}$$

Note that the cross-spectral matrix can be decomposed into an infinite variety of incoherent partial fields subject only to the condition that $\mathbf{S}_{\mathbf{yy}} = \mathbf{Y}\mathbf{Y}^{\mathrm{H}}$, where $\mathbf{Y}$ represents a partial field matrix. From Eqs. (2.8) and (2.10), the partial field matrix, $\mathbf{Y}$, can then be represented as [39]

$$\mathbf{Y} = \mathbf{S}_{\mathbf{ry}}^{\mathrm{H}} \mathbf{S}_{\mathbf{rr}}^{-1/2} = \mathbf{H}_{\mathbf{yr}} \mathbf{S}_{\mathbf{rr}}^{1/2} . \tag{2.11}$$

The SVD and partial coherence methods have been used for calculation of the partial field decomposition given in Eq. (2.11). Note that each column of the matrix, **Y**, represents a partial field vector. In the SVD method, the reference cross-spectral matrix is decomposed by using SVD and thus the partial fields can be represented as

$$\mathbf{Y} = \mathbf{S}_{\mathbf{ry}}^{\mathrm{H}} \mathbf{U} \mathbf{S}^{-1/2} = \mathbf{H}_{\mathbf{yr}} \mathbf{U} \mathbf{S}^{1/2} , \tag{2.12}$$

where **U** is the unitary matrix and **S** is the diagonal matrix of singular values. The partial coherence method is based on the use of LU decomposition [60] to separate the reference cross-spectral matrix into two parts, and in that case the partial fields are written as

$$\mathbf{Y} = \mathbf{S}_{\mathbf{ry}}^{\mathrm{H}} \mathbf{L}^{-1} \mathbf{D}^{-1/2} = \mathbf{H}_{\mathbf{yr}} \mathbf{L} \mathbf{D}^{1/2} , \tag{2.13}$$

where **L** is lower triangular matrix and **D** is the diagonal matrix with pivots. The SVD procedure has been used in the experiments presented in this chapter.

### 2.1.5 Non-Stationarity Compensation

By substituting Eqs. (2.5) and (2.6) into Eq. (2.8), the transfer function matrix relating the reference and field signals can be expressed in terms of the source matrix and the associated transfer matrix: i.e.,

$$\mathbf{H}_{\mathbf{yr}} = \mathbf{S}_{\mathbf{ry}}^{\mathrm{H}} \mathbf{S}_{\mathbf{rr}}^{-1} = \mathbf{G}_{\mathbf{ys}} \mathbf{S}_{\mathbf{ss}} \mathbf{G}_{\mathbf{rs}}^{\mathrm{H}} \left( \mathbf{G}_{\mathbf{rs}} \mathbf{S}_{\mathbf{ss}} \mathbf{G}_{\mathbf{rs}}^{\mathrm{H}} \right)^{-1} = \mathbf{G}_{\mathbf{ys}} \mathbf{G}_{\mathbf{rs}}^{-1} . \tag{2.14}$$

Note that the source cross-spectral matrix cancels out in this calculation and thus the transfer matrix between the reference and field signals is independent of source level variation since the transfer matrices between the source and reference and field signals are themselves assumed to be independent of source level. Under these conditions, the reference cross-spectral matrix varies in direct proportion to the source level non-stationarity, as shown in Eq. (2.6), from one scan sector to the next, but the transfer function matrix appropriate for each scan is consistent even when the source levels vary.

Based on the above considerations, the partial field matrix, Eq. (2.11), can finally be written in modified form as

$$\mathbf{Y} = \mathbf{H}_{\mathbf{yr},(\text{step})}\mathbf{S}^{1/2}_{\mathbf{rr},(\text{avg})} = \mathbf{S}^{\text{H}}_{\mathbf{ry},(\text{step})}\mathbf{S}^{-1}_{\mathbf{rr},(\text{step})}\mathbf{S}^{1/2}_{\mathbf{rr},(\text{avg})}, \tag{2.15}$$

where the subscripts (step) and (avg) denote spectral matrix estimates calculated during each scan and averaged over all the scans, respectively. The partial field decomposition represented by Eq. (2.15) thus combines transfer functions estimated during each scan with reference information averaged over the complete measurement set to create a consistent set of partial fields. Given the above assumptions, non-stationary effects should be suppressed in partial fields calculated using Eq. (2.15).

## 2.2 Partial Field Decomposition by Using Optimally-Located Virtual References

It has been shown previously that the multiple reference and field signals recorded during a scanning acoustical holography measurement can be used to decompose the total measured sound field radiated by a composite sound source into mutually incoherent partial fields. To obtain physically meaningful partial fields, i.e., fields closely related to particular component sources, the reference microphones should be positioned as close as possible to the component physical sources that together comprise the complete source. However, it is not always possible either to identify the optimal reference microphone locations prior to performing a holographic measurement, or to place reference microphones at those optimal locations, even if known, owing to physical constraints. Here, post-processing procedures are described that make it possible both to identify the optimal reference microphone locations and to place virtual references at those locations *after* performing a holographic measurement. The optimal reference microphone locations are defined to be those at which the Multiple Signal Classification (MUSIC) power is maximized in a three-dimensional space reconstructed by holographic projection. The acoustic pressure signals at the locations thus identified can then be used as optimal "virtual" reference signals. It is shown through an experiment and numerical simulation that the optimal virtual reference signals can be successfully used to identify physically meaningful partial sound fields particularly when used in conjunction with partial coherence decomposition procedures.

### 2.2.1 Introduction

For the NAH procedure to be successful in its simplest form, the measured sound field must be spatially phase-coherent. Such a spatially phase-coherent sound field can be obtained by capturing the sound pressure on the entire measurement surface simultaneously. However, the latter measurement requires the use of many field microphones, perhaps hundreds or thousands, which may not always be practical. When the sound field generated by a single coherent source is stationary, however, a relatively small number of scan microphones can be used in combination with a fixed-location reference microphone to sample data on portions of the hologram surface sequentially. The reference spectral data can then be combined with the transfer functions linking the references and the field points on the hologram surface to create a complex pressure distribution on the latter surface which may then be projected as desired.

A multi-reference procedure referred to as Spatial Transformation of Sound Fields (STSF), was introduced by Hald to accommodate situations in which the sound field is generated by a composite source comprising more than one mutually-incoherent source [40]. The latter procedure, described in terms of a reference cross-spectral matrix and a cross-spectral matrix linking the reference and field signals, is based on using singular value decomposition (SVD) to separate the total sound field into a set of phase-coherent partial fields that are incoherent with each other. The partial fields can then be independently projected and added together to yield the quadratic properties of the sound field on the reconstruction surfaces of interest. Note that in this procedure the characteristics of the partial fields depend on the reference microphone locations with respect to the component sources, and thus the partial field decomposition is not unique. As a result, the partial fields determined in this way cannot usually be associated with particular component sources.

Since the introduction of STSF, a number of investigations have focused on separating the total sound field into individual partial sound fields that *can* be associated with meaningful physical sources: e.g., in case of a running automobile, flow noise, engine noise, tire noise, etc. As an alternative to the SVD procedure, Hallman and Bolton [41] suggested the application of partial coherence decomposition (PCD), based on Gauss elimination [60], to separate the partial fields. Kwon and Bolton [39] compared the performance of the SVD and PCD methods; they also introduced the use of the multiple signal classification (MUSIC) algorithm [61] for the selection of the best references from amongst many candidates positioned around a composite sound source.

It was shown that the reference microphones should be positioned close to the individual physical sources if physically meaningful partial sound fields were to be obtained. However, in practice, the location of the most prominent sources is sometimes not known prior to performing a holographic measurement. There are also cases in which it is impossible to place references at the desired locations even when those locations are known: for example, when a reference microphone placed close to a physical source might itself induce flow noise or when the desired locations are otherwise inaccessible for practical reasons.

Thus, to facilitate the decomposition of a sound field into physically meaningful components, it would be desirable to be able to place "virtual" references at optimal locations *after* performing a holographic measurement made using a set of sufficient, but non-optimally located references.

A virtual reference procedure was first described by Nam and Kim [56]: it was based on a vector representation [57] of the sound field combined with a knowledge of various point-to-point transfer functions both measured and estimated by using holographic projections. First note that in their procedure it is assumed that the number of "real" and "virtual" references used first to measure, and then to post-process the data, is the same. However, when a holographic measurement is performed, it may be desirable to use a larger number of real references than virtual references to ensure that the total sound field is captured completely and to reduce noise effects. Nam and Kim also concluded that virtual references should be located at positions on the source surface where the amplitude of an acoustical property of interest, such as the pressure, particle velocity, or active intensity, was a maximum. Through numerical simulations it was shown that by positioning the virtual references appropriately on the source surface the sound field could be decomposed into physically meaningful partial fields, particularly when PCD was performed.

Here, the partial field decomposition procedure based on the use of virtual references introduced by Nam and Kim is re-derived in an alternative form, based on the use of signal cross-spectral matrices and transfer functions, with the intent of developing a procedure that is compatible with conventional multi-reference NAH techniques [40]. The procedure to be described here also makes it possible to use a larger number of real than virtual references as would usually be the case in practice. Here, an optimization procedure combined with the MUSIC algorithm was used to help identify the optimal reference locations. The optimal reference locations were identified by searching for the positions in three-dimensional space at which the MUSIC power was locally

maximized. By using the proposed procedure, it was possible to identify optimal reference positions in terms of both the projection surface location and the location on the projection surface; in contrast, by simply maximizing the amplitude of a particular acoustical property, e.g., pressure, only the virtual reference location on a projected surface can be identified. It is shown here, through both experiment and numerical simulation, that the optimal virtual reference procedure can yield improved estimates of the physical partial sound fields.

### 2.2.2 Projection in Multi-Reference NAH

When the total sound field generated by a composite source comprising a finite number of uncorrelated physical sources is completely sensed by a set of reference transducers (i.e., the number of references is equal to or larger than the number of uncorrelated sources and each uncorrelated source is sensed by at least one reference transducer), the field signals on the hologram surface can be expressed in the frequency domain as a linear combination of reference signals multiplied by appropriate acoustical transfer functions as shown in Eq. (2.7): i.e.,

$$\begin{bmatrix} y_1 \\ y_2 \\ \vdots \\ y_N \end{bmatrix} = \begin{bmatrix} h_{11} & h_{12} & \cdots & h_{1M} \\ h_{21} & h_{22} & \cdots & h_{2M} \\ \vdots & \vdots & \ddots & \vdots \\ h_{N1} & h_{N2} & \cdots & h_{NM} \end{bmatrix} \begin{bmatrix} r_1 \\ r_2 \\ \vdots \\ r_M \end{bmatrix}, \tag{2.16a}$$

where $y_i$ represents the $i$-th field signal on the hologram surface ($i$ = 1, 2, ···, $N$, and $N$ is the total number of measurement points on the hologram aperture), $r_j$ denotes the $j$-th reference signal ($j$ = 1, 2, ···, $M$, $M \geq 1$, and $M$ is the total number of reference microphones), and $h_{ij}$ denotes the transfer function between the $j$-th reference and $i$-th field signal. Equation (2.16a) can be expressed in compact vector-matrix form as,

$$\mathbf{y} = \mathbf{H}_{\mathbf{yr}}\mathbf{r}\,, \tag{2.16b}$$

where $\mathbf{y}$ and $\mathbf{r}$ are the $N$ by 1 field signal vector and the $M$ by 1 reference signal vector, respectively, and $\mathbf{H}_{\mathbf{yr}}$ is the $N$ by $M$ transfer function matrix that relates the reference and field signals. When the holographic measurement is made using a scanning procedure in which data over portions of the hologram aperture are captured sequentially, it is convenient to describe the sound field statistically. In the latter case, Eq. (2.16b) can be

modified by multiplying it by the Hermitian transpose of the reference vector and then evaluating the ensemble average to give:

$$\mathbf{S}_{\mathbf{yr}} = \mathbf{S}_{\mathbf{ry}}^{\mathrm{H}} = \mathrm{E}\left\{\mathbf{y}\mathbf{r}^{\mathrm{H}}\right\} = \mathbf{H}_{\mathbf{yr}}\mathrm{E}\left\{\mathbf{r}\mathbf{r}^{\mathrm{H}}\right\} = \mathbf{H}_{\mathbf{yr}}\mathbf{S}_{\mathbf{rr}}, \tag{2.17}$$

where E denotes the expectation operator, the superscript H denotes the Hermitian transpose, $\mathbf{S}_{\mathbf{ry}}$ is the cross-spectral matrix between the reference and field signals, and $\mathbf{S}_{\mathbf{rr}}$ is the reference cross-spectral matrix. Here it is assumed that the number of incoherent sources is $K \leq M$: the number of incoherent sources in any particular case can, in principle, be determined by counting the number of significant singular values when the reference cross-spectral matrix is decomposed by using SVD [55]. In the latter case, it is desirable to decompose the reference cross-spectral matrix by using SVD. The reference cross-spectral matrix, $\mathbf{S}_{\mathbf{rr}}$, can then be represented as the product of a diagonal matrix whose elements are the singular values, and a unitary matrix whose column vectors are the eigenvectors of $\mathbf{S}_{\mathbf{rr}}(\mathbf{S}_{\mathbf{rr}})^{\mathrm{H}}$. When the singular values associated with the noise subspace are small enough to be ignored, the reference cross-spectral matrix can be approximated as comprising only the first $K$ singular values and eigenvectors: i.e.,

$$\mathbf{S}_{\mathbf{rr}} = \mathbf{V}\boldsymbol{\Lambda}\mathbf{V}^{\mathrm{H}}, \tag{2.18}$$

where $\mathbf{V}$ is an $M$ by $K$ matrix whose $m$-th column is the column vector of the unitary matrix and $\boldsymbol{\Lambda}$ is the $K$ by $K$ diagonal matrix whose $m$-th diagonal element is the $m$-th singular value. By substituting Eq. (2.18) into Eq. (2.17), the transfer matrix relating the reference and field signals can be expressed as

$$\mathbf{H}_{\mathbf{yr}} = \mathbf{S}_{\mathbf{ry}}^{\mathrm{H}}\mathbf{S}_{\mathbf{rr}}^{-1} = \mathbf{S}_{\mathbf{ry}}^{\mathrm{H}}\mathbf{V}\boldsymbol{\Lambda}^{-1}\mathbf{V}^{\mathrm{H}}. \tag{2.19}$$

From Eq. (2.16b), the cross-spectral matrix of the field signals on the hologram surface can be estimated by using the reference cross-spectral matrix in Eq. (2.18): i.e.,

$$\mathbf{S}_{\mathbf{yy}} = \mathbf{H}_{\mathbf{yr}}\mathbf{S}_{\mathbf{rr}}\mathbf{H}_{\mathbf{yr}}^{\mathrm{H}} = \mathbf{H}_{\mathbf{yr}}\mathbf{V}\boldsymbol{\Lambda}\mathbf{V}^{\mathrm{H}}\mathbf{H}_{\mathbf{yr}}^{\mathrm{H}}. \tag{2.20}$$

The cross-spectral matrix of field signals on the hologram surface can then be decomposed to represent a set of incoherent partial fields subject only to the condition that $\mathbf{S}_{\mathbf{yy}} = \mathbf{Y}\mathbf{Y}^{\mathrm{H}}$, where each column of the matrix, $\mathbf{Y}$, represents a partial field vector: e.g.,

$$\mathbf{Y} = \mathbf{H}_{\mathbf{yr}}\mathbf{V}\boldsymbol{\Lambda}^{1/2} = \mathbf{H}_{\mathbf{yl}}\boldsymbol{\Lambda}^{1/2}, \tag{2.21}$$

where $\boldsymbol{\Lambda}^{1/2}$ is the principal reference signal matrix and $\mathbf{H}_{\mathbf{yl}}$ is the transfer matrix between the principal reference signal matrix and the partial field matrix ($\mathbf{H}_{\mathbf{yl}} = \mathbf{H}_{\mathbf{yr}}\mathbf{V}$). The acoustical field on any reconstruction surface can then be expressed as,

$$\mathbf{Y}' = \mathbf{H}_{\mathbf{y'y}}\mathbf{Y} = \mathbf{H}_{\mathbf{y'y}}\mathbf{H}_{\mathbf{yr}}\mathbf{V}\boldsymbol{\Lambda}^{1/2} = \mathbf{H}_{\mathbf{y'y}}\mathbf{H}_{\mathbf{yl}}\boldsymbol{\Lambda}^{1/2} = \mathbf{H}_{\mathbf{y'l}}\boldsymbol{\Lambda}^{1/2}, \tag{2.22}$$

where $\mathbf{Y}'$ is the partial field matrix on the reconstruction surface and $\mathbf{H}_{\mathbf{y'l}}$ represents the transfer matrix between the principal reference signals and the partial field signals on the reconstruction surface. The matrix $\mathbf{H}_{\mathbf{y'y}}$ is composed of the transfer functions that relate the field signals on the hologram and reconstruction surfaces, and it represents the NAH projection procedure including the spatial Fourier transform (in the planar case) and the propagation operation: the latter procedure also incorporates the effects of discretization, windowing, spatial filtering, zero-padding, etc. [36,40]. Note that in practice, the matrix $\mathbf{H}_{\mathbf{yr}}$ appearing in Eq. (2.22) should be calculated from the cross-spectral matrices, $\mathbf{S}_{\mathbf{yr},(\mathrm{step})}$ and $\mathbf{S}_{\mathbf{rr},(\mathrm{step})}$, measured during each individual scan, by using Eqs. (2.18) and (2.19), while $\mathbf{V}$ and $\boldsymbol{\Lambda}$ are calculated from the reference cross-spectral matrix, $\mathbf{S}_{\mathbf{rr},(\mathrm{avg})}$, averaged over all the scans, in order to suppress spatial noise caused by source non-stationarity (as noted earlier in this chapter). Finally note that each column of $\mathbf{H}_{\mathbf{y'l}}$ corresponds to the NAH projection of the corresponding column of $\mathbf{H}_{\mathbf{yl}}$. The cross-spectral matrix of the field signals on a reconstruction surface can then be calculated from Eq. (2.22) as

$$\mathbf{S}_{\mathbf{y'y'}} = \mathbf{Y}'\mathbf{Y}'^{\mathrm{H}} = \mathbf{H}_{\mathbf{y'l}}\boldsymbol{\Lambda}\mathbf{H}_{\mathbf{y'l}}^{\mathrm{H}}. \tag{2.23}$$

### 2.2.3 Virtual Reference Procedure

Virtual references can, in principle, be placed anywhere within the three-dimensional space covered by the NAH projection. By making use of the partial field signal matrices evaluated on the reconstruction surfaces, as in Eq. (2.22), the virtual reference signal matrix can be expressed as

$$\mathbf{X} = \begin{bmatrix} \mathbf{c}_1^{\mathrm{T}}\mathbf{Y}_1' \\ \mathbf{c}_2^{\mathrm{T}}\mathbf{Y}_2' \\ \vdots \\ \mathbf{c}_K^{\mathrm{T}}\mathbf{Y}_K' \end{bmatrix} = \begin{bmatrix} \mathbf{c}_1^{\mathrm{T}}\mathbf{H}_{\mathbf{y}_1'\mathbf{l}} \\ \mathbf{c}_2^{\mathrm{T}}\mathbf{H}_{\mathbf{y}_2'\mathbf{l}} \\ \vdots \\ \mathbf{c}_K^{\mathrm{T}}\mathbf{H}_{\mathbf{y}_K'\mathbf{l}} \end{bmatrix} \boldsymbol{\Lambda}^{1/2} = \mathbf{H}_{\mathbf{xl}}\boldsymbol{\Lambda}^{1/2}, \tag{2.24}$$

where $\mathbf{X}$ is the $K$ by $K$ virtual reference signal matrix. In Eq. (2.24), $\mathbf{c}_m$ represents the $N$ by 1 reference selection vector: when the $m$-th virtual reference is positioned at the $i$-th field position on the reconstruction surface, all elements of $\mathbf{c}_m$ are zeros except for the element at the $i$-th row, which is itself unity. Note that the matrix $\mathbf{Y}'_m$ in Eq. (2.24)

represents the partial field signal matrix for the reconstruction surface on which the $m$-th virtual reference is placed, and that the vector, $\mathbf{c}_m$, denotes the $m$-th virtual reference location on the $m$-th reconstruction surface. Thus, the location of the $m$-th reconstruction surface in combination with the vector, $\mathbf{c}_m$, determines the location of the $m$-th virtual reference in a three-dimensional space. The cross-spectral matrices between the virtual reference signals, and between the virtual reference and the field signals on the hologram surface, can then be obtained from Eqs. (2.21) and (2.24): i.e.,

$$\mathbf{S}_{\mathbf{xx}} = \mathbf{X}\mathbf{X}^{\mathrm{H}} = \mathbf{H}_{\mathbf{xl}}\boldsymbol{\Lambda}\mathbf{H}_{\mathbf{xl}}^{\mathrm{H}}, \tag{2.25}$$

and

$$\mathbf{S}_{\mathbf{xy}} = \mathbf{X}\mathbf{Y}^{\mathrm{H}} = \mathbf{H}_{\mathbf{xl}}\boldsymbol{\Lambda}\mathbf{H}_{\mathbf{yl}}^{\mathrm{H}}, \tag{2.26}$$

where $\mathbf{S}_{\mathbf{xx}}$ is the virtual reference cross-spectral matrix and $\mathbf{S}_{\mathbf{xy}}$ is the cross-spectral matrix between the virtual reference and field signals on the hologram surface.

Recall that under ideal circumstances, the physical reference microphones should be placed at the locations of physical, uncorrelated sources. In practice it may not be possible to position real reference microphones at those points.

It has been shown previously that the MUSIC algorithm can be combined with the SVD procedure to guide the selection of the best "real" reference microphones from amongst a large number of real microphones positioned around a noise source [39]. Since the MUSIC algorithm can be used to find the locations of sources in a three-dimensional space [61], the latter procedure has here been modified to identify the optimal virtual reference locations: the optimal locations are here identified as the points in a three-dimensional space at which the MUSIC power, defined below, is maximized.

When the cross-spectral matrix of the field signals on a reconstruction surface, i.e., $\mathbf{S}_{\mathbf{y'y'}}$ in Eq. (2.23), is decomposed by using the SVD procedure ($\mathbf{S}_{\mathbf{y'y'}} = \mathbf{W}\boldsymbol{\Sigma}\mathbf{W}^{\mathrm{H}}$), the unitary matrix, $\mathbf{W}$, can be expressed in terms of the eigenvectors of $\mathbf{S}_{\mathbf{y'y'}}(\mathbf{S}_{\mathbf{y'y'}})^{\mathrm{H}}$: i.e., $\mathbf{W} = [\mathbf{w}_1\ \mathbf{w}_2\ \cdots\ \mathbf{w}_N]$, where $\mathbf{w}_n$ is the $n$-th eigenvector associated with the $n$-th singular value. Since the number of incoherent sources is $K$, the noise subspace, $\mathbf{R}_{\mathrm{noise}}$, can be defined in terms of the noise-related eigenvectors, $\mathbf{w}_n$ ($n = K+1$ to $N$), as

$$\mathbf{R}_{\mathrm{noise}} = \sum_{n=K+1}^{N} \mathbf{w}_n \mathbf{w}_n^{\mathrm{H}}. \tag{2.27}$$

The MUSIC power is then defined in terms of $\mathbf{R}_{\mathrm{noise}}$ as

$$P_{\mathrm{MUSIC}} = \frac{1}{\mathbf{u}^{\mathrm{H}}\mathbf{R}_{\mathrm{noise}}\mathbf{u}}, \tag{2.28}$$

where $\mathbf{u}$ is the trial vector. Since the signal subspace spanned by $\mathbf{w}_n$ ($n = 1$ to $K$) is

orthogonal to the noise subspace represented by $\mathbf{R}_{\text{noise}}$, the MUSIC power should be infinite when $\mathbf{u} = \mathbf{w}_n$ ($n$ = 1 to $K$).

Assume, for example, that a vector representing a source at the $n$-th discrete point of the reconstruction surface can be approximated as the trial vector,

$$\mathbf{u}_n = [0 \quad \cdots \quad 0 \quad 1 \quad 0 \quad \cdots \quad 0]^{\mathrm{T}}, \tag{2.29}$$

where the $n$-th element of $\mathbf{u}_n$ is one and the other $N$-1 elements are zeros. In that case, the MUSIC power associated with the trial vector, $\mathbf{u}_n$, would be very large.

After calculating the MUSIC powers associated with all possible trial vectors, $\mathbf{u} = \mathbf{u}_n$ ($n$ = 1 to $N$), a map of the MUSIC power on a two-dimensional reconstruction surface can be obtained by reshaping the MUSIC power vector into a matrix whose elements represent the MUSIC power at a point on a two-dimensional surface. A three-dimensional MUSIC power image can then be obtained by repeating the latter operations on other projection surfaces in sequence. Since the MUSIC power at source locations is large, the optimal virtual reference locations are those where the MUSIC power is maximized locally. The virtual reference signals at those optimal locations can then be obtained from Eq. (2.24) since the reference locations that are identified by performing the optimal search are expressed in terms of the reconstruction surface locations and the reference selection vectors that appear in the latter equation.

The trial vector defined in Eq. (2.29) closely represents the sound field generated by a monopole source. It is thus likely that the maximum MUSIC power procedure as described here will identify the locations of monopole-like sources. Other trial vectors may be more appropriate for identifying the locations of more complicated sources, e.g., panel modes, but here attention is limited to trial vectors of the type defined in Eq. (2.29).

Consider next two monopole sources that are spatially separated but which are coherent: the MUSIC power criterion as defined above would identify sources at both locations. However, in this case there is only one coherent source mechanism: i.e., the number of incoherent sources is smaller than number of local MUSIC power maxima. In the latter case, virtual references should first be placed at all local MUSIC power maxima. Based on the virtual reference cross-spectral matrix, Eq. (2.25), the coherence between virtual references $i$ and $j$ can be calculated: i.e.,

$$\gamma_{ij}^2 = \frac{|S_{ij}|^2}{S_{ii} \cdot S_{jj}}, \tag{2.30}$$

where $S_{ii}$ and $S_{jj}$ are the auto-spectra of the virtual references $i$ and $j$, respectively, and $S_{ij}$

is the cross-spectrum between the virtual references $i$ and $j$. If the coherence between the signals at two candidate source locations is nearly unity, the sources at those two locations are coherent. The virtual reference at the location at which the MUSIC power is smaller should then be removed.

### 2.2.4 Partial Sound Field Decomposition

Once the optimal virtual reference locations are identified, the virtual reference signals at those positions can be obtained from Eq. (2.24). In addition, the cross-spectral matrices between the virtual reference signals, and between the virtual reference and field signals on the hologram surface, can then be calculated from Eqs. (2.25) and (2.26). The cross-spectral matrix of the field signals on the hologram surface can be expressed in terms of the latter cross-spectral matrices: i.e.,

$$\mathbf{S}_{\mathbf{yy}} = \mathbf{S}_{\mathbf{xy}}^{\mathrm{H}} \mathbf{S}_{\mathbf{xx}}^{-1} \mathbf{S}_{\mathbf{xy}} . \tag{2.31}$$

The cross-spectral matrix of field signals in Eq. (2.31) can be decomposed into a partial field matrix, $\mathbf{Y}_{\mathbf{x}}$, based on the "virtual" reference signals subject only to the condition that $\mathbf{S}_{\mathbf{yy}} = \mathbf{Y}_{\mathbf{x}}(\mathbf{Y}_{\mathbf{x}})^{\mathrm{H}}$: i.e.,

$$\mathbf{Y}_{\mathbf{x}} = \mathbf{S}_{\mathbf{xy}}^{\mathrm{H}} \mathbf{S}_{\mathbf{xx}}^{-1/2} , \tag{2.32}$$

where each column of $\mathbf{Y}_{\mathbf{x}}$ represents a partial field vector: the first column represents the first partial field vector, the second column represents the second partial field vector, and so on. Since the decomposition in Eq. (2.32) is not unique (since the square root inverse of the reference cross-spectral matrix is not uniquely determined), it is desirable to estimate "good" partial fields.

The SVD and PCD procedures have been widely used to perform the partial field decomposition expressed in Eq. (2.32) [39]. In the SVD method, the virtual reference cross-spectral matrix is represented as $\mathbf{S}_{\mathbf{xx}} = \mathbf{U}\mathbf{S}\mathbf{U}^{\mathrm{H}}$, where $\mathbf{U}$ is the unitary matrix and $\mathbf{S}$ is the diagonal matrix of singular values. The partial fields can thus be represented as

$$\mathbf{Y}_{\mathbf{x},\mathrm{SVD}} = \mathbf{S}_{\mathbf{xy}}^{\mathrm{H}} \mathbf{U}\mathbf{S}^{-1/2} . \tag{2.33}$$

The PCD procedure is based on the use of LU decomposition, obtained from the Gauss elimination process [60], to separate the reference cross-spectral matrix into two matrices: i.e., $\mathbf{S}_{\mathbf{xx}} = \mathbf{L}\mathbf{D}\mathbf{L}^{\mathrm{H}}$, where $\mathbf{L}$ is the lower triangular matrix whose diagonal

elements are unity and **D** is the diagonal matrix. In the latter case the partial fields are written as

$$\mathbf{Y}_{\mathbf{x},\mathrm{PCD}} = \mathbf{S}_{\mathbf{xy}}^{\mathrm{H}}\mathbf{L}^{\mathrm{H}^{-1}}\mathbf{D}^{-1/2}. \tag{2.34}$$

When the partial decomposition is based instead on the use of real reference signals, the cross-spectral matrices in Eqs. (2.33) and (2.34) should be calculated using the real rather than the virtual reference signals: i.e., $\mathbf{S_{rr}}$ and $\mathbf{S_{ry}}$ instead of $\mathbf{S_{xx}}$ and $\mathbf{S_{xy}}$. Note that when performing a partial coherence decomposition, the number of real references should be equal to the number of incoherent sources. When the virtual reference procedure is used, surplus references can be discarded before performing the partial field decomposition.

## 2.3 Holography Measurements on a Rolling Tire

An experiment using two loudspeakers driven separately by independent random noise sources and a corresponding numerical simulation which used two monopoles simulating the loudspeakers were described in Refs. [38,62]. It was shown through both the experiment and numerical simulation that the compensation procedure described in Eq. (2.15) reduces the spatial noise resulting from source non-stationarity even when the standard deviation of the source levels was approximately 1 dB: i.e., even when the sources were "reasonably" stationary [38].

The latter experiment and simulation data were also analyzed by using the proposed virtual reference procedure. It was shown that the optimal virtual reference procedure results in partial fields that are very similar to the "real" partial fields associated with individual physical sources regardless of the locations of the real references; however, the partial fields decomposed by using the real reference signals directly were found to be physically meaningful only when the references were located very close to the actual sources [62]. It was also found that using the set of virtual references located at the maximum MUSIC power locations resulted in more accurate estimates of the physically meaningful partial fields than were obtained using any other set of virtual references (e.g., on the source plane) or even a set of "good" real references [62].

Here, the compensation procedure described above was applied to the holographic measurement of a rolling tire. The latter experimental data were also analyzed by using the optimal virtual reference procedure to separate sound radiation from the leading and

trailing edges and the sidewall of the rolling tire.

Figure 2.2 shows a photograph of the experimental setup for the rolling tire. A corresponding illustration of the setup is shown in Fig. 2.3. A tire mounted on a car was driven by a roller: the tire was rotating in the counterclockwise direction corresponding to an automobile speed of 21 mph. An 8 by 8 square microphone array with a spacing of 10 cm was used to scan the hologram aperture shown in Fig. 2.3. The location of the hologram surface was $z$ = 5 cm when the origin of the $z$-axis was on the sidewall of tire (i.e., the source plane is located at $z$ = 0). Once a scan was completed, the microphone array was shifted laterally or vertically by 5 cm to complete the measurement with a sampling space of 5 cm. Since the hologram aperture comprised 32 by 16 points to be measured and the size of the scanning microphone array was 8 by 8, 8 scans (4 scans in the $x$-direction and 2 scans in the $y$-direction) and the associated measurements were performed. During the scanning, 8 reference microphones were fixed around the tire as shown in Figs. 2.2 and 2.3. Windshields were applied to reference microphones 2 and 3 to suppress flow noise. During each scan, the data record length was 2048 points at a sampling rate of 4096 Hz and 50 linear averages were performed when estimating the various spectra; during the latter operations a 1024 point overlap was used and a Hanning window was applied to each record. Here, the measured data were processed up to 1.6 kHz. Note that the sampling space of 5 cm is small enough to capture an acoustic image in the frequency range of interest since the wavelength at 1.6 kHz is approximately 20 cm (to avoid spatial aliasing, the sampling space must be smaller than half of the minimum wavelength). Note also that the size of the hologram aperture is large enough that the acoustic pressure at its edges can be assumed to be zero.

## 2.4 Results and Discussion

The singular values of the measured reference cross-spectral matrix averaged over all scans are shown in Fig. 2.4. It can be seen that the first singular value is significantly larger than the second singular value at most frequencies. Since the number of incoherent sources can, in principle, be determined by counting the number of significant singular values [55], it can be concluded that only one incoherent source is dominant. However, at some frequencies, e.g., 216 Hz, the first two singular values are significantly larger than the others values and they are very close to each other (the difference is approximately 2 dB at 216 Hz): i.e., at those frequencies, two incoherent sources are

significant. Here, the measured data at 216 Hz was chosen to demonstrate the non-stationary compensation effects and the decomposed partial fields obtained by using the optimal virtual reference procedure: the results are shown in Figs. 2.5 to 2.10.

The sound pressure fields, decomposed by using real references combined with the SVD procedure on the hologram surface at 216 Hz are shown in Figs. 2.5 and 2.6: the results in Fig. 2.5 were obtained without source non-stationarity compensation, while the compensation was applied to the results in Fig. 2.6. By comparing Fig. 2.5(a) and Fig. 2.6(a) (or Fig. 2.5(b) and Fig. 2.6(b)), it can be seen that a spatial distortion in the shape of the microphone array is not visible when the non-stationarity compensation is applied.

In Fig. 2.7, the MUSIC power vector at 216 Hz is plotted on the $z = 0$ plane: the vector in Fig. 2.7(a) was reshaped into a matrix whose $i, j$-th element represents the $i, j$-th measurement point on the $x$-$y$ plane as shown in Fig. 2.7(b). Two source locations can be identified from the positions of the local maxima of the MUSIC power: those locations correspond to vector indices, $n = 15$ and $n = 19$. Note that the two locations are close to the contact patch region.

The MUSIC power at 216 Hz was then calculated on projection planes from $z = -0.1$ to 0.1 m as shown in Fig. 2.8(a). The MUSIC powers at $n = 15$ and $n = 19$, i.e., at the two source locations as identified from the results of Fig. 2.7, are plotted as a function of $z$ in Fig. 2.8(b). Note that the two plots in Fig. 2.8(b) are cross-sectional views of Fig. 2.8(a) when $n = 15$ and $n = 19$. Local maxima of the MUSIC power were found at $z = -0.091$ m for $n = 15$ and $z = -0.025$ m for $n = 19$. These locations lie behind the nominal source plane at $z = 0$ m, and these perhaps coincide with the acoustical centers of the actual sources.

Since data on the $x$-$y$ plane are available only at the discrete measurement points, an interpolation should, in principle, be performed to obtain continuous data on the reconstruction plane. To avoid the complexities introduced by an interpolation function, however, it is here assumed that a virtual reference may only be placed at a discrete measurement point. In the latter case the virtual reference locations on the $x$-$y$ plane did not change with small variations of $z$-location (e.g., see Fig 2.8(a)) since the $x$-$y$ resolution as determined by the distance between the discrete measurement points was relatively coarse compared with the resolution in $z$-direction. Thus, the locations of virtual references in the $x$-$y$ plane were first determined from the maxima of MUSIC power on the $z = 0$ surface: e.g., see Fig. 2.7(b). The optimal reference locations were then identified as those points at which the MUSIC power was maximized as a function of $z$ at the corresponding location in the $x$-$y$ plane: e.g., see Fig. 2.8(b).

The partial pressure fields shown in Fig. 2.9 were obtained by using real references, while those in Fig. 2.10 were obtained by using optimal virtual references. Note that the partial pressure fields in Fig. 2.9 are identical with the partial fields in Fig. 2.6 and that the total pressure fields in Figs. 2.9(c) and 2.10(c) were calculated as the quadratic summation of the two pressure fields. The partial fields obtained by using real references cannot be interpreted clearly in terms of the physical sources (see Fig. 2.9). However, it can be seen that the partial pressure fields decomposed by using virtual references can be associated with the physically meaningful sources (see Fig. 2.10): the first partial pressure field decomposed by using the virtual references can be associated with the sound radiating from the sidewall near the contact patch area, and the second field can be associated with the sound radiating from the treadband (in particular, from the trailing edge of the horn shape formed between the tire treadband and the ground). Note that the total fields shown in both Figs. 2.9(c) and 2.10(c) are identical even though the individual partial fields are decomposed by using different sets of references.

The auto-spectrum averaged over all the reference microphones is shown in Fig 2.11: the frequency range is from 0 to 1200 Hz in Fig. 2.11(a), while in Fig. 2.11(b) it is zoomed from 0 to 200 Hz. Here, harmonic peaks that are close to each other at an approximate interval of 6 Hz are associated with the period of tire revolution.

The reconstructed pressure, particle velocity, active intensity, and reactive intensity on the source plane (i.e., $z = 0$) are shown in Figs. 2.12 to 2.18: the latter three properties are in $z$-direction. Frequencies were here chosen at various peaks in the reference spectrum (see Fig. 2.11). Note that the active sound intensity has generally both positive and negative values in the $x$-$y$ plane although the total radiated power, calculated from the summation of active sound intensity multiplied by the associated area, is positive. At very low frequencies (48 and 86 Hz) in Figs. 2.12 and 2.13, it can be seen that the motion of the tire sidewall is distinctive (see particle velocity in the $z$-direction labeled (b)). The sound radiation, represented here by active intensity, is also significant from the sidewall, but the maximum sound radiation is from the region close to the contact patch. From Figs. 2.14 to 2.17, the modal response of the tire is clearly visible in the particle velocity fields: the circumferential mode number, $n$, is equal to 2, 3, 4, and 5 at 102, 128, 156, and 183 Hz, respectively. Regardless of the modal response, most sound radiation is again from the contact patch region. Finally, it can be seen from the reconstructed sound fields at 1053 Hz in Fig. 2.18, showing representative high frequency behavior, only the contact patch region is important in terms of both vibration response and sound radiation.

## 2.5 Conclusions

In this chapter, multi-reference, scan-based NAH has been formulated using a mathematical description that explicitly features the acoustic transfer function between the references and the field points. Based upon the present description, a procedure to compensate for source non-stationarity was proposed. In addition, a post-processing procedure has been described that makes it possible to identify virtual reference signals that can be used to identify physically meaningful partial fields *after* performing a holographic measurement based on a non-optimal, but sufficient, reference set. It was shown through a rolling tire experiment that the proposed compensation procedure reduces the spatial noise resulting from source non-stationarity and that the proposed optimal reference procedure can be used to separate the sound radiation from the sidewall and the horn region. It was also shown that the NAH procedure along with the compensation procedure for source non-stationarity successfully visualized the vibration response and sound radiation of the rolling tire. At low frequencies, modal response of the tire was visible; however, most sound radiation is from the region close to contact patch at both low and high frequencies.

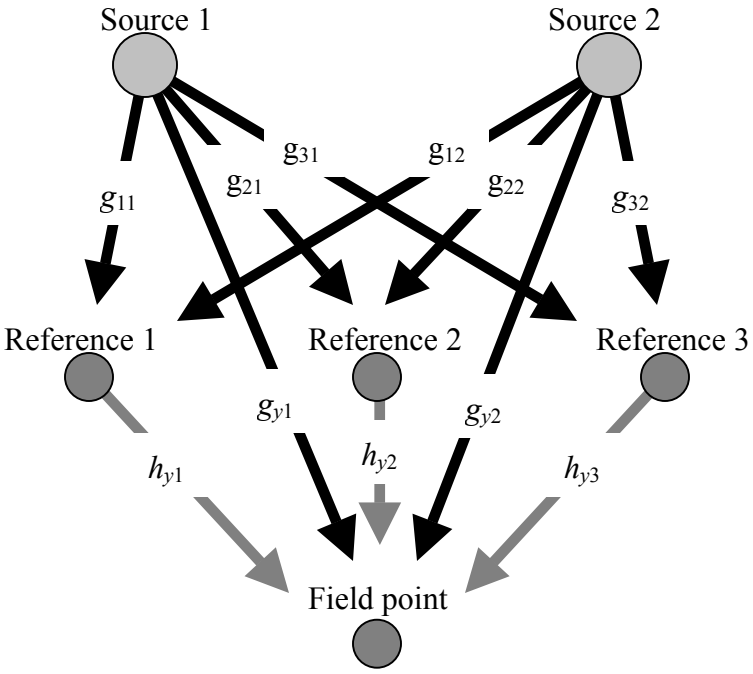


Figure 2.1: Geometrical relations between sources, references, and field points and the associated transfer functions.

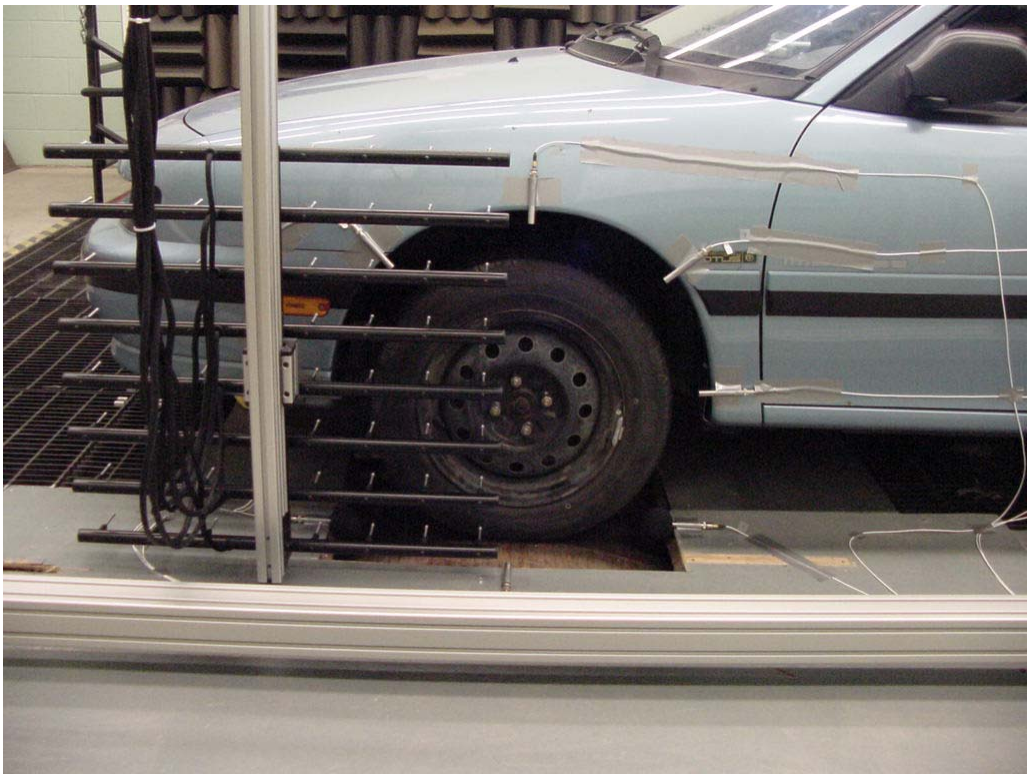

Figure 2.2: Photograph of experimental setup: tire (that is driven by a roller), reference microphones, and scanning microphone array are shown.

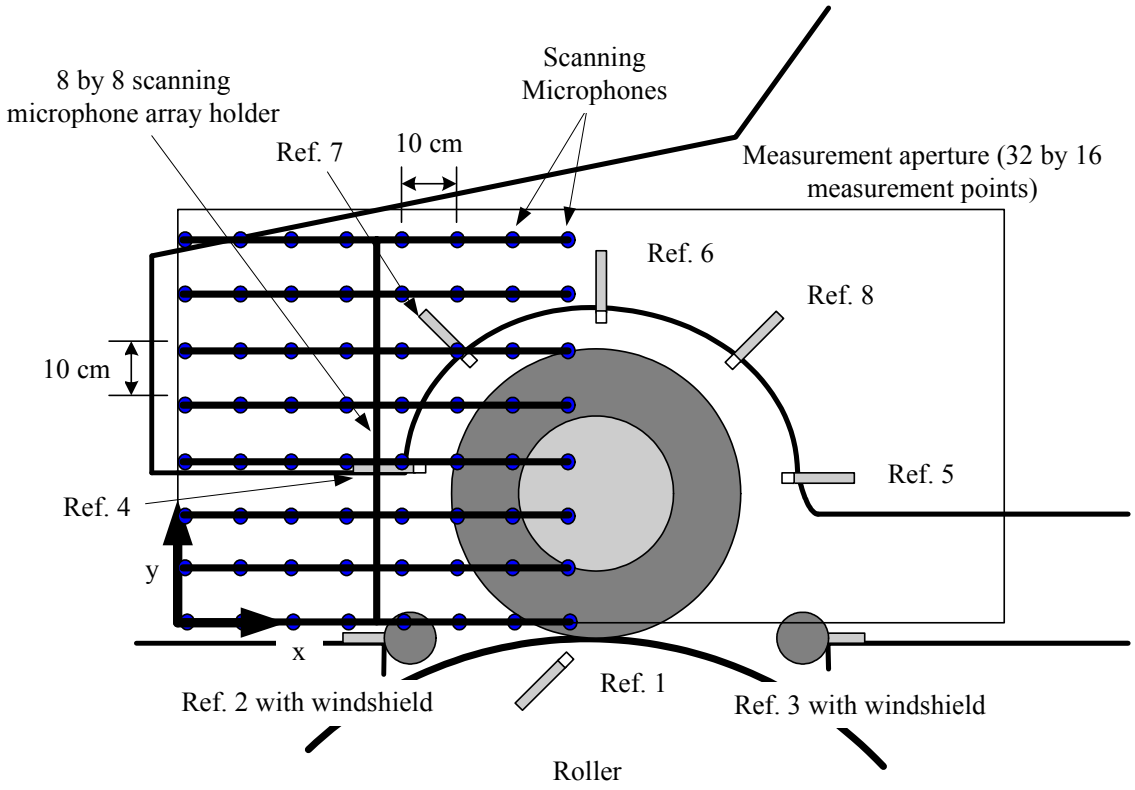


Figure 2.3: Sketch of experimental setup used for holographic measurements on rolling tire.

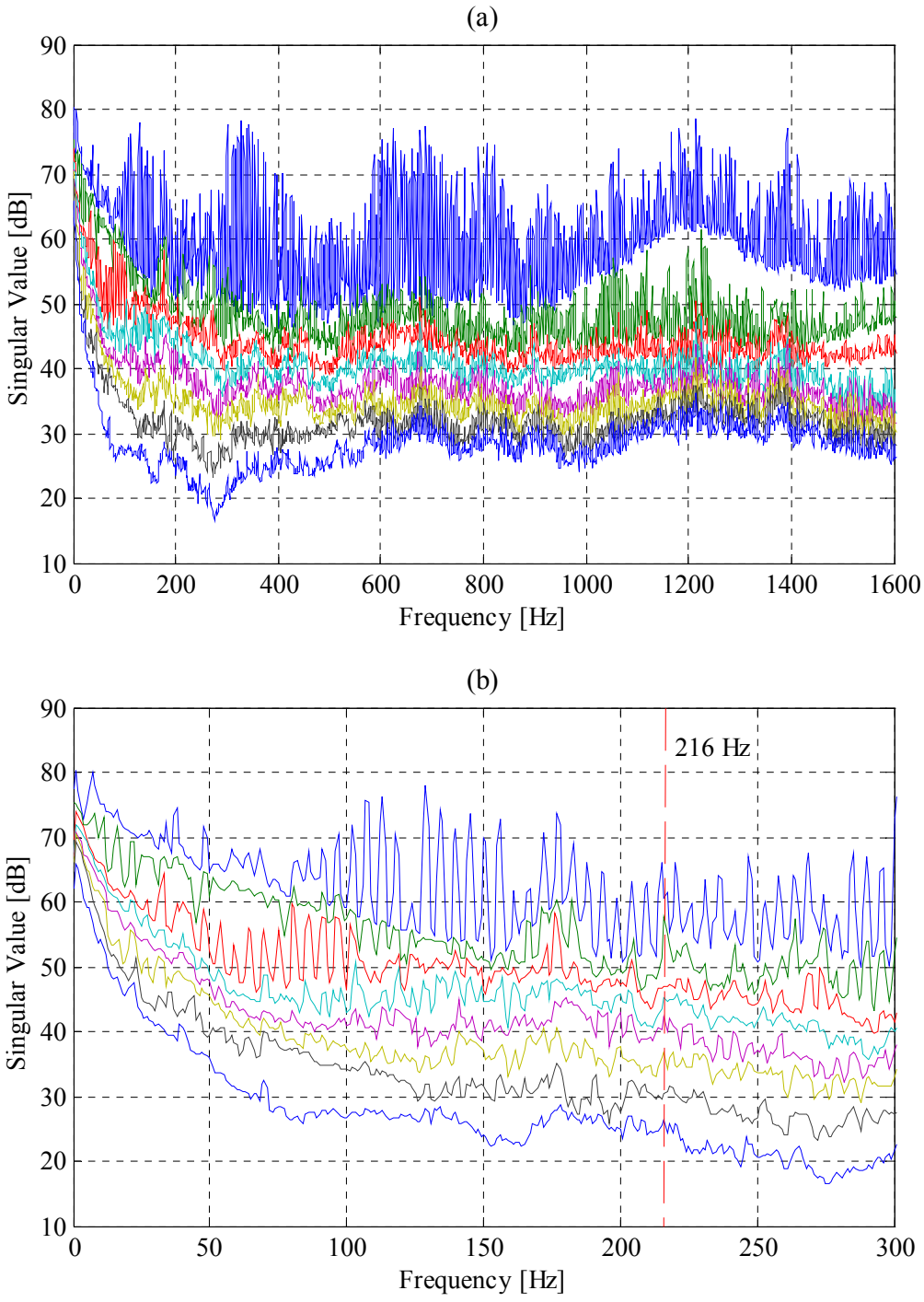


Figure 2.4: Singular value spectra of reference cross-spectral matrix: (a) from 0 to 1600 Hz, and (b) zoomed from 0 to 300 Hz.

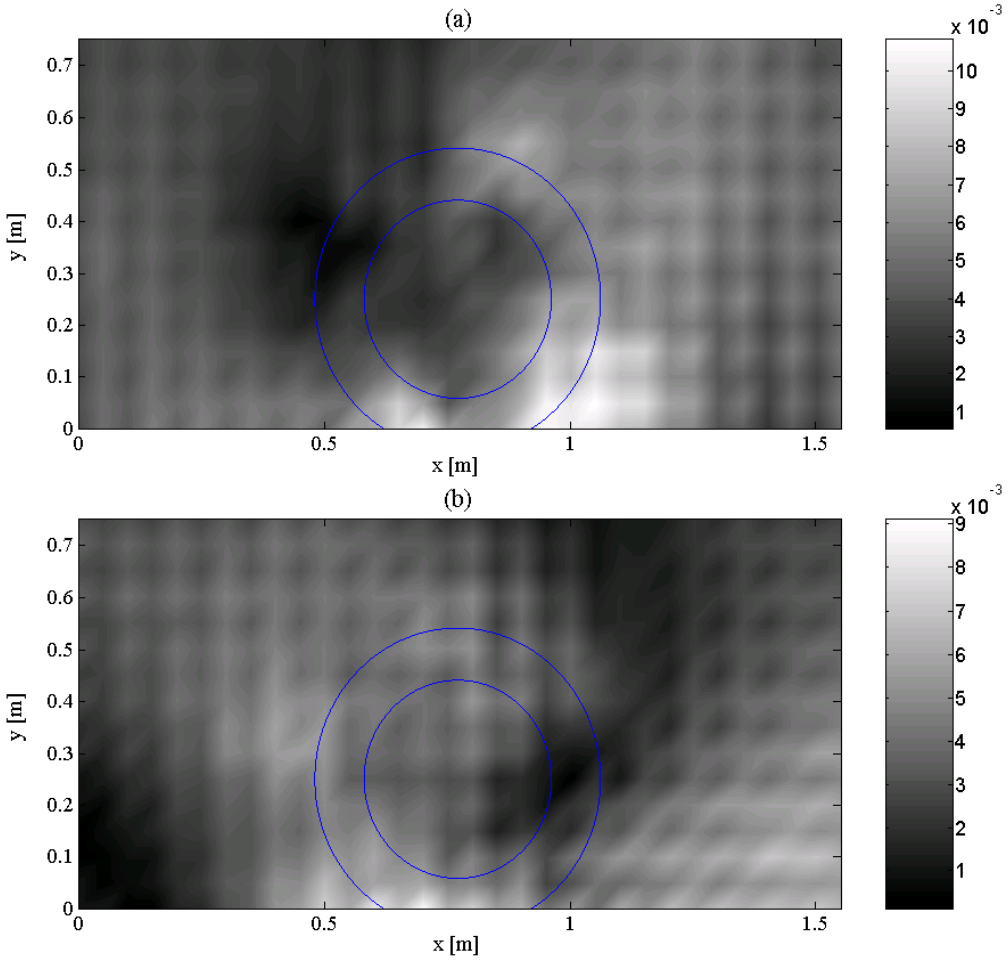


Figure 2.5: Partial pressure fields on hologram surface at 216 Hz without source non-stationary compensation (decomposed by using real references combined with SVD procedure): (a) 1st partial field and (b) 2nd partial field.

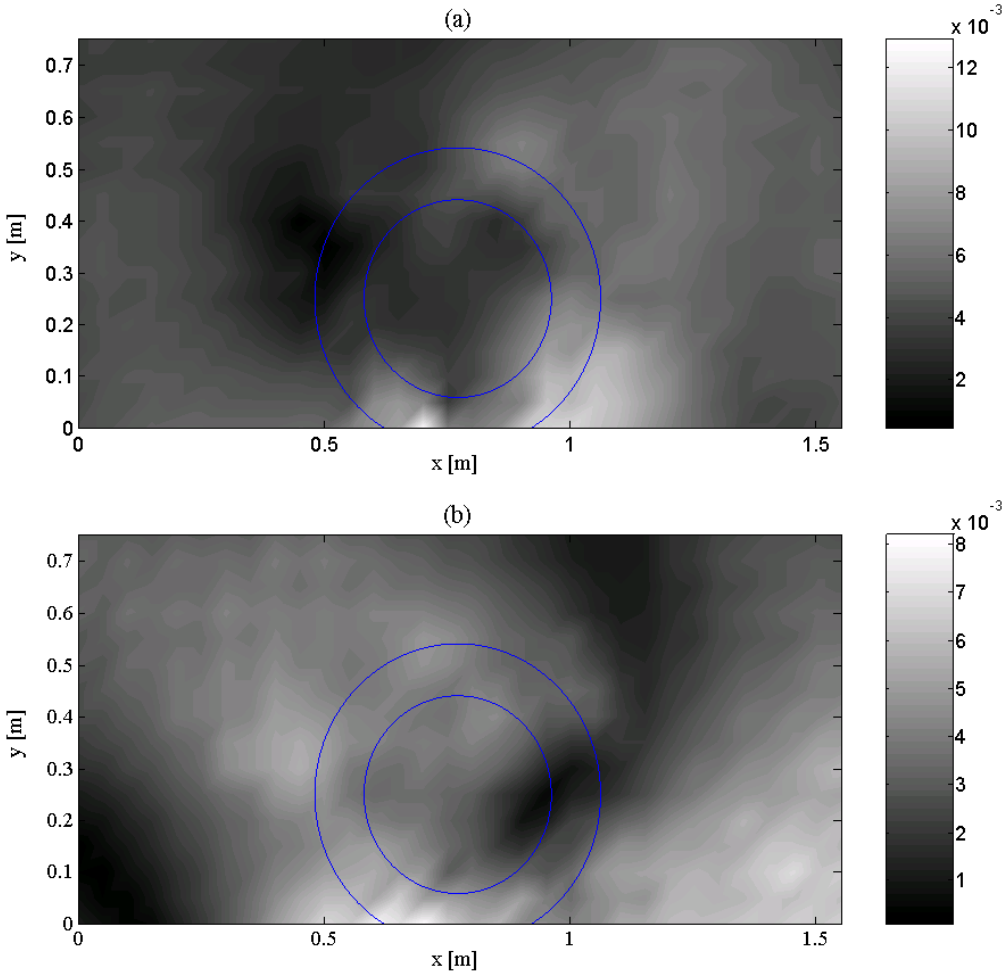


Figure 2.6: Partial pressure fields on hologram surface at 216 Hz with source non-stationary compensation (decomposed by using real references combined with SVD procedure): (a) 1st partial field and (b) 2nd partial field.

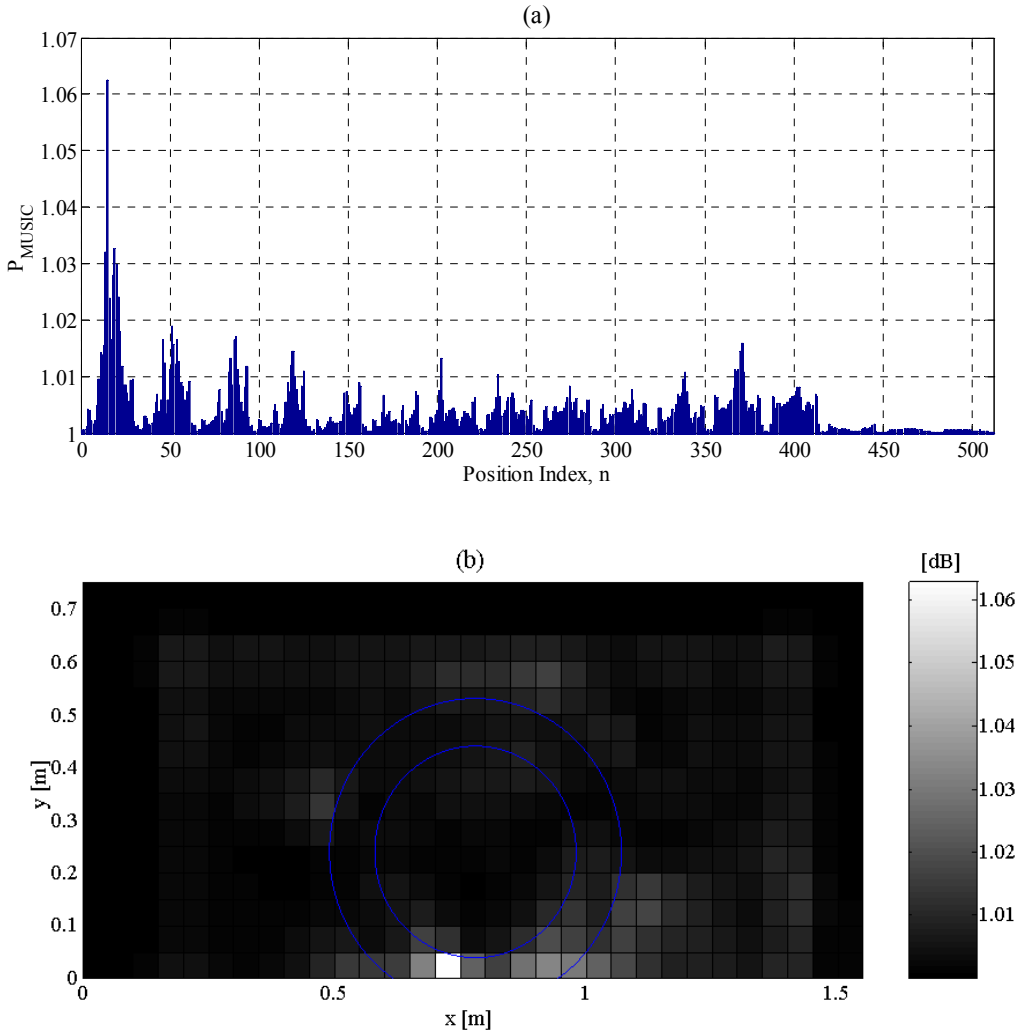


Figure 2.7: Music power at 216 Hz on the source plane ($z$ = 0 m): (a) represented by the function of position index, $n$ (maxima at $n$ = 15 and 19) and (b) mapped on $x$-$y$ plane at 216 Hz.

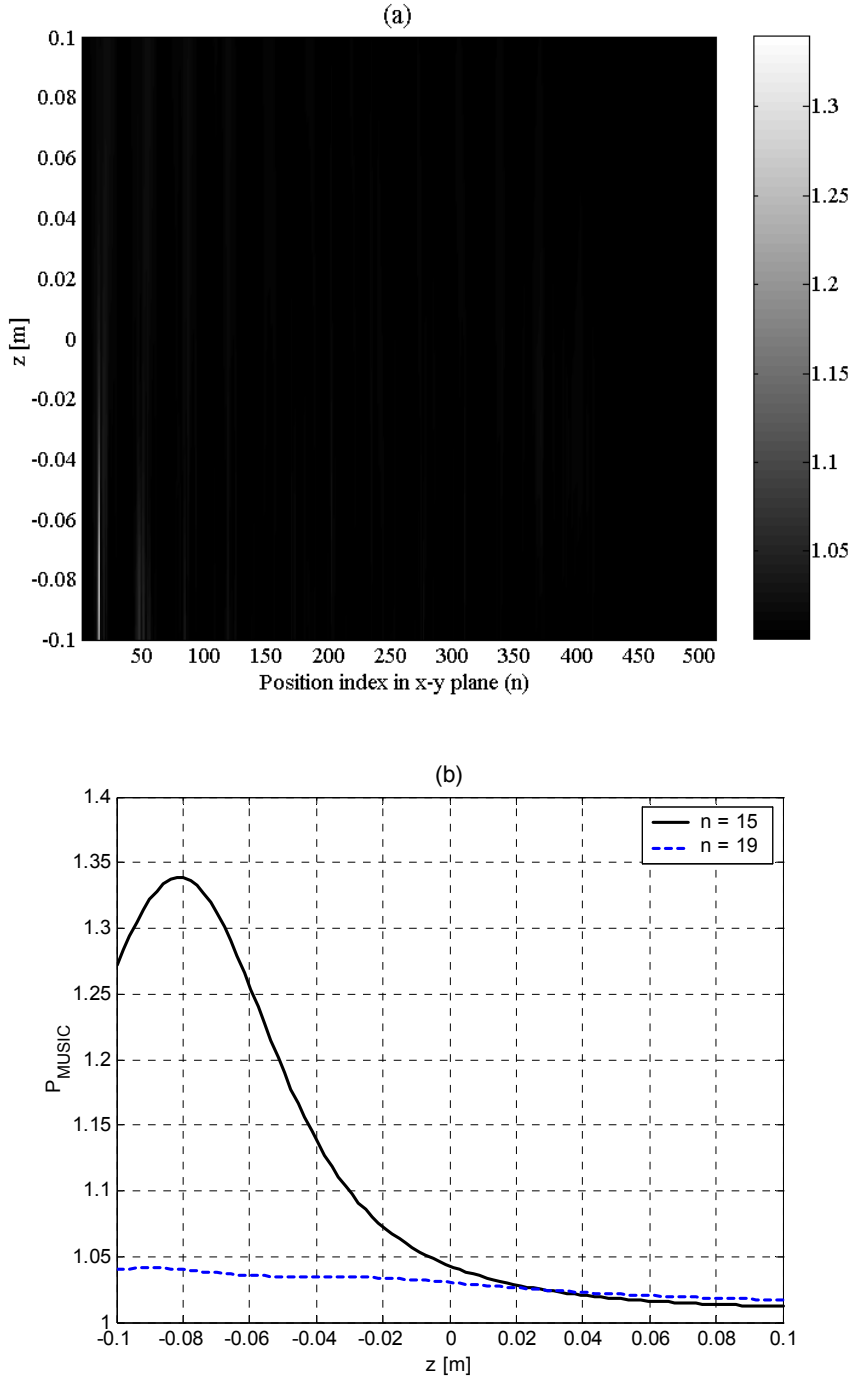


Figure 2.8: Music power at 216 Hz: (a) as a function of $n$ = 1 to 288 and $z$ = -0.1 to 0.1 m, and (b) plotted from $z$ = -0.1 to 0.1 m when $n$ = 15 (MAX($P_{MUSIC}$) = 1.3386 at $z$ = -0.0818 m) and when $n$ = 19 (MAX($P_{MUSIC}$) = 1.0414 at $z$ = -0.0904 m).

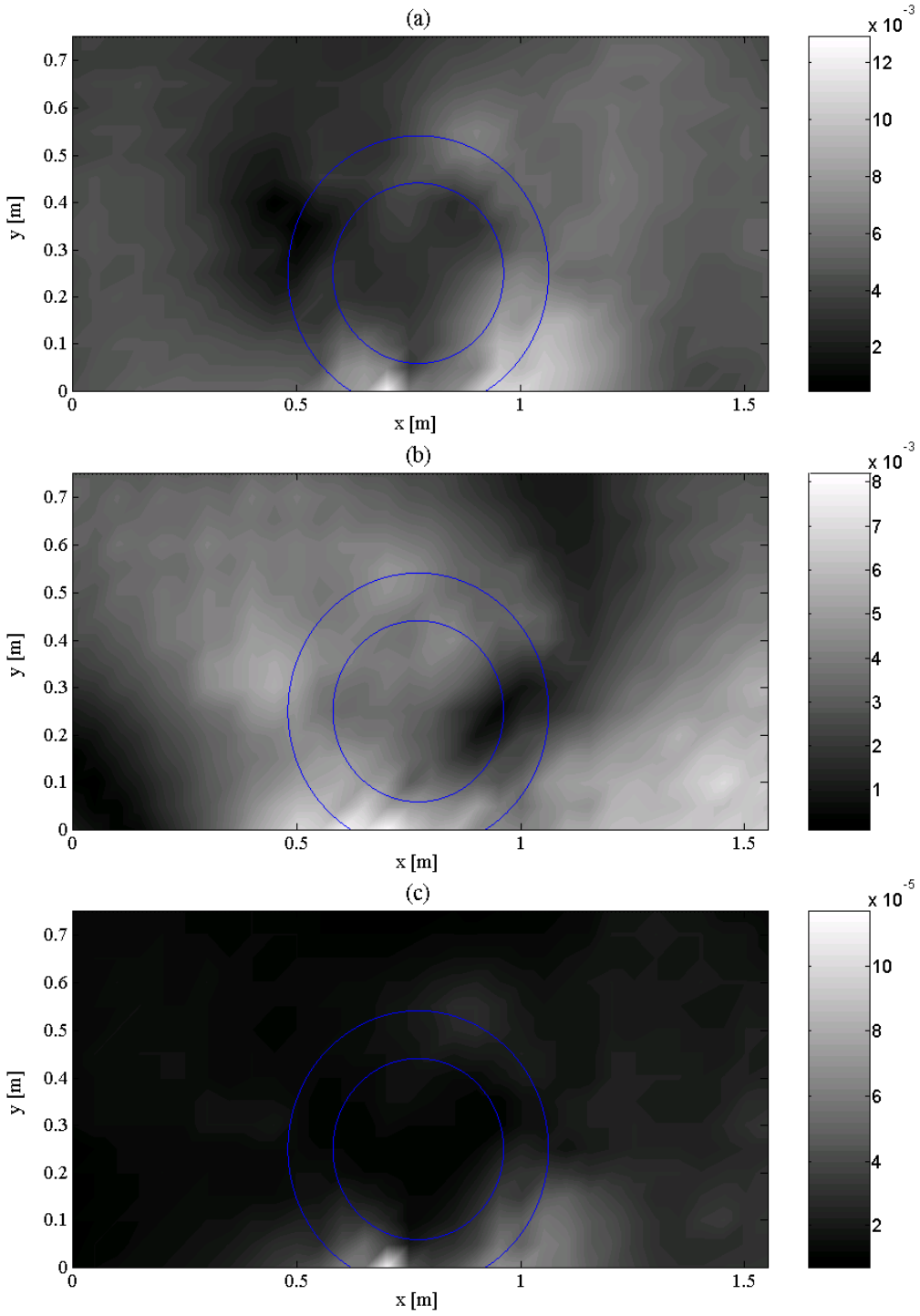


Figure 2.9: Partial pressure fields on hologram surface at 216 Hz decomposed by using real references combined with SVD procedure: (a) 1st partial pressure field, (b) 2nd partial pressure field, and (c) total pressure field (i.e., quadratic summation of the two partial fields).

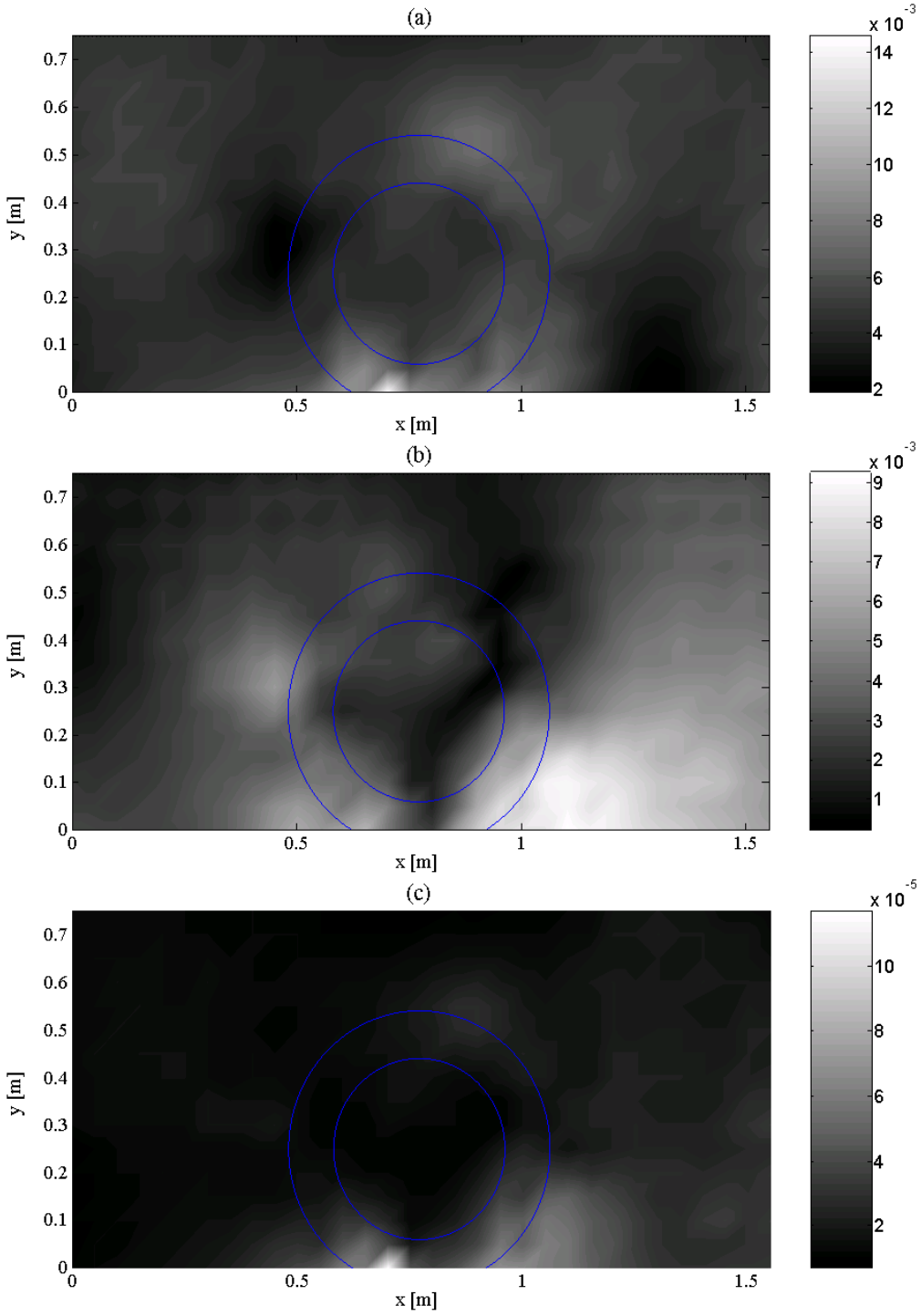


Figure 2.10: Partial pressure fields on hologram surface at 216 Hz decomposed by using optimal virtual references combined with SVD procedure: (a) 1st partial pressure field, (b) 2nd partial pressure field, and (c) total pressure field (i.e., quadratic summation of the two partial fields).

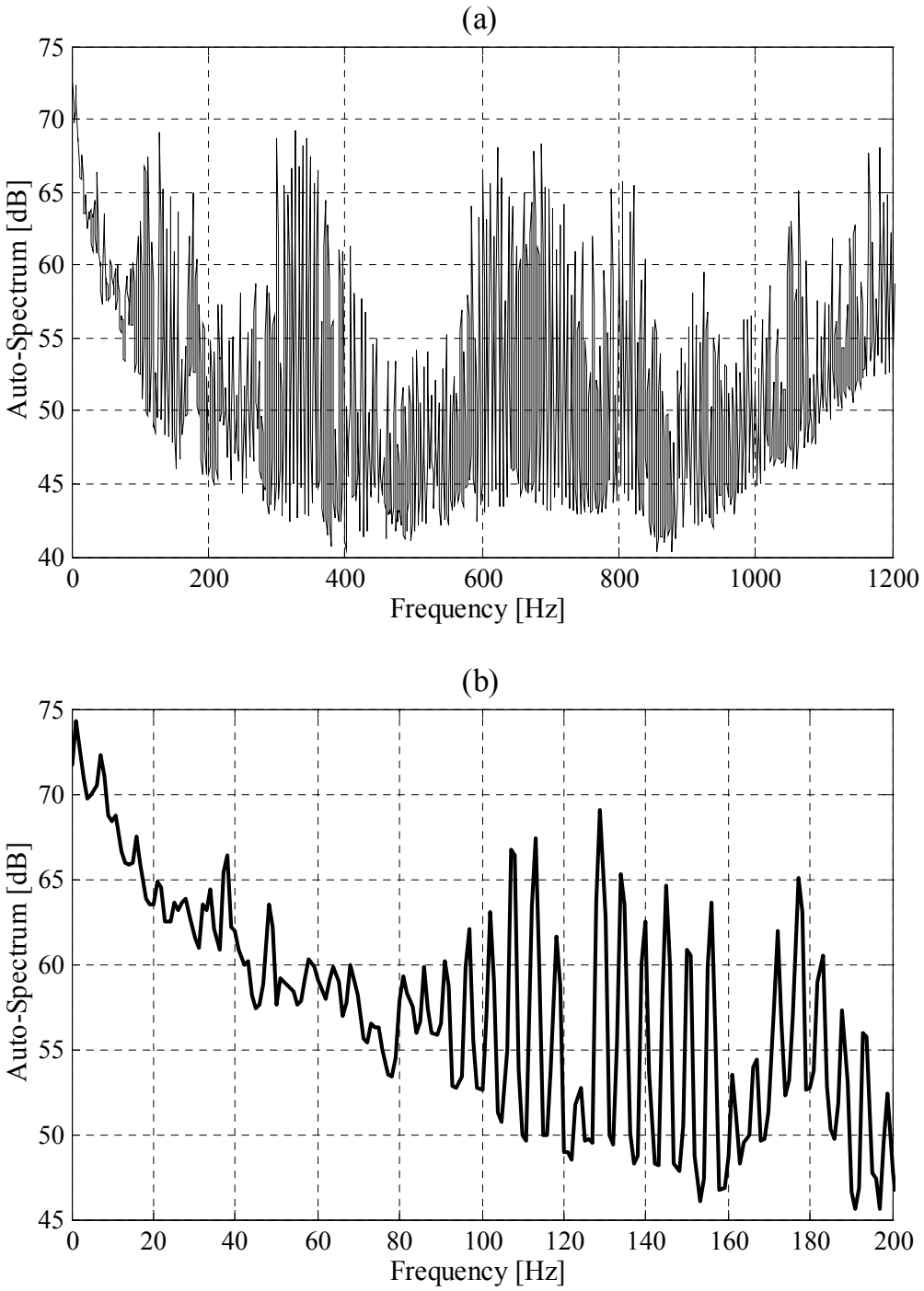


Figure 2.11: Auto-spectrum averaged over all reference microphones (21 mph): (a) from 0 to 1200 Hz and (b) zoomed from 0 to 200 Hz.

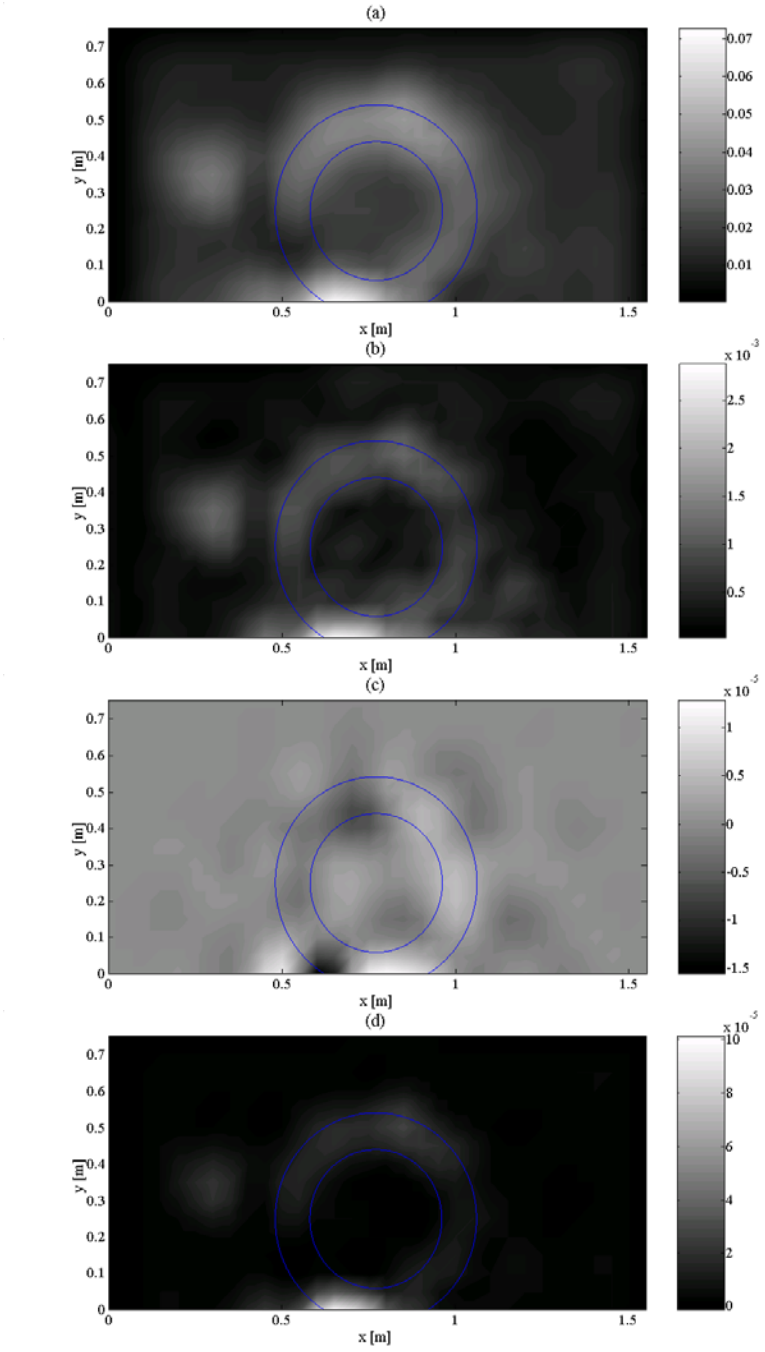


Figure 2.12: Projected sound fields on source plane ($z = 0$) at 48 Hz: (a) acoustic pressure, (b) particle velocity in $z$-direction, (c) active sound intensity in $z$-direction, and (d) reactive sound intensity in $z$-direction.

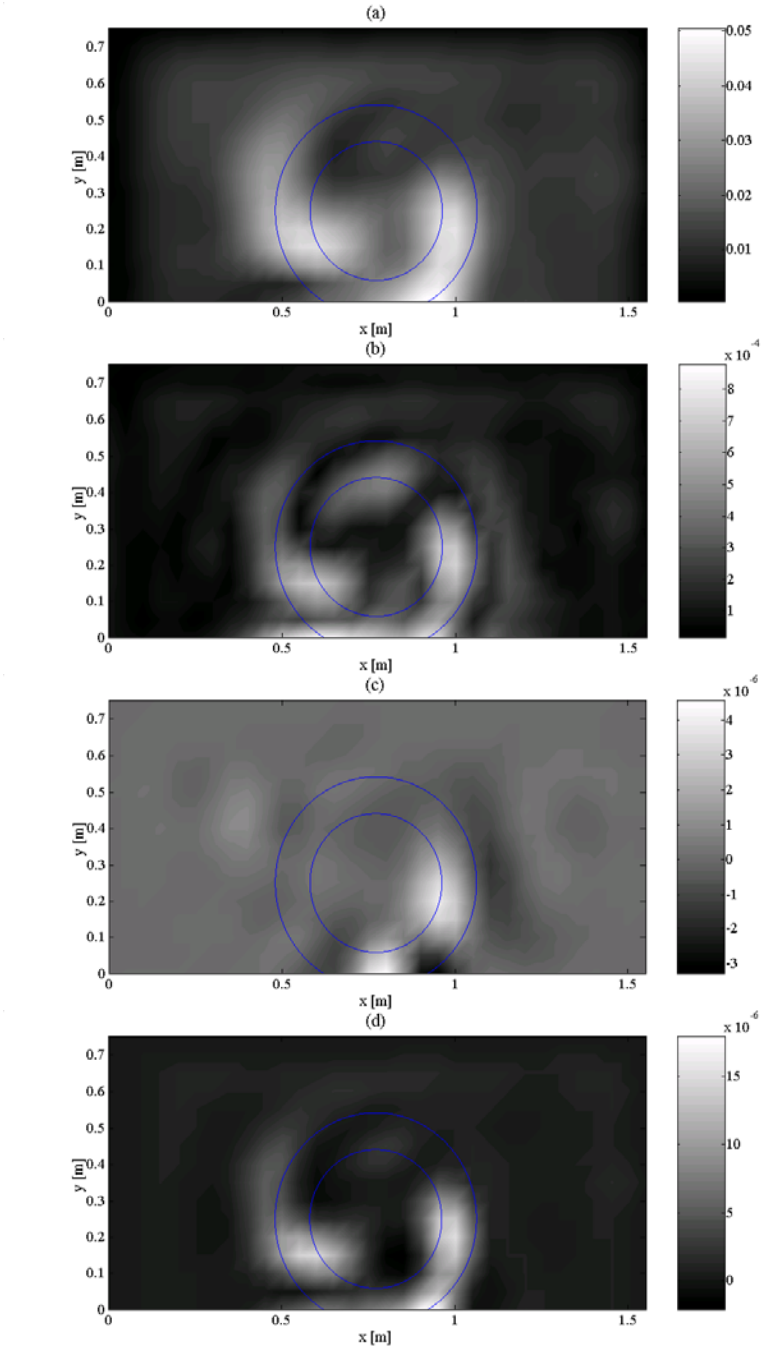


Figure 2.13: Projected sound fields on source plane ($z = 0$) at 86 Hz: (a) acoustic pressure, (b) particle velocity in $z$-direction, (c) active sound intensity in $z$-direction, and (d) reactive sound intensity in $z$-direction.

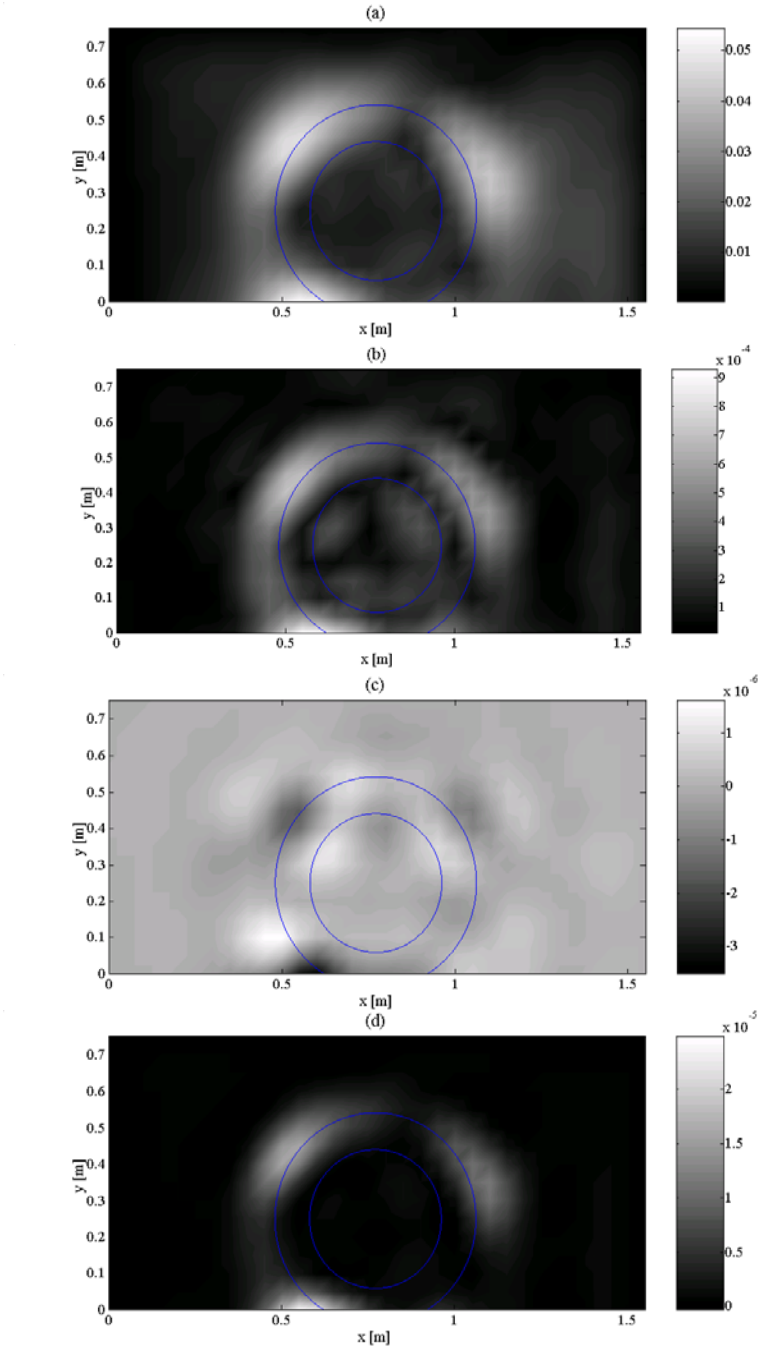


Figure 2.14: Projected sound fields on source plane ($z$ = 0) at 102 Hz: (a) acoustic pressure, (b) particle velocity in $z$-direction, (c) active sound intensity in $z$-direction, and (d) reactive sound intensity in $z$-direction.

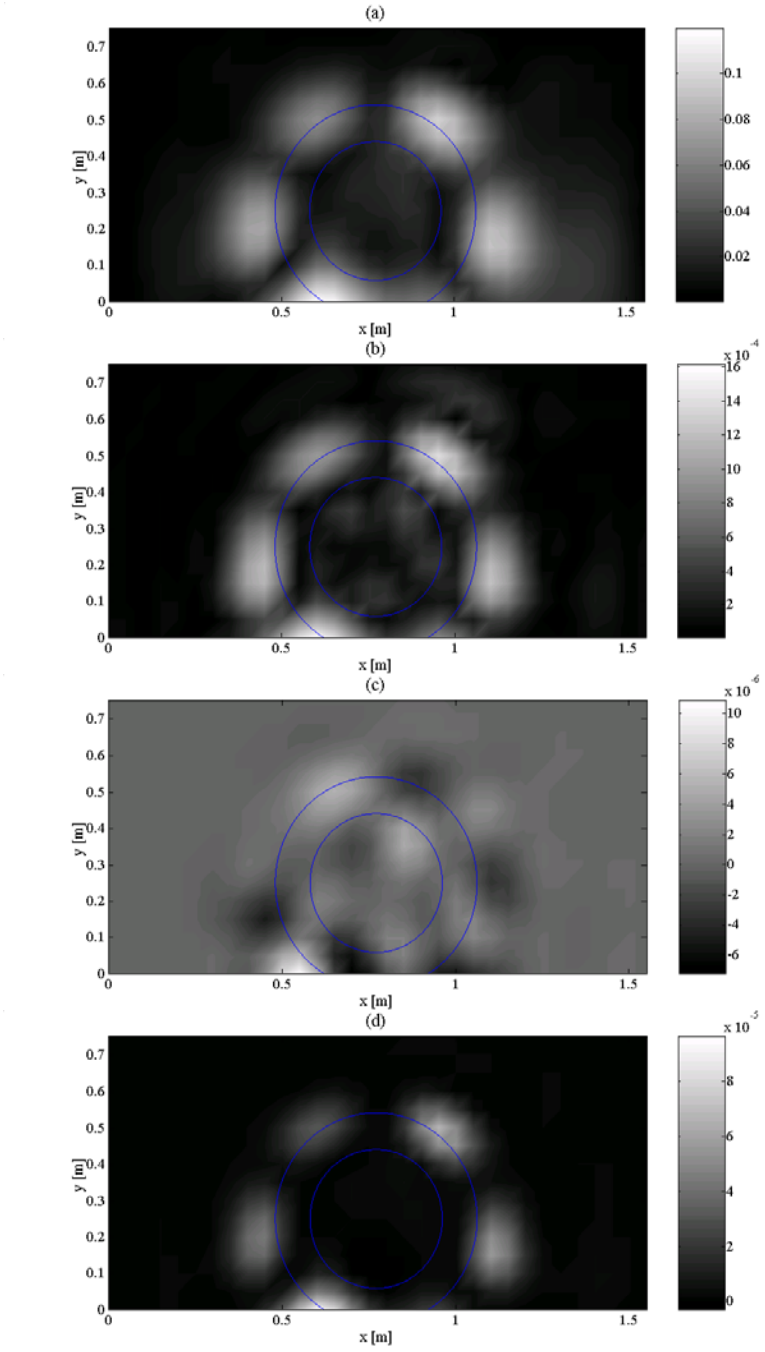


Figure 2.15: Projected sound fields on source plane ($z$ = 0) at 128 Hz: (a) acoustic pressure, (b) particle velocity in $z$-direction, (c) active sound intensity in $z$-direction, and (d) reactive sound intensity in $z$-direction.

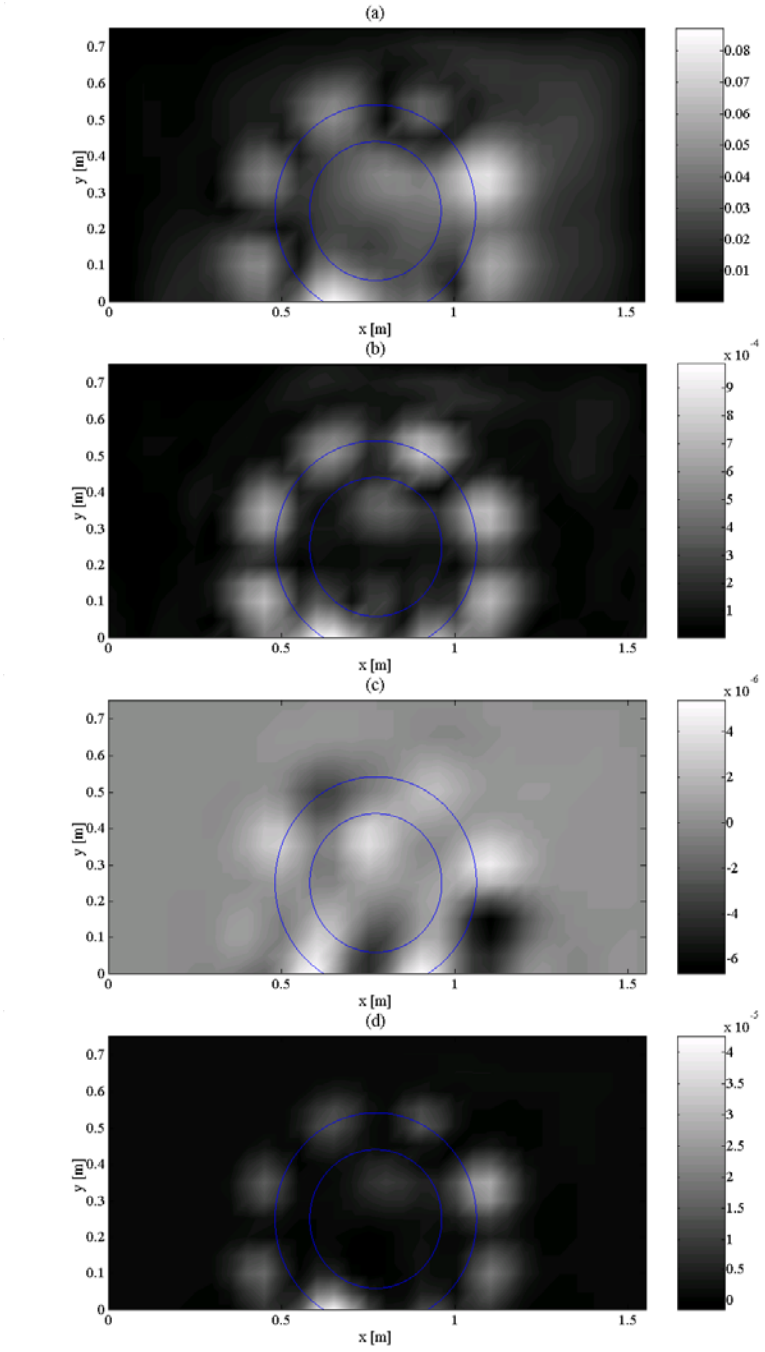


Figure 2.16: Projected sound fields on source plane ($z$ = 0) at 156 Hz: (a) acoustic pressure, (b) particle velocity in $z$-direction, (c) active sound intensity in $z$-direction, and (d) reactive sound intensity in $z$-direction.

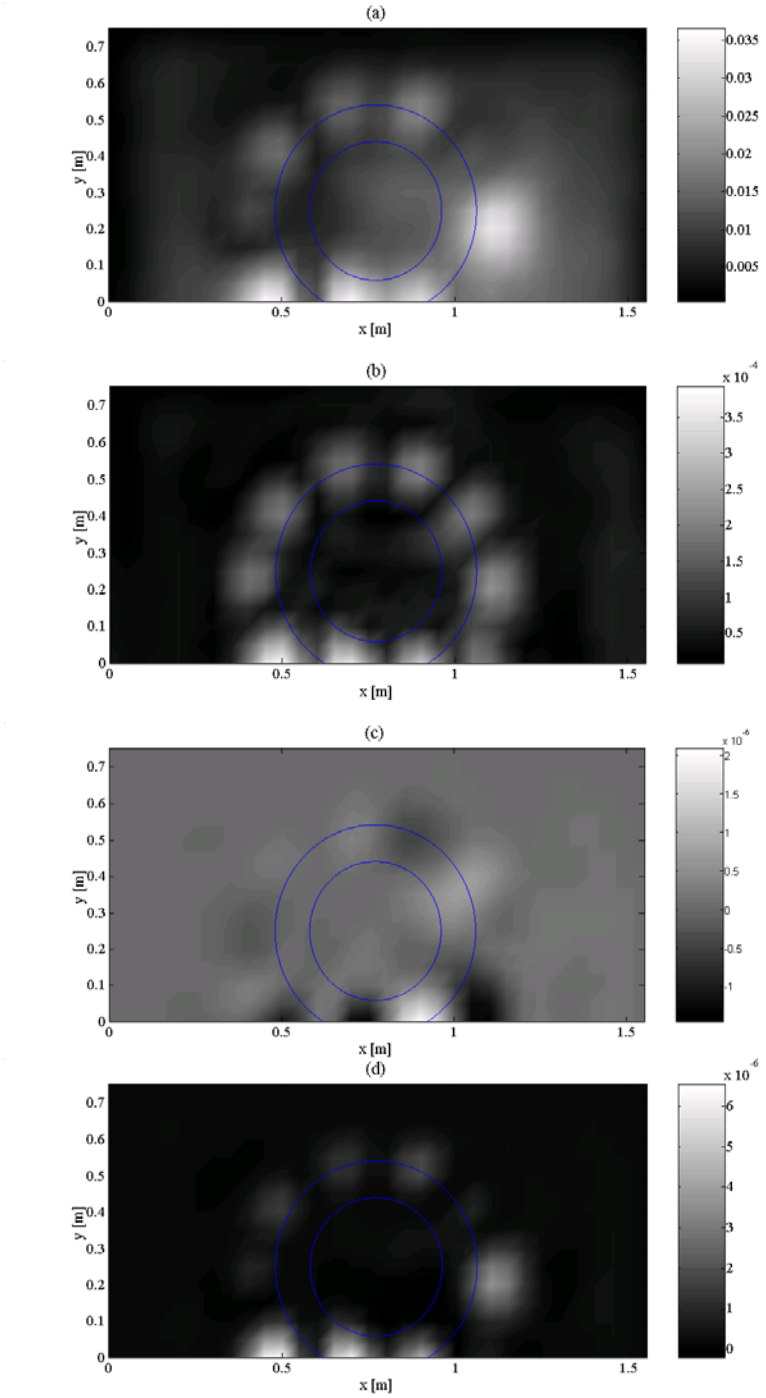


Figure 2.17: Projected sound fields on source plane ($z$ = 0) at 183 Hz: (a) acoustic pressure, (b) particle velocity in $z$-direction, (c) active sound intensity in $z$-direction, and (d) reactive sound intensity in $z$-direction.

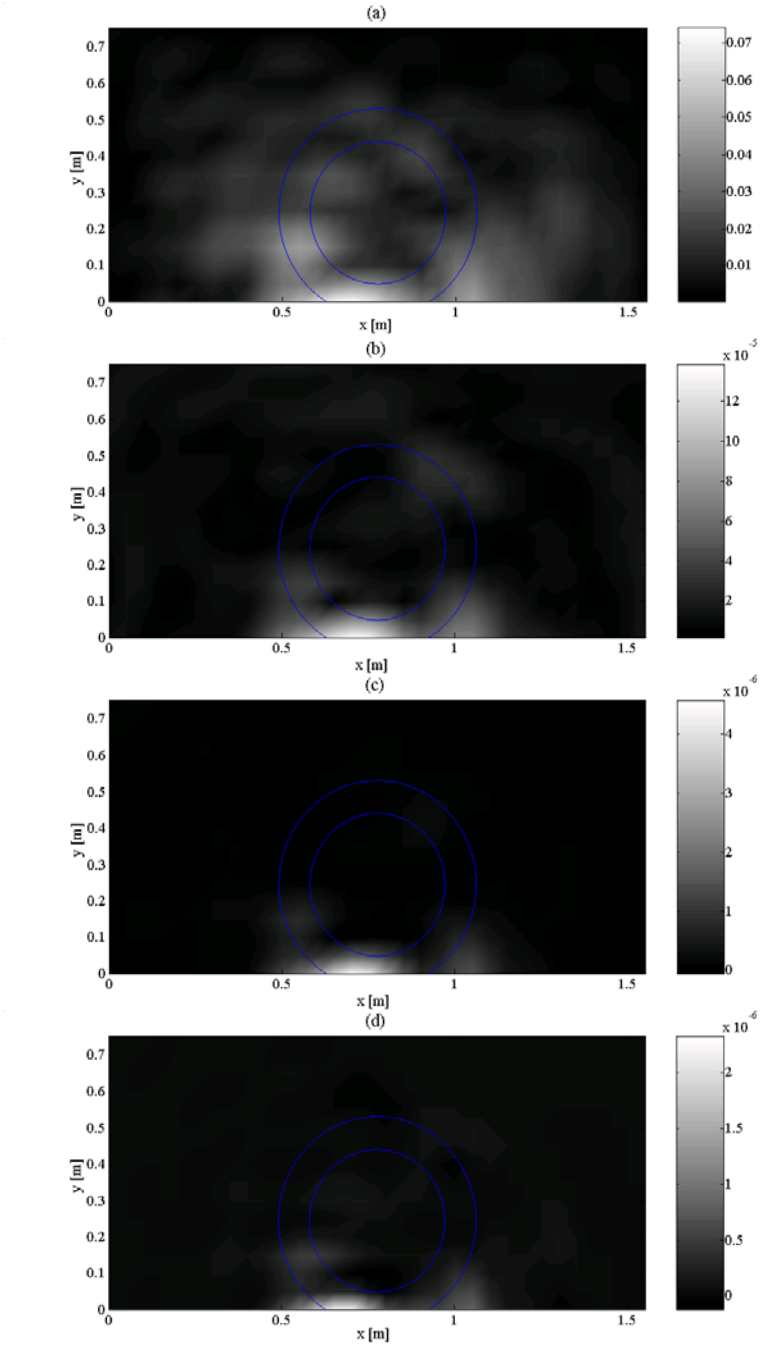


Figure 2.18: Projected sound fields on source plane ($z$ = 0) at 1053 Hz: (a) acoustic pressure, (b) particle velocity in $z$-direction, (c) active sound intensity in $z$-direction, and (d) reactive sound intensity in $z$-direction.

# 3. MEASUREMENT OF STATIONARY TIRE VIBRATION

In the last chapter, techniques for visualizing the sound field radiated by a tire were described. In this chapter, procedures for visualizing and characterizing the vibration of stationary tires are considered. In particular, the use of both non-parametric and parametric wave number decomposition techniques to characterize tire vibration is described. When a tire was driven radially at a point on its treadband, measurements of the resulting radial treadband vibration were made around the treadband circumference by using a laser Doppler velocimeter. By performing a circumferential wave number decomposition of the space-frequency data, the propagation characteristics of the waveguide modes that contributed to the response of a tire could be visualized. However, to obtain quantitative estimates of the real and imaginary dispersion relations for each of these modes, an iterative Prony series approach has been used: techniques for using the iterative Prony procedure successfully are described in detail, particularly with regard to model order selection and the identification of parameter starting values. By curve-fitting to the resulting data, it is possible to obtain estimates of wave velocity and attenuation rate on a mode-by-mode basis.

## 3.1 Introduction

It is now well known that tire/road interaction noise can contribute significantly to passenger vehicle passby noise levels. As a result, tire/road interaction noise has been the subject of many investigations. In this chapter, tire vibration and its relation to sound radiation are the primary focus. In particular, in the work to be described here, wave number decomposition techniques [21,42] have been applied to the experimental analysis of the vibration of a stationary tire.

In the experiments to be described here, a stationary tire was driven radially at a point on its treadband by using a small shaker. Measurements of the resulting radial

treadband vibration were then made around the treadband circumference by using a laser Doppler velocimeter. By a direct inspection of the resulting space-frequency data, it was possible to identify the frequency ranges in which the tire responded either modally or non-modally. However, by performing a circumferential wave number decomposition of the space-frequency data, it was in addition possible to identify the wave types that contributed significantly to the vibration response of the tire in the frequency range considered here [43]. The results to be presented below suggest that the vibration response of a typical passenger car tire below 1 kHz is controlled by a small number of relatively slowly propagating waveguide modes that are primarily associated with flexural motion of the treadband, and a faster mode associated with extension of the treadband. Each of these modes can be associated with a particular cross-sectional mode shape, and thus it was concluded that tires could be effectively modeled as waveguides.

Emphasis was also placed on estimating quantitative information about the propagating tire modes: in particular their wave speeds and attenuation rates. Previously, non-parametric, i.e., FFT-based, circumferential wave number decomposition techniques were used to characterize tire vibration. But in that case the spatial Fourier transform yields only the real part of the dispersion relation, which then allows only the wave speed to be inferred. In addition, spatial transform procedures may suffer from poor resolution in the wave number domain. These various concerns have been addressed in the present work in which complex wave numbers were identified by fitting a Prony series, i.e., a sum of complex exponentials, to the spatial data. By doing so, it is possible to obtain complex dispersion relations and then the corresponding wave speeds and the spatial decay rates by curve fitting. Here, the conventional Prony method [44-47] has been supplemented by the application of an iterative Prony method [48-50]: the conventional Prony series method has been used to provide starting values for the iterative procedure. In this way, optimal performance in terms of estimation error and convergence speed is guaranteed and the propagating wave properties are identified precisely and quickly. In particular, “true” system modes can be easily distinguished from those associated with noise.

## 3.2 Experiments on a Stationary Tire

Figure 3.1 shows the measurement set-up that was used to measure the radial treadband

vibration. A Firestone P215/70R14 M+S tire was used in these measurements, and it was placed horizontally on a tire balancer as shown. The treadband was forced radially by a mini-shaker acting through a circular copper plate that had a diameter of 3.3 cm and which was bonded directly to the tire treadband. A PCB 208A03 force transducer was mounted to the copper plate and was connected through a stinger to the Brüel and Kjaer 810 mini-shaker that was mounted on an adjustable frame. That frame was itself attached to the wheel so that it could be rotated together with the tire. A counter weight was attached to the tire balancer to balance the weight of the drive arrangement.

The output of a random noise generator was passed through a Wavetek 852 bandpass filter and a QSC Model 1080 power amplifier before being delivered to the mini-shaker. The radial velocity of the treadband was measured along the circumference of the tire over the frequency range from 100 Hz to 1000 Hz by using a Polytec OFV-040 laser vibrometer and OFV 3000 controller. The responses from the force transducer and laser vibrometer were delivered to a Brüel and Kjaer 2032 signal analyzer after the former signal was amplified using a PCB 480D09 charge amplifier. A Matlab computer program was used to control the signal analyzer and to record all the necessary information.

The experiment was performed by driving the tire at the center of the treadband and measuring the velocities at two hundred and six equally spaced measurement locations along the center line of the treadband. As shown Fig. 3.2, small pieces of reflective tape were placed on the measurement points to ensure a good signal-to-noise ratio. To demonstrate the effect of inflation pressure, measurements were made at both 20 psi and 40 psi inflation pressures using air to inflate the tire.

## 3.3 Spatial Fourier Transform

The complete data set resulting from each measurement (i.e., radial velocity normalized by the input force versus frequency) was arranged in matrix form for further analysis. The normalized radial velocity in each set was further normalized with respect to drive-point velocity at each frequency. Data at three frequencies are shown in Fig. 3.3 and complete space-frequency data sets at two inflation pressures are shown in Fig. 3.4. Note that the magnitude of the normalized velocity is plotted in a decibel scale, and that the circumferential angle $\theta = 0$ deg. corresponds to the drive point.

To present the experimental results in the wave number domain, the normalized

radial velocity at each frequency can be expressed as

$$v(p,q) = \frac{1}{N}\sum_{m=0}^{N-1} V(p,m)\exp\left(jk_m q\Delta s\right) \tag{3.1}$$

where $v(p,q)$ is the measured velocity at the $p$-th frequency and $q$-th circumferential position, $N$ is the total number of measurement points along the center of treadband, $\Delta s$ is the spatial sampling interval, $k_m$ is the $m$-th circumferential wave number given by $k_m = 2\pi m/(N\Delta s)$, $V(p,m)$ is the amplitude of velocity in the wave number domain at the $p$-th frequency, and $m$-th circumferential wave number, and $j$ is the unit complex number. Note that each component of $V$ represents a disturbance propagating around the tire at a rate controlled by the circumferential wave number. Equation (3.1) represents the inverse discrete Fourier transform and thus $V(p,m)$ can be calculated from the forward discrete Fourier transform: i.e.,

$$V(p,m) = \sum_{q=0}^{N-1} v(p,q)\exp\left(-jk_m q\Delta s\right). \tag{3.2}$$

Frequency-wave number decompositions, i.e., plots of $|V(p,m)|$ versus frequency and circumferential mode number, at two inflation pressures are shown in decibel form in Fig. 3.5 (the circumferential mode number is obtained by multiplying together the circumferential wave number and the radius of the tire.). The various curving tracks are associated with disturbances propagating around the circumference of the tire. Note also that standing circumferential modes appears as bright spots in this form of plot. The group speed of propagating disturbances can be calculated as:

$$c_g = \frac{\partial\omega}{\partial k_m} \tag{3.3}$$

Lines corresponding to various group speeds have been superimposed on Fig. 3.5.

The normal acceleration as a function of cross-sectional position (see Fig. 3.6) was measured at one circumferential position ($\theta$ = 45 deg.) by using a roving accelerometer: results at two frequencies are shown in Fig. 3.7. Note that the 0 cm position corresponds to one rim, and 41 cm corresponds to the other. The width of the treadband itself was approximately 18 cm so that the “shoulders” of the tire were near the 10 cm and 30 cm positions.

## 3.4 Prony Series Identification

### 3.4.1 Introduction

When a complex wave number is used to represent a spatially attenuated wave such as the measured data shown in Fig. 3.3, its imaginary part accounts for the spatial attenuation. Thus, it is appropriate to identify the spatially attenuated wave by using a series of complex exponential functions whose exponents are themselves complex. This exponential series identification method, the Prony method, is very well known [44-47]. In the conventional implementation of the Prony method, a relatively large number of exponential terms (i.e., a large model order) is used so as to include roots that are necessary to model measurement noise. Because the bias error of the wave number estimate due to measurement noise decreases as the model order is increased, the model order must be as large as possible. To distinguish "true" roots from noise-related roots, Braun and Ram [46] have proposed a perturbation method that requires an in-depth understanding of the movement range associated with each type of root.

Here the iterative Prony method proposed by Therrien and Velasco [48] was used instead. This procedure can be used to find a Prony series representation of the spatial data that minimizes an estimation error norm. Therefore, without large bias error, it can be used to identify Prony parameters with slightly lager model order than the number of true roots. There are two concerns associated with this iterative scheme, however. The first concern is how to determine the model order. The second concern is that the error norm itself is not a quadratic function; all quadratic functions possess a unique optimal point where the value of the error norm is the local as well as the global minimum so that in that case the iterative optimization method would always yields the optimal solution regardless of the starting point. To resolve the former concern, a singular value decomposition procedure was used: this procedure is well established for the conventional Prony method [46,47] and can be also applied in conjunction with the iterative method to estimate an appropriate model order. To resolve the second concern, it is necessary to select parameter starting values close to their optimal values to guarantee an optimal solution regardless of error norm definition. In the present case, parameter starting values were selected from amongst the solutions of the conventional Prony method. The convergence characteristics of the iterative procedure were guaranteed in this way.

### 3.4.2 Iterative Prony Method

The discrete and finite sized data set measured at the $N$ equally spaced points can be approximated by a complex exponential series written in matrix form: i.e.,

$$f(x_n) = \sum_{m=1}^{M} c_m \exp(ik_m x_n) + e(x_n), \tag{3.4}$$

where $f(x_n)$ is the measured data at the $n$-th measurement location, $x_n$ ($n$ = 1, 2, …, $N$), $M$ is the model order, $c_m$ is the $m$-th complex amplitude, $k_m$ is the m-th complex wave number, and $e$ is the estimation error. Here, the $m$-th complex wave number, $k_m$, has both a real part ($\beta_m$) that represents the propagation factor and an imaginary part ($\alpha_m$) that represents the spatial attenuation factor. Eq. (3.4) can be expressed in matrix form: i.e.,

$$\begin{bmatrix} f_1 \\ f_2 \\ \vdots \\ f_N \end{bmatrix} = \begin{bmatrix} r_1^0 & r_2^0 & \cdots & r_M^0 \\ r_1^1 & r_2^1 & \cdots & r_M^1 \\ \vdots & \vdots & \ddots & \vdots \\ r_1^N & r_2^N & \cdots & r_M^N \end{bmatrix} \begin{bmatrix} c_1 \\ c_2 \\ \vdots \\ c_M \end{bmatrix} - \begin{bmatrix} e_1 \\ e_2 \\ \vdots \\ e_N \end{bmatrix} \tag{3.5}$$

or, in more compact form,

$$\mathbf{f} = \mathbf{R}\mathbf{c} - \mathbf{e} \tag{3.6}$$

where $r_m = \exp(\mathrm{i}k_m\Delta x)$, $\Delta x$ is the sampling interval, and the last vector term is the estimation error. Note that $f_n = f(x_n)$ and $e_n = \mathrm{e}(x_n)$ in Eqs. (3.5) and (3.6). In the iterative procedure, the complex wave numbers and their complex amplitudes are found by an optimization scheme, essentially a steepest decent method, which has the effect of minimizing the error norm defined as

$$\mathrm{E} = \mathbf{e}^H \mathbf{e}. \tag{3.7}$$

Once $\mathbf{r} = [r_1\ r_2\ \ldots\ r_M]^{\mathrm{T}}$ is found separately from $\mathbf{c}$ by applying the numerical optimization scheme, the optimal value of $\mathbf{c}$ can be calculated analytically from Eqs. (3.6) and (3.7) provided that $\mathbf{r}$ is a constant vector. Thus, the unknowns $\mathbf{r}$ and $\mathbf{c}$ are separately updated under the assumption that one of them is constant in turn at each iteration step [48]: i.e., $\mathbf{r}$ is updated using the steepest decent method assuming $\mathbf{c}$ is constant; then $\mathbf{c}$ is calculated based on this new $\mathbf{r}$. These steps are repeated until a convergence criterion is satisfied.

### 3.4.3 Determination of Model Order and Starting Point

Consider first the conventional Prony method. The equation for the wave numbers can be separated from Eq. (3.6) (when there is no estimation error) by utilizing a characteristic equation defined as

$$r^M - a_{M-1} r^{M-1} - \cdots - a_1 r - a_0 = 0 \tag{3.8}$$

of which the roots are $r_m = \exp(\mathrm{i} k_m \Delta x)$ ($m$=1, 2, …, $M$) [44]. The coefficients of the characteristic equation, $a_m$, can be calculated from

$$\begin{bmatrix} f_M & \cdots & f_1 \\ \vdots & \ddots & \vdots \\ f_{N-2M-1} & \cdots & f_{N-M} \end{bmatrix} \begin{bmatrix} a_{M-1} \\ \vdots \\ a_0 \end{bmatrix} = \begin{bmatrix} f_{M+1} \\ \vdots \\ f_N \end{bmatrix}. \tag{3.9}$$

When the roots of Eq. (3.8) are known, the values of the wave amplitudes can be obtained from Eqs. (3.6) and (3.7) analytically, thus providing candidate starting values for the iterative procedure. It is first necessary, however, to estimate the model order, which in turn determines the number of starting values required. The model order can be determined by examining the singular values of the coefficient matrix in Eq. (3.9): the model order is then equal to or larger than the number of significant singular values (i.e., the rank of the coefficient matrix). The final parameter starting values are selected from amongst the solutions of the conventional method. When a dominant wave component is removed from the exponential series, the residual error should be large. Thus, the starting values are chosen to include only the wave components that make the error norm significantly large when one of them is removed from the Prony series.

## 3.5 Results and Discussion

### 3.5.1 Spatial Response

The normalized magnitude of the radial treadband velocity is plotted in Figs. 3.3 and 3.4 for two cases: (a) tire inflation 20 psi and (b) tire inflation 40 psi. These results can be used to explain the circumferential modal behavior and the spatial attenuation determined by the amount of the decrease of the amplitude envelope per unit circumferential length.

Consider first the spatial responses in Fig. 3.3. At 100 Hz, it is obvious that there is not much spatial attenuation although there is significant spatial attenuation at both 500 and 1000 Hz. It is also clear that circumferential standing wave modes are formed at 100 Hz: i.e., $n = 3$, since there are 6 nodes, for the 20 psi tire and $n = 2$ for the 40 psi tire. This indicates that the phase speed at 100 Hz in the 40 psi tire is faster than that in the 20 psi one. The last observations from Fig. 3.3 are that the spatial attenuation at the higher frequency is larger than that at lower frequency and that it is more significant in the tire with lower pressure at the same frequency.

Similar phenomena can be observed in Fig. 3.4 where the complete space-frequency data sets are shown. Note that the circumferentially modal nature of the tire response is evident below 700 Hz in the 20 psi case and below 800 Hz in the 40 psi case. At higher frequencies, the treadband vibration decays to negligible levels in less than one-half of the tread circumference. Thus at high frequencies, waves propagate freely away from the drive point, while at lower frequencies oppositely directed circumferentially propagating waves interfere with each other to create standing wave patterns around the tire circumference. Additionally, there are some frequencies, such as approximately 280 Hz, 420 Hz, and 550 Hz in Fig. 3.4(a) and 300 Hz, 500 Hz, and 700 Hz in Fig. 3.4(b), where the characteristics of the spatial response change rapidly: the waves near one of these frequencies are attenuated very quickly. This frequency is traditionally called the “cut-on” frequency: i.e., the frequency at which a specific wave mode starts to propagate along the tire.

### 3.5.2 Non-Parametric Dispersion Relations

Consider the wave number domain results: see Fig. 3.5. First, the wave number-frequency domain results are nearly symmetrical with respect to the zero wave number axis, indicating that waves propagate equally in the positive and negative circumferential directions. Second, each of the curving trajectories in the wave number-frequency domain indicates the existence of a single, circumferentially propagating wave type. Each of these waves is associated with a particular mode shape of the treadband cross-section, as illustrated schematically in Fig. 3.8, which will be explained in detail in the following section. Four propagating modes cut on below 700 Hz, and the cut-on frequencies increase with inflation pressure: see Fig. 3.5. This behavior is characteristic of wave guide-like flexural modes. Note that owing to the inflation-dependent cut-on

frequencies of these flexural modes, it is probable that stiffness in this case is largely provided by the treadband tension resulting from the inflation pressure, although some trajectory curvature attributable to the flexural stiffness of the treadband is visible at higher frequencies. Each trajectory approaches asymptotically a line of approximately constant slope in the wave number-frequency domain (indicated by the superimposed dotted black lines in Fig. 3.5): the slope of that line gives the group speed of the modes. At 20 psi, the group speed of the membrane modes is approximately 60 m/s, while at 40 psi, the group speed is approximately 80 m/s (an increase approximately proportional to the square root of the inflation pressure, as would be expected for membrane waves).

A faster wave cuts on in the vicinity of 600 Hz (indicated by the line at 120 m/s). The relatively high speed of this propagational mode appears to be related to an extension of the entire carcass: i.e., this mode cuts on at $n = 0$, thus causing the whole tire to expand and contract. Owing to its much higher group speed, and to the fact that this mode at cut on causes a net volume displacement of air, this mode is probably a relatively effective sound radiator that would be expected to dominate the radiated sound field at 600 Hz and above.

### 3.5.3 Cross-Sectional Mode Shapes

The results in Fig. 3.7 show the representative cross-sectional mode shapes associated with the first and second trajectories in the low frequency region in Fig. 3.5. Note that 154 Hz is a frequency at which the first trajectory that cuts on at approximately 50 Hz is dominant, and that the second trajectory cutting-on at approximately 250 Hz is predominant at 356 Hz in Fig. 3.5. The cross-sectional mode at 154 Hz has nodes at 10 cm and 30 cm; i.e., at the tire shoulder. Thus, this cross-sectional mode is $m = 3$, which indicates that the first trajectory in Fig. 5 is associated with the cross-sectional mode $m$=3. Similarly, it can be concluded that the second trajectory is associated with $m = 5$. These conclusions are illustrated in Fig. 3.8 where each line is associated with its cross-sectional mode number.

### 3.5.4 Parametric Dispersion Relations

When the wave number transform technique is applied to the measured data, only the real

part of the dispersion relation is obtained, as shown in Fig. 3.5. That information allows the wave speed to be inferred, but not the corresponding attenuation characteristics. Further, because of the exponentially decaying characteristic of each wave component, each of the latter has a finite bandwidth in the wave number domain at a specific frequency, thus sometimes making it difficult to identify peak locations in the frequency-wave number domain. The resolution in wave number is also limited by the total length of the measured data.

These various concerns have been resolved by fitting a Prony series to the spatial data as explained in Section 3.4. The results of the Prony series identification at three frequencies are shown together with the measured data in Fig. 3.9. It is apparent that the measured data is well represented by the Prony series. The real and imaginary wave numbers obtained from the Prony series identification at each frequency are plotted separately in Fig. 3.10. The brightness of the result at each frequency represents the magnitude of the complex amplitude associated with that frequency-wave number combination: thus the dominant mode at any frequency may be identified. The most interesting feature in Fig. 3.10 is the behavior near the cut-on frequency of the higher modes. For example, near the cut-on frequency of the second mode (approximately 300 Hz), the first mode begins to be significantly attenuated and the second mode "cuts on" when it has a large imaginary wave number: i.e., the second mode is initially nearly evanescent. As the frequency increases, the imaginary wave number of the first mode increases and that of the second mode decreases and the dominant mode shifts from the first to the second mode.

By fitting the dispersion curves of the first and second modes with polynomials, analytical expressions for the dispersion characteristics of these modes were obtained. By using these polynomial expressions, the wave speeds and spatial attenuations per wavelength then can be calculated: the former from the dispersion curves in the real wave number domain and the latter from those in the imaginary domain. Both results are shown in Fig. 3.11. As expected, the phase velocity of each mode approaches an asymptotic limit from above as the frequency increases, while the group speed increases towards the same limit from below. It can also be seen that the attenuation per wavelength approaches a maximum near the modal cut on frequency.

## 3.6 Conclusions

Here tire treadband vibration has been measured and studied by using wave number decomposition techniques at frequencies below 1000 Hz. It is has been shown from measured, non-parametric dispersion relations that, below 1000 Hz, the carcass vibration is controlled by no more than six propagating waves and that each of these waves is associated with a particular cross-sectional mode shape. These waves fall into two groups: flexural waves and extensional waves, the former propagating significantly more slowly than the latter. Thus, it can be concluded that tires can be effectively modeled as waveguides. It was also pointed out that the first effective sound radiation from the carcass probably occurs at around 600 Hz with the cut-on of the first extensional mode. Whereas the spatial Fourier transform yielded only real and banded wave number estimates with limited resolution, the Prony series procedure described here can be used to decompose the measured data into a small number of exponential terms (including an exponential decay factor). The Prony series results can then be used to estimate the velocity and spatial rate of attenuation of each mode that contributes significantly to the tire vibration.

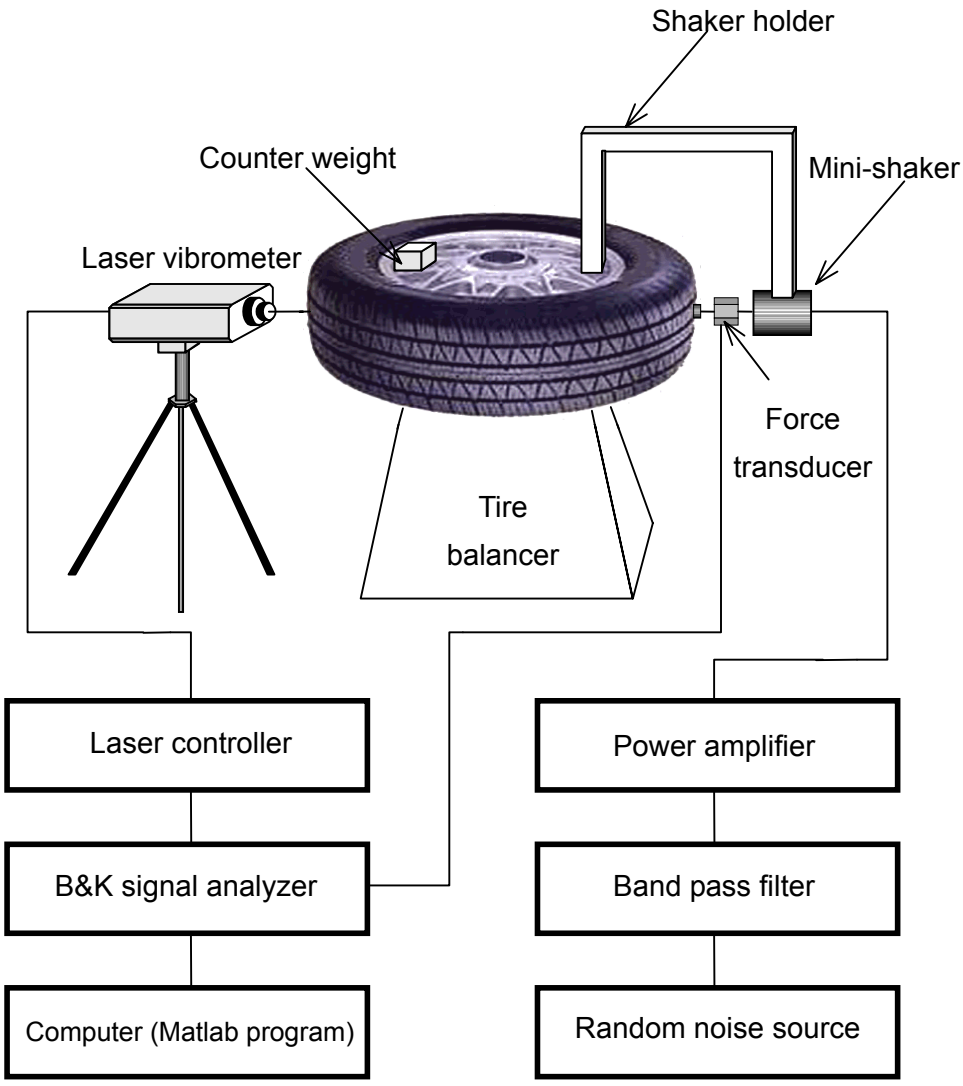


Figure 3.1: Sketch of experimental setup used for the measurement of stationary tire vibration.

Figure 3.2: Photograph showing retro-reflective tape applied to tire treadband.

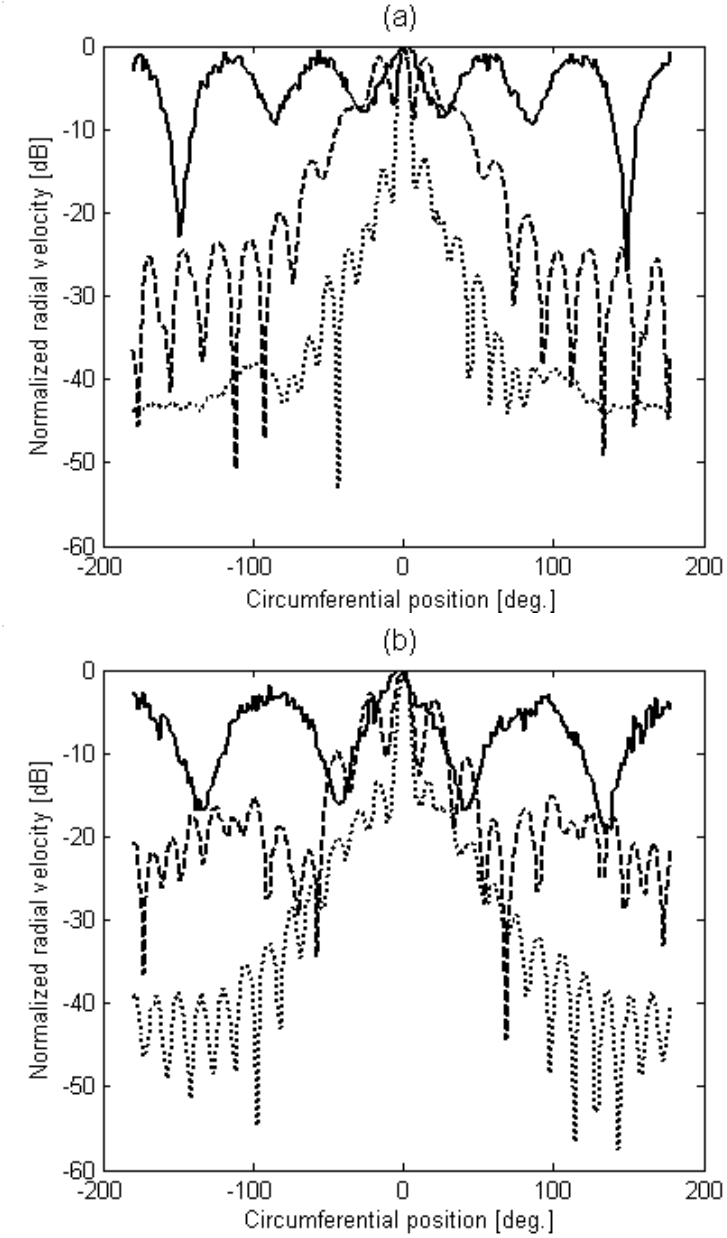


Figure 3.3: Magnitude of radial velocity (normalized with respect to drive-point velocity) versus circumferential position at three frequencies: ———, 100 Hz; – – – –, 500 Hz; ·····, 1000 Hz: (a) Inflation pressure 20 psi and (b) Inflation pressure 40 psi.

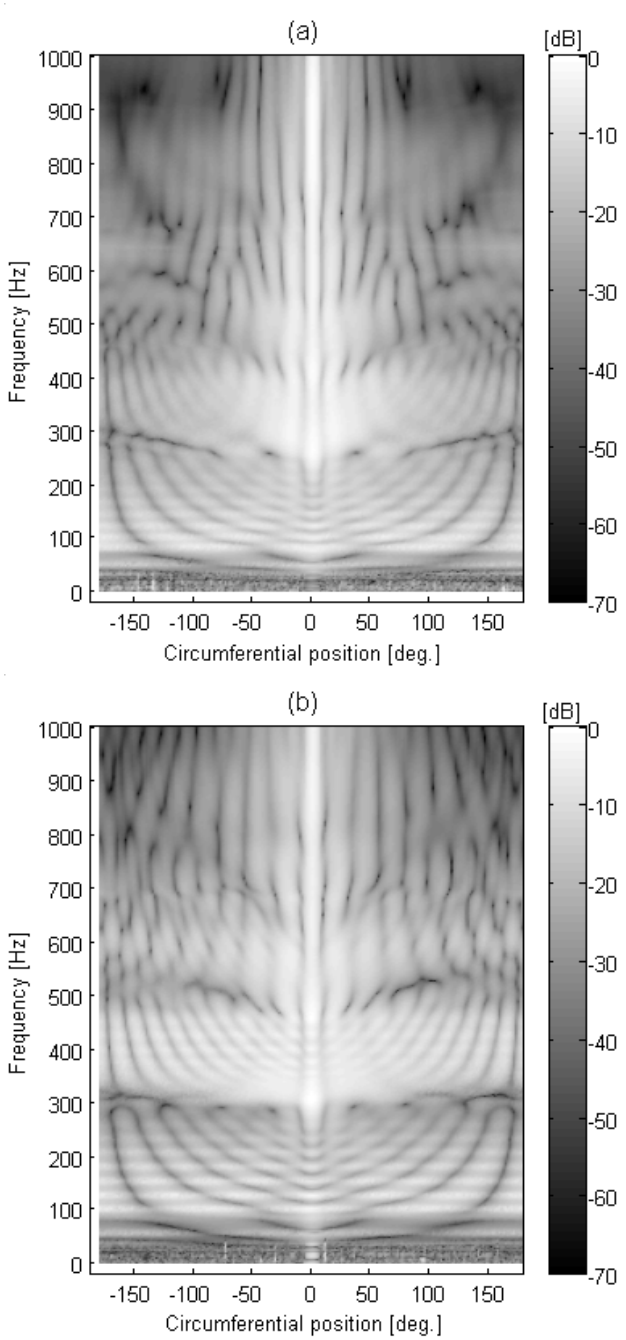


Figure 3.4: Magnitude of radial velocity (normalized with respect to the largest drive-point velocity within each data set) versus circumferential position and frequency: (a) Inflation pressure 20 psi and (b) Inflation pressure 40 psi.

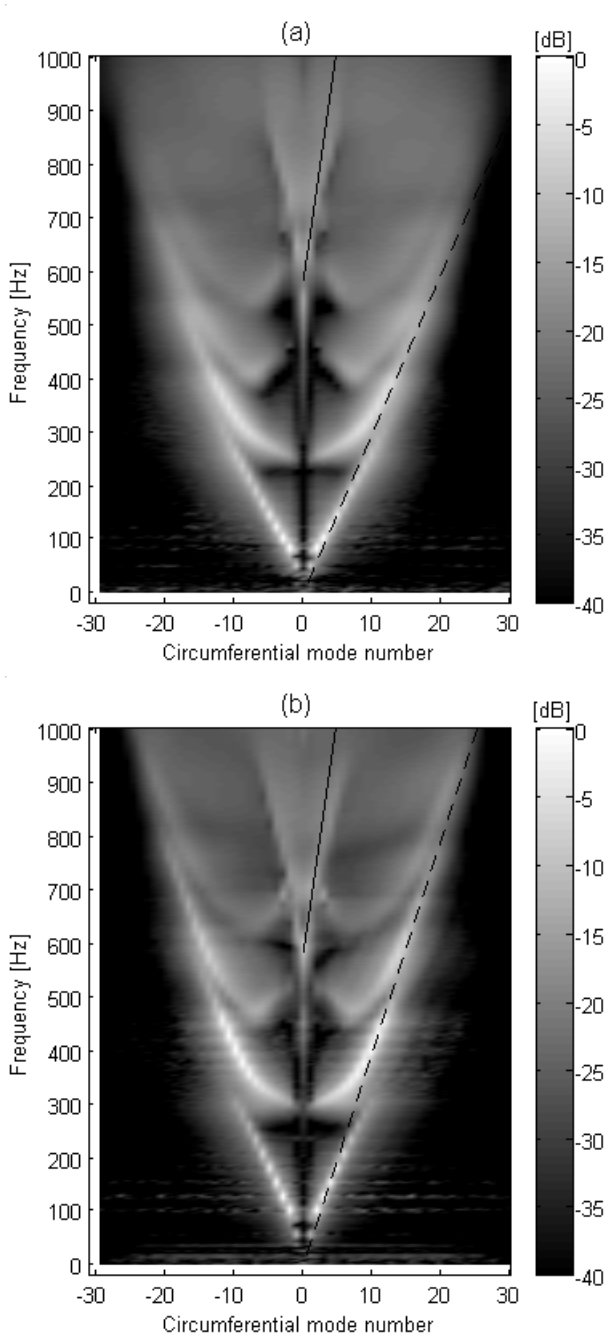


Figure 3.5: Magnitude of radial velocity (normalized with respect to largest value within each data set) versus frequency and circumferential mode number: (a) Inflation pressure 20 psi; – – – –, group speed 60 $ms^{-1}$; ———, group speed 120 $ms^{-1}$ and (b) Inflation pressure 40 psi; – – – –, group speed 80 $ms^{-1}$; ———, group speed 120 $ms^{-1}$.

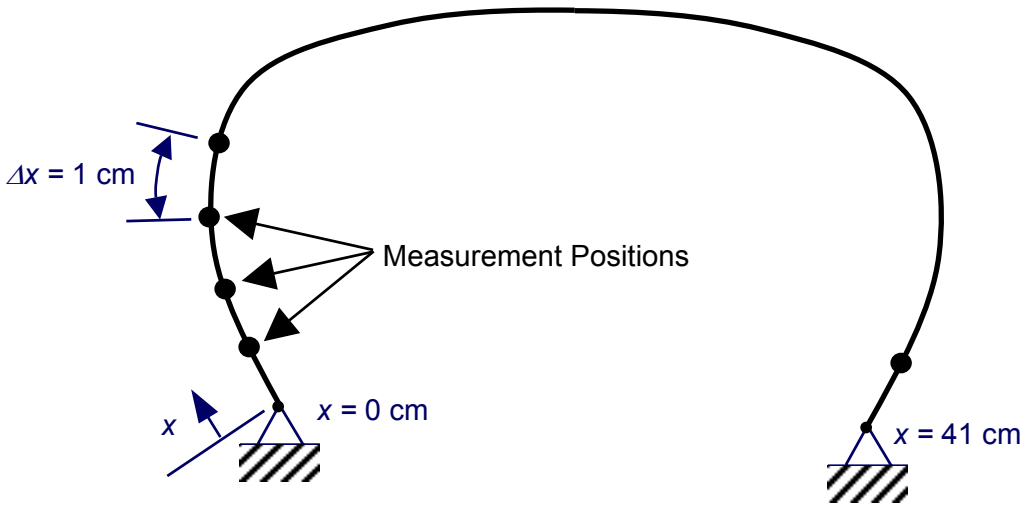


Figure 3.6: Sketch of cross-sectional measurement positions.

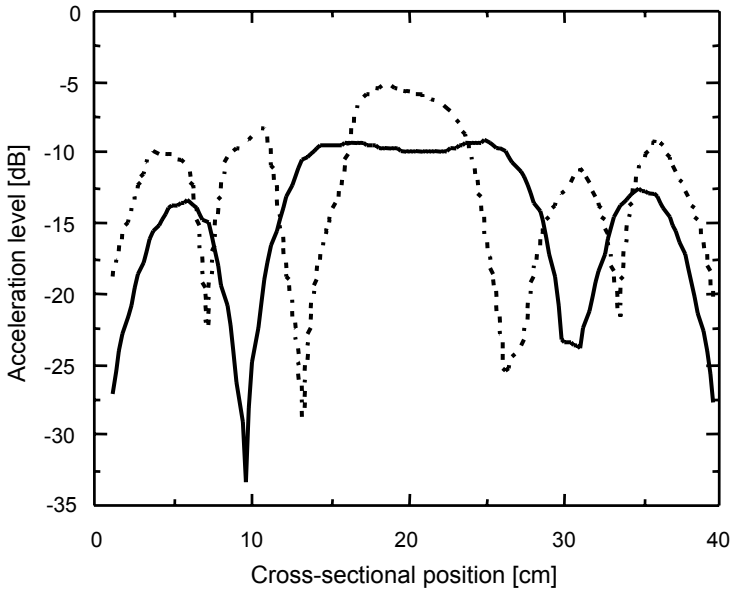


Figure 3.7: Acceleration level normal to surface (with respect to arbitrary reference) versus cross-sectional position, measured at a circumferential position 45 deg. from the drive-point: ———, 154 Hz; - - - - -, 356 Hz.

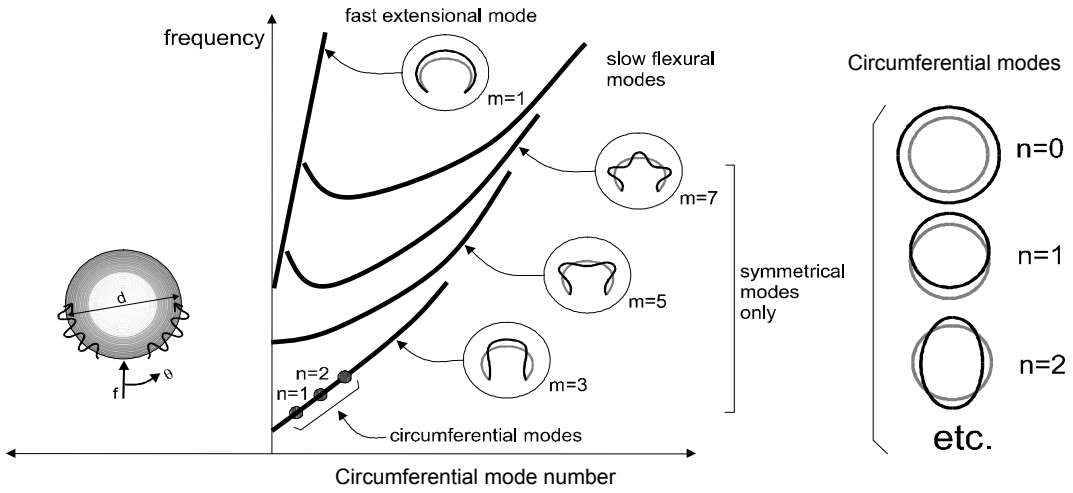


Figure 3.8: Summary of stationary tire dynamic response when point-driven at the center of treadband.

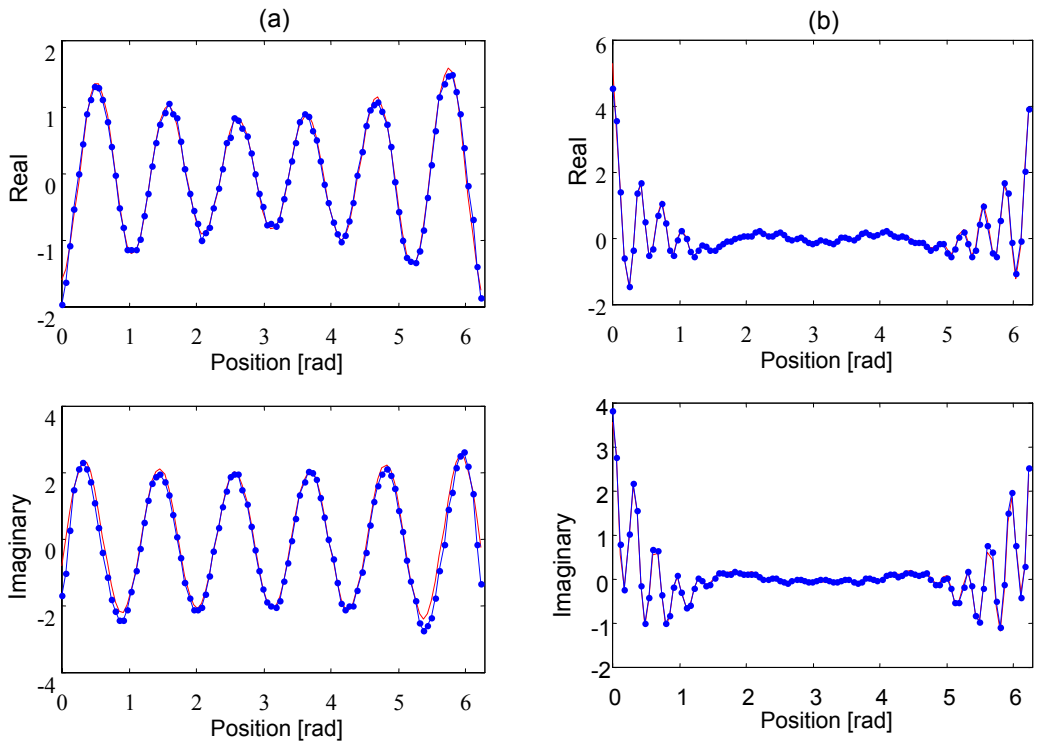


Figure 3.9: Results of Prony series identification applied to the experimental data at two frequencies: solid line with dots - measured data and solid line without dots - Prony results: (a) 200 Hz and (b) 800 Hz.

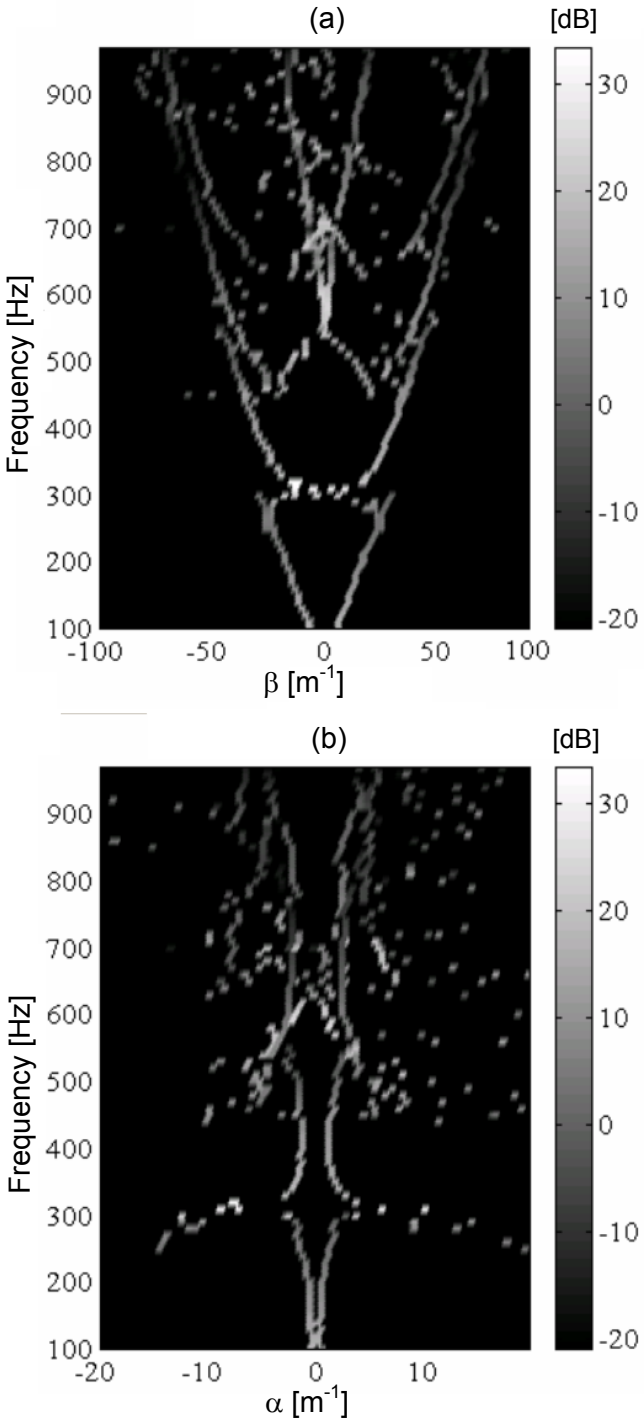


Figure 3.10: Parametric dispersion relations obtained by Prony series identification: (a) Real wave number and (b) Imaginary wave number.

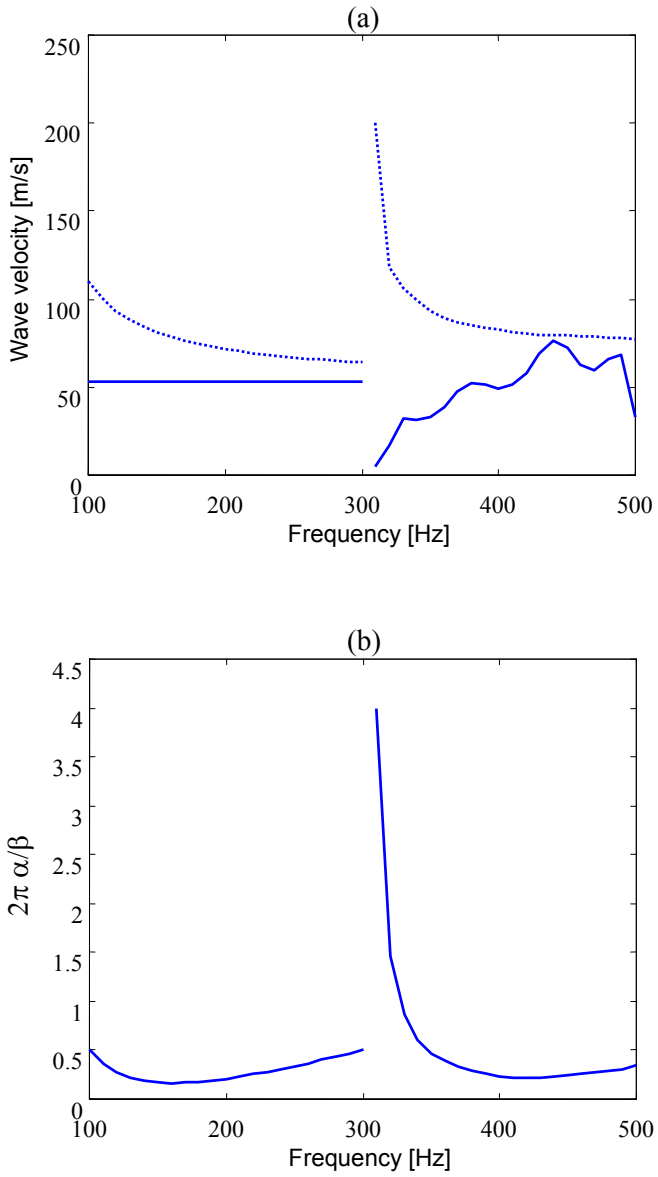


Figure 3.11: Results obtained from polynomial curve fittings of parametric dispersion relations: (a) Phase and group velocities (dotted line - phase velocity and solid line - group velocity) and (b) Spatial attenuation per wavelength.

# 4. MODELING OF TIRE VIBRATION

A stationary tire was driven radially at a point on its treadband and measurements of the resulting radial treadband vibration were made around the treadband circumference by using a laser Doppler velocimeter. By performing a circumferential wave number decomposition of the measured space-frequency data, the wave propagation characteristics were visualized. In an attempt to understand these experimental results in details, the tire treadband was modeled as a ring-like, circular cylindrical shell with air pressure acting on its interior surface. The model makes allowance for general boundary conditions at the lateral edges of the ring, and the sidewall of the tire is modeled as a distribution of springs and dampers. Both analytical and finite element methods were applied to obtain the vibration response. This shell model was found to explain the propagation characteristics of the waveguide modes that are visible in the experimental results. In particular, the low frequency, flexural wave characteristics associated with finite curvature and resulting in efficient radiation of sound were well reproduced. Fast in-plane waves that are potentially significant sound radiators at high frequencies were also well reproduced by this model: the excitation of these modes results from wave coupling within the curved shell. Finally, a full FE model in which the shape is the similar to a "real" tire was analyzed for the purpose of comparison with the simple circular cylindrical shell model. The latter model can be used to generate input data for sound radiation predictions.

## 4.1 Introduction

In Chap. 3, it was shown that wave number transform techniques can be used to characterize both tire dynamics and their potential for radiating sound. Here the objective was to describe simple analytical and numerical models of tire treadbands that

nonetheless reproduce the significant features of measured tire dispersion relations. Thus the present work represents a first attempt to relate tire design parameters to the major features of their associated dispersion relations. It is hoped that this approach will ultimately lead to the identification of tire designs that result in minimum sound radiation in particular frequency ranges of interest.

Previously Kropp [29] modeled a treadband as a 2-D circular ring; however, the higher wave modes, associated with displacement variations across the width of the treadband were not considered. Recently, Pinnington and Briscoe [51] introduced a flat, thick plate model that accounted for the cut-on of the higher cross-sectional modes as well as the effects of shear deformation and rotary inertia. However, this model was not able to account for curvature effects at low frequencies where the radius of curvature is comparable to the wavelength. Here the emphasis was placed on modeling the treadband as a circular cylindrical shell that has finite width and curvature. First, an analytical model is described in which the treadband is modeled as a simply supported, circular cylindrical shell. This model was used to identify the types of waves that can propagate in circular structures, to illustrate the effect of inflation pressure on wave speed, and to verify the performance of a finite element (FE) model. The latter model was in turn used to model the effect of finite sidewall stiffness and orthotropy resulting from fiber-reinforcement of the treadband. The inflation pressure acting on the inside surface of the treadband was also considered in both the analytical and FE models. It has been found that the FE model reproduces the major features of tire dispersion curves: e.g., the appearance of tensioned membrane-like flexural modes at low frequencies, and secondly the cut-on at the tire's circumferential ring frequency of a fast mode that is primarily associated with extensional motion of the treadband. Finally, a full model that has the same cross-sectional shape as a real slick tire was modeled with shell elements. Inflation pressure was also applied on the inside surface of the model.

## 4.2 Analytical Model of Tire Treadband

Here the treadband of a tire was modeled as a circular cylindrical shell as shown in Fig. 4.1. The effects of inflation pressure were allowed for by modeling the resultant in-plane residual stresses. When a real tire is inflated, it deforms from its original shape and the deformation results in a spatial variation of residual stresses within the tire. When forced externally, the tire then vibrates around the statically deformed shape.

Here it was assumed that the static deformation due to inflation pressure could be ignored: thus the residual stresses were assumed to be uniformly distributed within the treadband, and the tire was assumed to vibrate around its uninflated shape. Under these assumptions, the residual circumferential stress acting normal to the treadband cross-sectional area can be easily calculated on the basis of static force equilibrium. Although the residual stress in the *x*-direction is not directly related to the action of the inflation pressure in this rigid body model, the inflation pressure acting on a tire's sidewalls results in *x*-direction residual stresses that balance the force acting between the sidewall and rim.

The vibration of the treadband has been modeled by using Love's shell equations including the effects of in-plane residual stresses as given by Soedel [52]. When shear deformation, rotary inertia and non-linear effects are neglected, the governing equations become

$$-\frac{\partial N_{xx}}{\partial x}-\frac{1}{a}\frac{\partial N_{x\theta}}{\partial \theta}-\lambda \dot{u}_x-\rho h\ddot{u}_x=q_x \tag{4.1}$$

$$-\frac{\partial N_{x\theta}}{\partial x}-\frac{1}{a}\frac{\partial N_{\theta\theta}}{\partial \theta}-\frac{Q_{\theta r}}{a}+\lambda \dot{u}_\theta+\rho h\ddot{u}_\theta=q_\theta \tag{4.2}$$

$$-\frac{\partial Q_{xr}}{\partial x}-\frac{1}{a}\frac{\partial Q_{\theta r}}{\partial \theta}+\frac{N_{\theta\theta}}{a}-N_{xx}^{r}\frac{\partial^2 u_r}{\partial x^2}-\frac{N_{\theta\theta}^{r}}{a^2}\frac{\partial^2 u_r}{\partial \theta^2}+\lambda \dot{u}_r+\rho h\ddot{u}_r=q_r\,, \tag{4.3}$$

where $u$ is the displacement in the direction indicated by the subscript, $N_{ij}$ and $Q_{ij}$ ($i, j = x, \phi, r$) are resultant in-plane and shear forces (see Appendix B), respectively, the superscript $r$ denotes residual force, and $q$ is the external force applied in the direction indicated by the subscript. In addition, $\rho$ is the density of the treadband, $h$ is its thickness, $\lambda$ is the damping constant, and $a$ is the tire radius. When the static deformation due to inflation pressure is ignored, the residual circumferential force can be expressed as

$$N_{\theta\theta}^{r}=ap\,, \tag{4.4}$$

where $p$ is the inflation pressure. Simple support boundary conditions were invoked at both edges of the treadband. A set of assumed displacements that satisfy the simply supported boundary condition, that is the product of spatially sinusoidal functions in the $x$ and $\theta$ directions, is used to perform a modal analysis of this system [52]: i.e.,

$$u_x(x,\phi,t)=A_{mn}\cos\left(\frac{m\pi x}{L}\right)\cos\big(n(\theta-\theta_0)\big)\exp(i\omega_{mn}t) \tag{4.5}$$

$$u_{\phi}(x,\phi,t) = B_{mn}\sin\left(\frac{m\pi x}{L}\right)\sin\left(n(\theta-\theta_0)\right)\exp(i\omega_{mn}t) \tag{4.6}$$

$$u_{r}(x,\phi,t) = C_{mn}\sin\left(\frac{m\pi x}{L}\right)\cos\left(n(\theta-\theta_0)\right)\exp(i\omega_{mn}t)\,, \tag{4.7}$$

where $\omega_{mn}$ is the natural frequency of the $(m,n)$ mode and the constant phase angle, $\theta_0$, is 0 or $\pi/2$. The forced harmonic response was then represented by the linear superposition of modes, with the appropriate modal coefficients being determined by applying the point force. Damping was modeled by adding modal damping ratios, and they were assumed to be proportional to the natural frequencies of each mode.

The analytical solution served principally to verify the performance of the FE model described next, which was then used to represent more realistic configurations: e.g., resilient support at the treadband edges and orthotropic material properties.

## 4.3 Finite Element Model of Tire Treadband

The model described above was reproduced in FE form (implemented in ANSYS Version 5.6.). However, in this case the residual stress and the initial displacement were calculated by performing an initial static analysis. The FE mesh and location of the applied force are shown in Fig. 4.2. Note that the FE model represents a quarter of the complete circular cylindrical shell. Since the point force is applied at the centerline of treadband, symmetry conditions can be applied at the $z = 0$ and $y = 0$ planes to improve computational efficiency. Element type SHELL63 was used to represent the treadband.

After verifying the accuracy of the FE model by comparing its predictions with the analytical solution, the simple support boundary condition at the treadband edges was replaced by a distributed radial stiffness and damping. That is, the nodal points at the treadband edges were connected by springs and dampers to stationary ground points that can be imagined to be points on the wheel rim. The radial springs and dampers represent a simplified sidewall model.

Commercial tires usually feature reinforcing fibers supported within a rubber matrix within the treadband to increase the tire's strength. The fiber acts to increases the stiffness in the fiber direction without altering the stiffness in the transverse direction. Thus if the composite treadband is to be modeled as an equivalent bulk material, the latter should be assumed to be orthotropic. This orthotropic property was included in the present FE model: the fiber direction was assumed to be in the $\theta$-direction, and thus the

Young's modulus in the $\theta$-direction is larger than that in the $z$-direction.

## 4.4 Full Tire FE Model

For the purpose of obtaining the vibration response of the sidewall, a full tire FE model in which the cross-sectional shape and effective material properties are similar to those of a real, slick tire, is considered here. Fig. 4.3 shows the cross-sectional shape of a real tire. To model the geometry of the real tire, the position and thickness of the sampling points that are approximately located at the center of the cross-sectional area as shown in Fig. 4.3 were first measured. Then polynomial curve fitting was applied to these data: the order of the polynomial was 7 for the curve fitting to the sampled center positions, 0 for the thickness of the treadband, and 4 for the thickness of the sidewall. The results of the curve fitting along with the sampled center position and thickness are shown in Fig. 4.4. Note that the thickness of the treadband was assumed to be constant as shown in Fig. 4.4(b): the interface between the treadband and sidewall is approximately located at $\theta = 45°$. The resulting coefficients of the polynomials are shown in Table 4.1. Based on the polynomial curve fits, a full FE model was generated (see Fig 4.5.): the nodes of the FE model were placed on the curve fitted to the sampled center points and the thickness at each node was calculated from the curve fitting to the sampled thickness. Note that the full FE model represents a quarter of the complete tire as in the case of the circular cylindrical shell model. The material parameters used for the circular cylindrical shell model (see Table 4.2) were also used for the treadband of the full FE model. In addition, the material properties of the sidewall are shown in Table 4.3. Note that the $x$-direction is the transverse direction that is orthogonal to the circumferential direction (or $\theta$-direction) and that is tangential to the tire surface.

## 4.5 Results and Discussion

The material parameters used for the calculations of both analytical and FE circular cylindrical shell model are listed in Table 4.2. These properties were adapted from the work of Kropp [29] and Pinnington and Briscoe [51] or were estimated based on physical reasoning or direct measurement.

The analytical dispersion relations obtained from Eqs. (4.1) to (4.3) in the absence

of external forcing and damping are plotted in Fig. 4.6. Note that there exist three natural frequencies for each circumferential mode shape: the three modes are associated with the primarily flexural, shear, and longitudinal motion in order of increasing frequency. The cross-sectional mode associated with each trajectory is denoted by $m$ = 1, etc. in Fig. 4.6(a). Lines corresponding to the asymptotic transverse shear and quasi-longitudinal wave phase speeds calculated for an equivalent plate are shown in Figure 4.6(b) where it can be seen that the modal trajectories associated with each of the latter two waves approach the corresponding asymptote at frequencies sufficiently high that the radius of curvature of the shell is very large compared to a wavelength. By comparing Figs. 4.6(a) and 4.6(b), it can be observed that inflation pressure and sidewall tension primarily affect the propagation of the flexural waves: the former has the effect of increasing the wave speed (i.e., increasing the slope of the model trajectories) while the latter increases the modal cut-on frequencies. These observations are consistent with the results of earlier experiments (see Chap. 3.).

The forced solutions for the simply supported edge case that were calculated by using the analytical and FE models are plotted in Fig. 4.7. The two results are identical except for minor differences resulting from differences in the damping models in the two cases. Hence, it was confirmed that in the case of the analytical model the residual stresses can be calculated by applying static force equilibrium and that the effects of initial static deformation shape can be ignored. The results of Fig. 4.7 also confirmed that the FE model functioned properly. By comparison with the analytical dispersion relations shown in Fig. 4.6(b), it can be seen that only odd cross-sectional modes are excited in this case since the radial point force was applied at the center of treadband. Further, it can be seen that neither the shear nor longitudinal waves are significantly excited in the simply supported edge configuration.

Figure 4.8 shows the forced FE response when the springs and dampers were applied to the edges of the treadband. To calculate the results shown in Fig. 4.8(a), isotropic material properties were assumed while the orthotropic results are shown in Fig. 4.8(b). The dispersion curves for the equivalent tensioned membrane and for the asymptotic quasi-longitudinal wave are also shown in these figures. It can be seen that at low frequencies the treadband behaves like a tensioned membrane (i.e., the first flexural root is approximately non-dispersive at low frequencies.). At higher frequencies, the root shows the curvature characteristic of flexural waves propagating in a stiff plate. Thus at low frequencies flexural wave propagation is largely controlled by inflation pressure, while at higher frequencies the flexural stiffness of the treadband

becomes more significant. Note that the second flexural mode which cuts-on near 500 Hz shows a negative group speed (i.e., a negative slope) in the orthotropic case: this feature has also been observed in earlier experiments. By comparison with the simply supported case, the cut-on frequencies are reduced since the resilient boundary conditions reduce the effective stiffness in the radial direction. Note, however that the cut-on frequencies of the higher order flexural modes are higher here than those observed in real tires, since in the latter case the cut-on frequency is controlled by the rim-to-rim distance, while in the present case the cut-on frequencies are determined primarily by the treadband width.

It can also be seen in Fig. 4.8 that the fast wave cutting-on near 400 Hz is asymptotically similar to a quasi-longitudinal wave. In the isotropic case, the ring frequency in the circumferential direction is $f_r$ = 356 Hz, while in the orthotropic case, $f_r$ = 411 Hz. As indicated in Table 4.2, the Young's modulus is larger in the $x$-direction in the latter case than in the isotropic case. This difference results in the increased wave speed in the $\theta$-direction in the orthotropic case (resulting in the increased slope of the various roots.). Note that the fast longitudinal mode can potentially radiate sound efficiently owing to its relatively high phase speed and because it is associated with a significantly large zero wave number component (i.e., the breathing mode of the tire) whereas the zero wave number components of the flexural modes are suppressed in the spring supported case (as observed in Chap. 3). Longitudinal modes of the type discussed here cannot be excited when a normal force is applied to a plate since all the wave types are uncoupled in that case. However, it is relatively easy to excite the longitudinal wave in a circular cylindrical shell since radial motion and in-plane motion in the $\theta$-direction are coupled to each other by the effects of finite curvature.

Figure 4.9 shows the dispersion relations obtained from the FE forced response of the full model. The major characteristics of the circular cylindrical shell model shown in Fig. 4.8(b) can be also observed in Fig. 4.9 although cut-on frequencies and asymptotic wave speeds are not exactly identical: tensioned membrane behavior at low frequencies, negative group speed of the second flexural wave, and longitudinal wave cutting-on can be seen in Fig. 4.9. Note that the total mass of the full FE model is heavier than that of the circular cylindrical shell model because the full FE model has additional sidewall mass. Thus, due to mass effects the asymptotic wave speeds in the results of the full model (Fig. 4.9(a)) are slower than those in the results of the circular cylindrical model (Fig. 4.8(b)), and the cut-on frequencies in Fig. 4.9(a) are lower than those in Fig. 4.8(b). For the purpose of verifying the mass effects in the full model, the density of the

treadband and sidewall were reduced by 400 kg/m$^3$ and 300 kg/m$^3$, respectively, and the results are shown in Fig. 4.9(b). By comparison of Figs. 4.9(a) and 4.9(b), it can be seen that the total mass controls the asymptotic wave speed and cut-on frequency.

## 4.6 Conclusion

It has been shown here that circular cylindrical shell models successfully reproduce the major features of tire dispersion relations. It was shown, for example, that increasing the inflation pressure increases the speeds and cut-on frequencies of flexural wave modes. Furthermore, when a distributed radial stiffness is applied to the treadband edges (to model the tire's sidewall), the shell model predicts the existence of the two wave types that are known to contribute significantly to tire dynamic response: flexural wave modes and a fast extensional wave mode that cuts-on at the circumferential ring frequency. The latter wave type, in particular, has the potential to radiate sound effectively owing to its relatively high phase speed. It was also observed that fiber reinforcement of the treadband, and the resulting orthotropic stiffness properties of the treadband, can account for the existence of modes having negative group speeds at small wave numbers. Finally, it has been shown that the full tire model also reproduces the major characteristics of measured tire dispersion relations. Because the full model has a sidewall, its vibration response can potentially be used as the input of a BEM sound radiation prediction.

Table 4.1: Coefficients of polynomial curve fittings used for full tire FE model.

| | Center position | Thickness |
|---|---|---|
| $\theta^7$ | -0.00149850814719 | NA |
| $\theta^6$ | -0.04025769477963 | NA |
| $\theta^5$ | +0.17418736177842 | NA |
| $\theta^4$ | -0.16478582814991 | -0.08774538233321 |
| $\theta^3$ | -0.11313933180690 | +0.16979310241424 |
| $\theta^2$ | +0.16604421979686 | -0.08284637359125 |
| $\theta^1$ | +0.02962997925038 | -0.00207482792958 |
| $\theta^0$ | +0.08701014435462 | +0.01096996817256 |

Table 4.2: List of parameters used for stationary tire treadband models.

| | |
|---|---|
| Young's Modulus (Isotropic Material) | $E = 4.9\times10^8$ N/m$^2$ |
| Young's Moduli (Orthotropic Material) | $E_x = 3.2\times10^8$ N/m$^2$, $E_\theta = 7.5\times10^8$ N/m$^2$ |
| Shear Modulus | $G_{x\theta} = 5.0\times10^7$ N/m$^2$ |
| Density | $\rho_t = 1200$ kg/m$^3$ |
| Poisson's Ratio | $\nu_{x\theta} = 0.45$ |
| Modal Damping Ratio | $\xi = 0.05$ |
| Thickness | $h = 0.008$ m |
| Radius | $a = 0.32$ m |
| Width | $L = 0.16$ m |
| Inflation Pressure | $p = 206910$ Pa ($p = 30$ psi) |
| Sidewall Tension | $N^r_{xx} = 2\times10^4$ N/m |
| Spring Constant of Sidewall | $k_{sidewall} = 197.95$ N/m$^2$ |
| Damping Constant of Sidewall | $c_{sidewall} = 1.00$ Ns/m$^2$ |

Table 4.3: Material properties of the sidewall used for the full FE model.

| | |
|---|---|
| Young's Moduli (Orthotropic Material) | $E_x = 3.2\times10^8$ N/m$^2$, $E_\theta = 7.5\times10^8$ N/m$^2$ |
| Shear Modulus | $G_{x\theta} = 1.5\times10^6$ N/m$^2$ |
| Density | $\rho_s = 800$ kg/m$^3$ |
| Poisson's Ratio | $\nu_{x\theta} = 0.45$ |

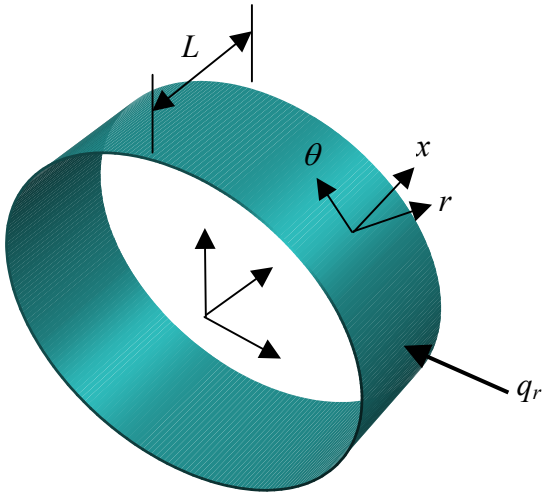


Figure 4.1: Treadband modeled as circular cylindrical shell with simply supported boundary conditions at the treadband edges.

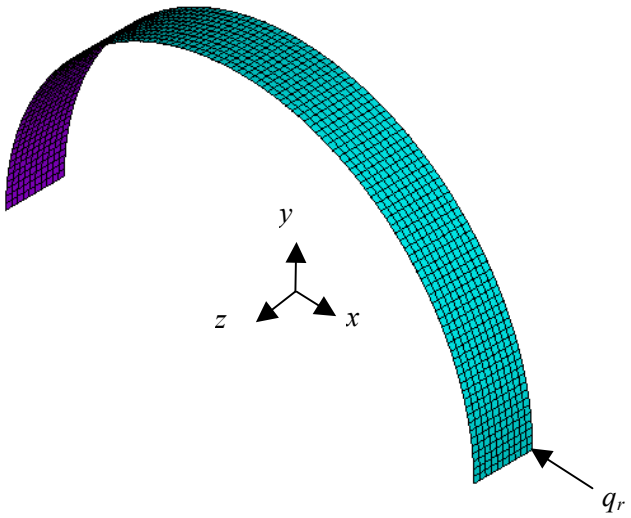


Figure 4.2: Finite Element model of circular cylindrical shell.

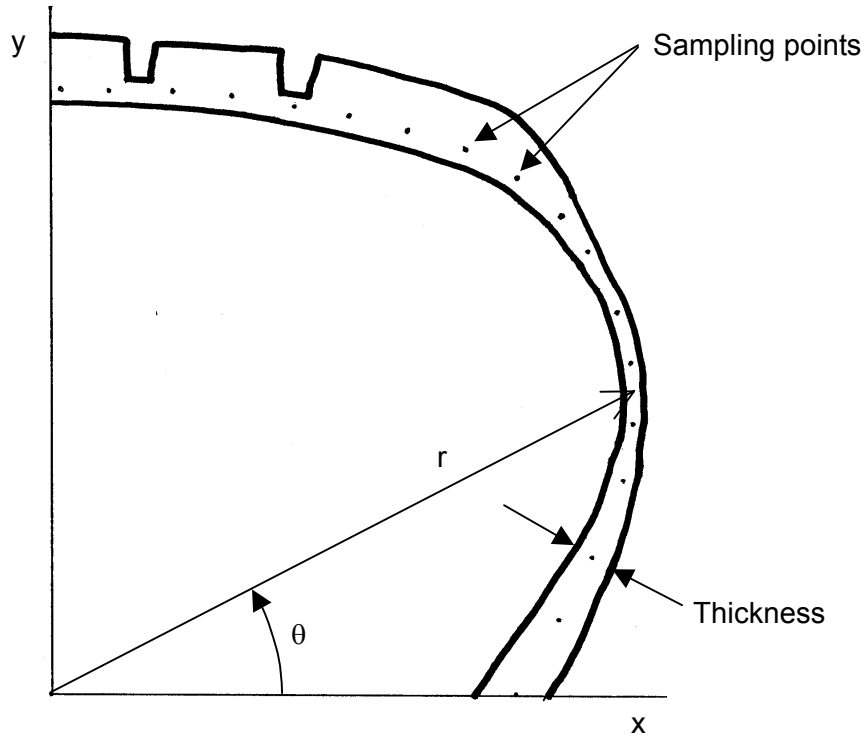


Figure 4.3: Cross-sectional shape of real tire: sampled points are located approximately at the center of the cross-sectional area.

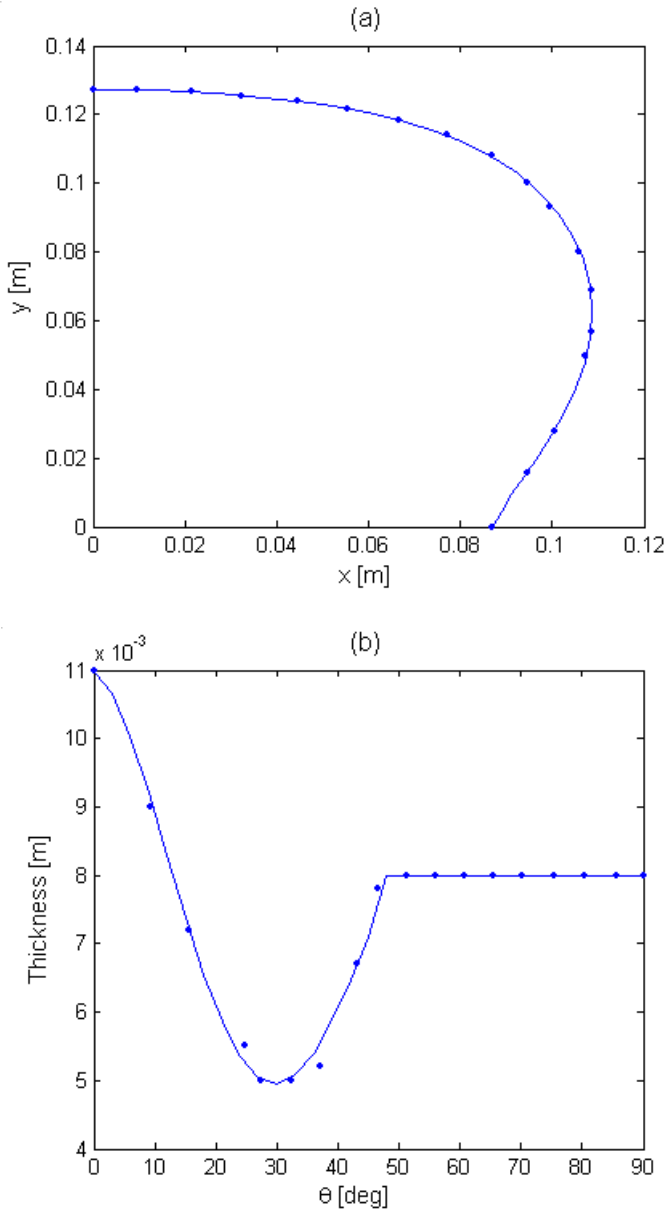


Figure 4.4: Polynomial curve fittings of sampled center position and thickness: dots - sampled data and sold line - polynomial curve fits: (a) Center position and (b) Thickness.

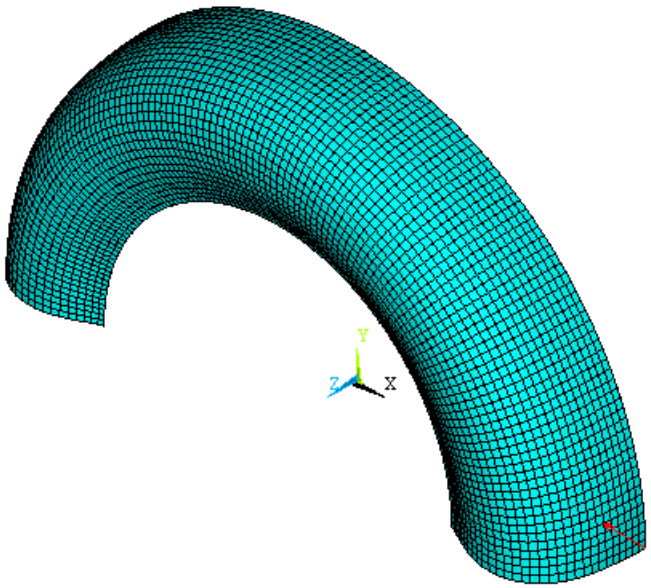


Figure 4.5: Mesh of full FE model and applied point force.

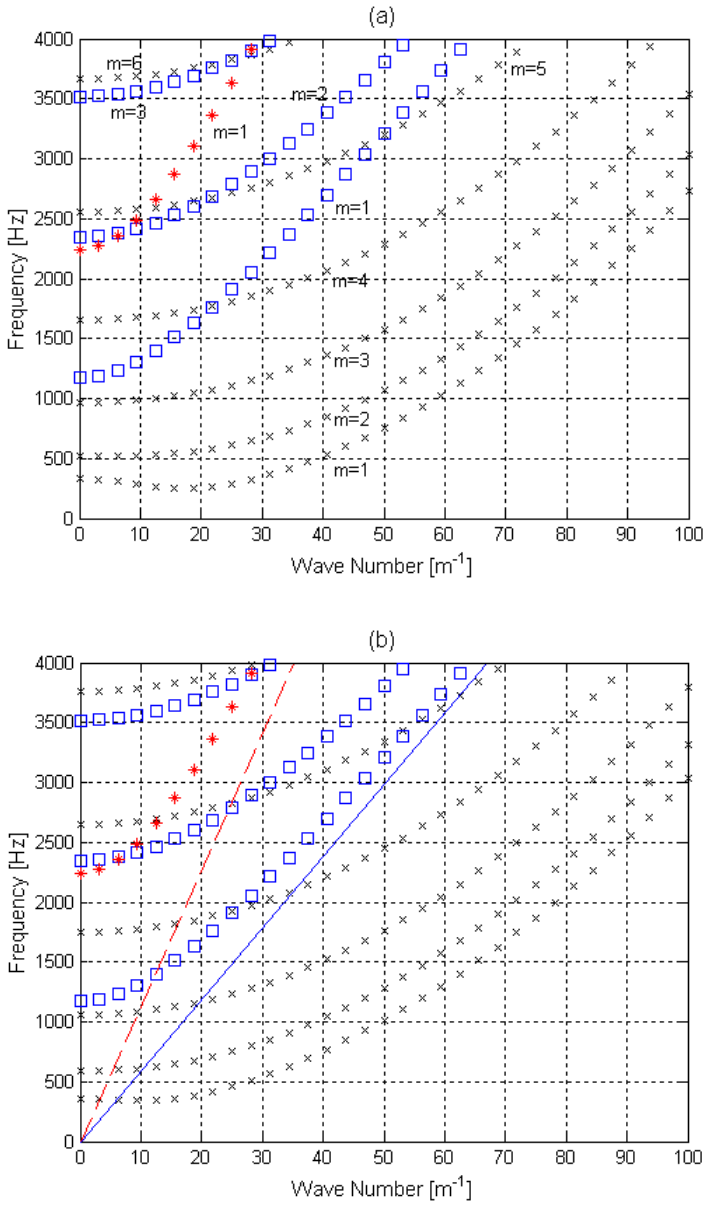


Figure 4.6: Analytical dispersion relations for a simply supported circular cylindrical shell: × - flexural wave, □ - shear wave, and * - longitudinal wave: (a) $p$ = 0 Pa and $N^{r}_{xx}$ = 0 N/m and (b) $p$ = 206910 Pa and $N^{r}_{xx}$ = 20000 N/m, dashed line - asymptotic quasi-longitudinal wave, and solid line - asymptotic transverse shear wave.

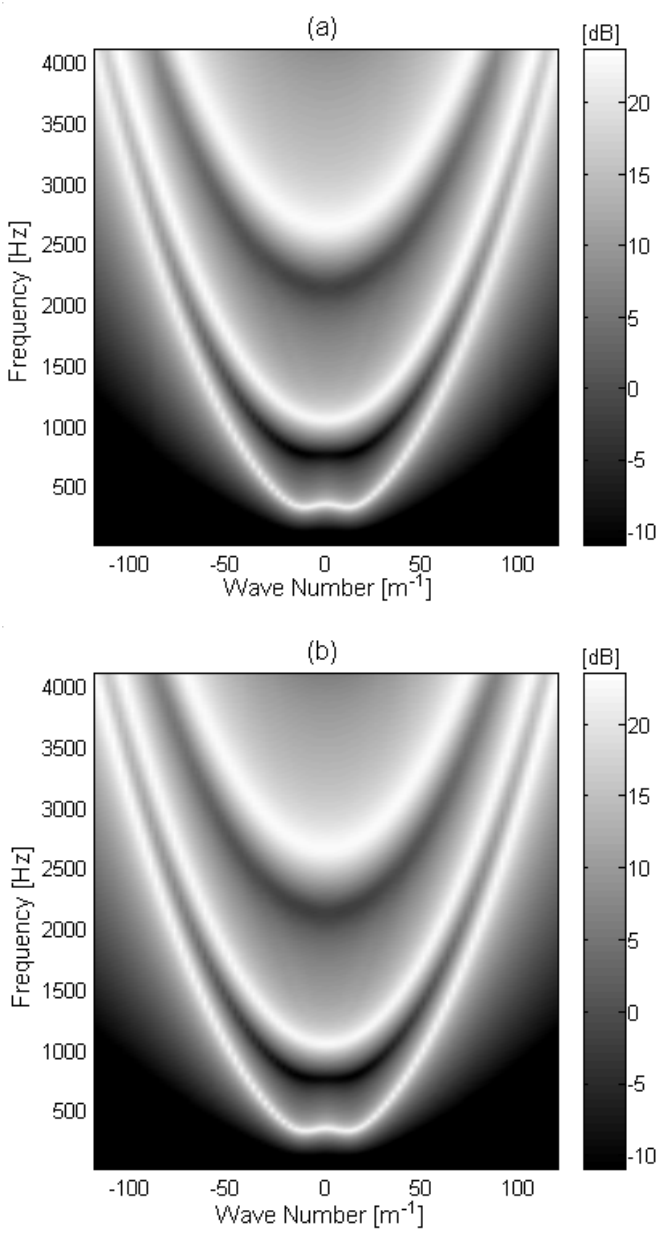


Figure 4.7: Forced responses for the simply supported circular cylindrical shell with $p$ = 206910 Pa and $N'_{xx}$ = 20000 N/m: (a) Analytical result and (b) Finite element simulation.

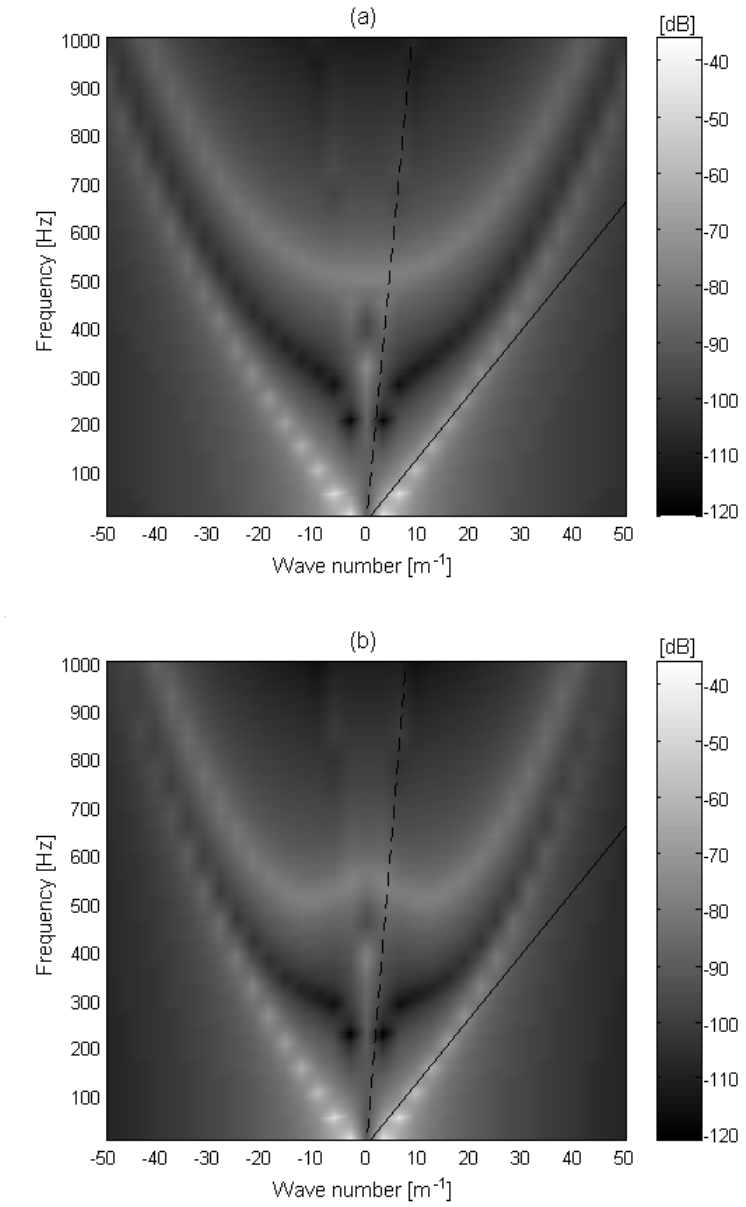


Figure 4.8: Dispersion relations for circular cylindrical shell supported by springs and dampers along the edges of treadband, dashed line - asymptotic longitudinal wave, and solid line - dispersion curve of equivalent tensioned membrane: (a) Isotropic material and (b) Orthotropic material.

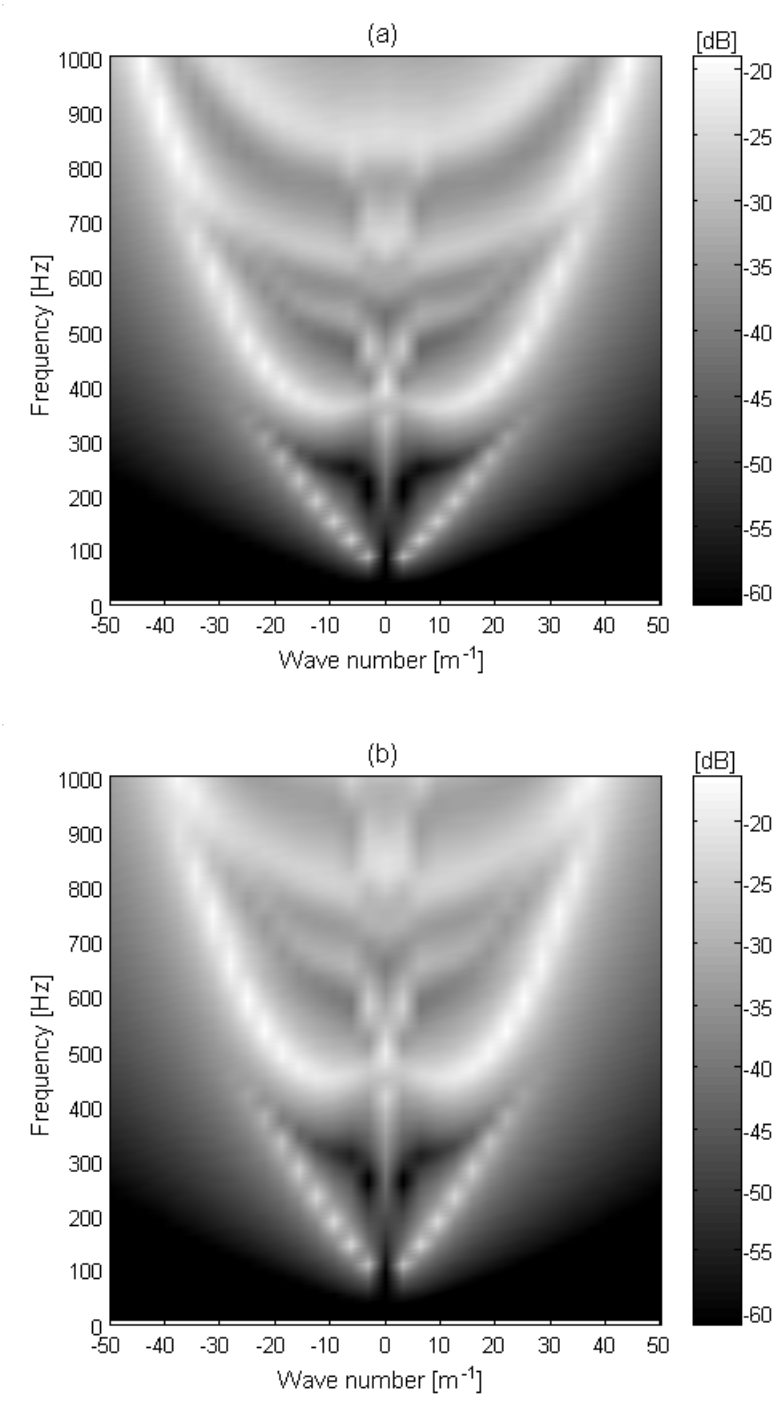


Figure 4.9: Dispersion relations for full FE model: (a) $\rho_t$ (density of treadband) = 1200 kg/m$^3$ and $\rho_s$ (density of sidewall) = 800 kg/m$^3$, and (b) $\rho_t$ = 800 kg/m$^3$ and $\rho_s$ = 500 kg/m$^3$.

# 5. HYBRID TWO-DIMENSIONAL FINITE ELEMENT METHOD

It has been shown experimentally that the vibration of a tire in the region near the contact patch can be represented by a set of decaying waves, each associated with a particular cross-sectional mode. Thus, a tire can be modeled as a lossy waveguide in which decaying waves propagate in the circumferential direction. It may therefore be computationally efficient to analyze tire vibration, especially in the region close to the contact patch, by using a hybrid finite element model in which the cross-section of a tire is approximated by two-dimensional finite elements while a wave-like solution is assumed in the circumferential direction. Here, a hybrid finite element was formulated based on composite shell theory: in particular, a circular conical shell element was formulated. The inflation pressure acting on the inner surface was included in the model by considering both residual stresses and non-linear terms in the strain-displacement relations. The dispersion relations for the tire model obtained by using the hybrid FE model were compared with those obtained from a three-dimensional FE model. It has been shown that the FE analysis made using the hybrid two-dimensional finite elements yields results in close agreement with a three-dimensional model.

## 5.1 Introduction

In Chapter 3, it was shown that the wave propagation characteristics of a tire could be visualized by performing a circumferential wave number transform of the measured space-frequency data. In an attempt to understand these experimental results in detail, the tire treadband was modeled as a circular cylindrical shell with air pressure acting on its interior surface (see Chap. 4). The shell model was found to be capable of representing the principal wave propagation characteristics of a tire: i.e., the vibrational response of a tire can be expressed as a superposition of decaying waves, each associated

with a particular cross-sectional mode shape. Thus, it was concluded that a tire can be modeled as a lossy waveguide.

When a FE model of a tire is used to analyze tire vibration at high frequencies, the size of the elements must be small and the tire's cross-section should be modeled in detail since the vibrational wavelengths may be comparable to the thickness of the tire. In consequence, a 3-D finite element model for high frequency analysis may require both a large modeling effort and significant computational resources.

Since tires behave like constant cross-section waveguides, it would be computationally efficient to analyze tire vibration by using hybrid, 2-D FE models: i.e., the cross-section of a tire is approximated by finite elements while a wave-like solution is assumed in the circumferential direction. Note that the hybrid, 2-D FE models of the type to be described here can also be used to investigate the dynamic behavior of any structure whose cross-sectional shape and material properties can be assumed to be constant with respect to the circumferential direction (e.g., tire, disc, or bell) or the axial direction (e.g., plate, straight ventilation duct, or aircraft fuselage).

Previously, Cheung described a hybrid, 2-D FE formulation based on the use of strip elements: interpolation functions were prescribed in the cross-sectional direction along with analytical mode shapes in the axial direction [63]. Richards analyzed the vibrational response of a tire coupled with an internal acoustical cavity by applying hybrid 2-D finite elements to both the tire and acoustical cavity [64]. In his case, the tire was modeled as a membrane: i.e., treadband flexural stiffness was not accounted for. In addition, Brockman et al. [65] estimated tire critical speeds by using a hybrid 2-D FE model. They used solid elements in cylindrical coordinates and accounted for the tire's rotation in the circumferential direction; inflation pressure was also considered by including initial stresses and non-linear stains in their formulation. Nilsson and Finnveden [66] calculated the input point mobility of a tire by using a hybrid 2-D FE model based on orthotropic, pre-stressed conical shell elements.

Here, a hybrid 2-D finite element for a circular, conical shell is described. The radius of curvature in the cross-sectional direction within an element was assumed to be infinite. However, in the circumferential direction the radius of curvature was considered to be finite. When the initial static stresses in a shell element are assumed to be much larger than the dynamic stresses associated with vibration, the non-linear strain energy terms represented by the multiplication of initial stresses and non-linear strains cannot be neglected [65,52]. Thus, the hybrid, 2-D finite shell element presented here includes non-linear strains to accommodate the latter situation. In addition, multi-

layered, thin shell elements (referred to as composite shell elements) with constant thickness in the cross-sectional direction were also incorporated. A linear thickness variation in the cross-sectional direction has also been implemented for a single layered shell element. Finally, allowance was made for both external point forces applied at a node and distributed forces exerted on an element.

As a first step in the application of the hybrid 2-D finite element, a tire was modeled by using orthotropic, circular conical shell finite elements. Natural frequencies and the associated mode shapes were calculated for both uninflated and inflated cases. Forced responses were then obtained by combining the modes extracted from the natural vibration analysis. Modal damping was included in the latter procedure. A 3-D FE model that had the same geometry and material properties as the hybrid 2-D model was also analyzed for the purpose of comparison.

## 5.2 Finite Element Formulation

### 5.2.1 Strain-Displacement Relations

Figure 5.1 shows a sketch of a circular conical shell finite element that has two nodal lines. Here we define the local element coordinates, $x_1$, as the cross-sectional direction, $x_2$, as the circumferential direction, and $x_3$, as the normal direction to the shell surface. Since the radius of curvature in the $x_1$-direction is assumed to be infinite, i.e., $R_1 = \infty$, the Lamé parameter in the $x_1$-direction is $A_1 = 1$ [52]. The radius of curvature and Lamé parameter in the $x_2$-direction, as illustrated in Fig. 5.1, are

$$R_2 = \frac{a}{\cos\theta} + x_1 \tan\phi \tag{5.1}$$

and

$$A_2 = a + x_1 \sin\phi\,, \tag{5.2}$$

respectively. Note that when the radius of curvature in the $x_2$-direction is infinite, i.e., $R_2 = \infty$ and $A_2 = 1$, a strip element is obtained.

It is assumed that vibrational displacements of the shell element can be approximated by interpolation functions in the $x_1$-direction and represented by an analytical solution in the $x_2$-direction. Then, the displacement vector $\mathbf{u} = [u_1\ u_2\ u_3]^T$ of

the element can be expressed as

$$\mathbf{u}(x_1, x_2, t) = \boldsymbol{\chi}(x_1)\mathbf{y}(t, x_2), \tag{5.3}$$

where $\boldsymbol{\chi}$ is the matrix of interpolation functions (see Appendix D), $\mathbf{y}$ is the nodal displacement vector, and $t$ is the time. The nodal displacement vector is defined as $\mathbf{y} = [u_{11}\ u_{12}\ u_{21}\ u_{22}\ u_{31}\ \beta_{11}\ u_{32}\ \beta_{12}]^{\mathrm{T}}$, where $u_{nm}$ is the translational displacement in the $x_n$-direction at the $m$-th node and $\beta_{nm}$ is the rotational displacement in the $x_n$-direction at the $m$-th node. Note that an element has two nodes and that each node has four nodal displacements (three translational displacements and one rotational displacement) that are functions of $t$ and $x_2$.

When the shear deformation of the shell is assumed to be negligible, strain can be separated into membrane and bending strains, and those strains can be directly related to displacements (see Appendix A). By substituting Eq. (5.3) into the strain-displacement relations, strains can be associated with the nodal displacement vector: i.e.,

$$\mathbf{e} = \mathbf{E}_0\mathbf{y} + \mathbf{E}_1\frac{\partial \mathbf{y}}{\partial x_2} + \mathbf{E}_2\frac{\partial^2 \mathbf{y}}{\partial x_2^2} + \cdots, \tag{5.4}$$

where $\mathbf{e}$ is the strain vector, $\mathbf{e} = [\varepsilon^0_{11}\ \varepsilon^0_{22}\ \varepsilon^0_{12}\ \kappa_{11}\ \kappa_{22}\ \kappa_{12}]^{\mathrm{T}}$, $\varepsilon^0_{mn}$ is the membrane strain, and $\kappa_{mn}$ is the bending strain. Note that the strain vector is separated in terms of independent variables: i.e., the matrices, $\mathbf{E}_0$, $\mathbf{E}_1$, $\mathbf{E}_2$, which are functions of $x_1$, and the derivatives of the nodal displacements which are functions of $x_2$ and $t$. Note also that the strain vector can be separated into two parts, i.e., $\mathbf{e} = \mathbf{e}_l + \mathbf{e}_n$, where the first part represents the linear strain vector and the second the non-linear strain vector: the first three terms on the right-hand side of Eq. (5.4) represent the linear strain-displacement relations.

### 5.2.2 Energy Expressions

In a composite shell, the resultant forces obtained by integrating the stresses in the thickness direction (i.e., the $x_3$-direction) can be related to the strains by

$$\mathbf{R} = \mathbf{C}\mathbf{e}, \tag{5.5}$$

where $\mathbf{R} = [N_{11}\ N_{22}\ N_{12}\ M_{11}\ M_{22}\ M_{12}]^{\mathrm{T}}$: i.e., the resultant force vector whose elements are expressed as

$$N_{mn} = \int_{-h/2}^{h/2} \sigma_{mn}\, dx_3\ ,$$

and

$$M_{mn} = \int_{-h/2}^{h/2} x_3 \sigma_{mn} dx_3 \ ,$$

where $\sigma_{mn}$ is the stress in the $x_n$-direction acting on the $x_m$-surface and $h$ is the thickness of the shell. When there are initial stresses, the resultant forces can be expressed as the sum of the initial resultant forces and the dynamic resultant forces: i.e., $\mathbf{R} = \mathbf{R}^0 + \mathbf{R}'$, where the first term, $\mathbf{R}^0$, is the resultant force vector which results from the initial stresses, and the second term, $\mathbf{R}'$, is the dynamic resultant force vector which is associated with the shell motion.

The potential energy stored in the element can be expressed in terms of the strain and resultant force vectors: i.e.,

$$U = \frac{1}{2} \int_t \int_{x_1} \int_{x_2} \mathbf{e}^{\mathrm{T}} \mathbf{R} A_1 A_2 dx_1 dx_2 dt \ . \tag{5.6}$$

When the non-linear strains are much smaller than the linear strains ($\mathbf{e}_l >> \mathbf{e}_n$) and the initial resultant forces are much larger than the dynamic resultant forces ($\mathbf{R}^0 >> \mathbf{R}'$), the potential energy represented in Eq. (5.6) can be approximated as $U \cong U_l + U_n$, where $U_l$ and $U_n$ are associated with linear and non-linear strains, respectively: i.e.,

$$U_l = \frac{1}{2} \int_t \int_{x_1} \int_{x_2} \mathbf{e}_l^{\mathrm{T}} \mathbf{C} \mathbf{e}_l A_1 A_2 dx_1 dx_2 dt \tag{5.7}$$

and

$$U_n = \frac{1}{2} \int_t \int_{x_1} \int_{x_2} \mathbf{e}_n^{\mathrm{T}} \mathbf{R}^0 A_1 A_2 dx_1 dx_2 dt \ . \tag{5.8}$$

The kinetic energy can be expressed as

$$T = \frac{1}{2} \int_t \int_{x_1} \int_{x_2} \rho h \dot{\mathbf{y}}^{\mathrm{T}} \boldsymbol{\chi}^{\mathrm{T}} \boldsymbol{\chi} \dot{\mathbf{y}} A_1 A_2 dx_1 dx_2 dt \ , \tag{5.9}$$

where $\rho$ is the density. Finally, the work performed by external distributed forces is

$$W_q = \int_t \int_{x_1} \int_{x_2} \mathbf{y}^{\mathrm{T}} \boldsymbol{\chi}^{\mathrm{T}} \mathbf{Q} A_1 A_2 dx_1 dx_2 dt \tag{5.10}$$

and the work performed by external point forces is

$$W_f = \int_t \int_{x_1} \int_{x_2} \mathbf{y}^{\mathrm{T}} \boldsymbol{\chi}^{\mathrm{T}} \mathbf{F} A_1 A_2 dx_2 dt \ , \tag{5.11}$$

where $\mathbf{Q}$ and $\mathbf{F}$ are the external distributed and point force vectors, respectively.

### 5.2.3 Element Equations

The element equations can be obtained by taking a small variation of the nodal displacements in the energy expression: i.e.,

$$\delta\left(U_l + U_n - T - W_q - W_f\right) = 0\,. \tag{5.12}$$

By substituting Eqs. (5.7) to (5.11) into Eq. (5.12), the system equation for one element can be derived as

$$\sum_{m=0}^{4}\mathbf{K}_m\frac{\partial^m\mathbf{y}}{\partial x_2^m} + \sum_{m=0}^{2}\mathbf{K}_m^0\frac{\partial^m\mathbf{y}}{\partial x_2^m} + \mathbf{M}\frac{\partial^2\mathbf{y}}{\partial t^2} = \mathbf{F}^e + \mathbf{F}^i + \mathbf{Q}^e\,, \tag{5.13}$$

where $\mathbf{K}_m$ is the 8 by 8 $m$-th stiffness matrix (the superscript, "0" denotes that the stiffness matrix is associated with the initial stresses), $\mathbf{M}$ is the 8 by 8 mass matrix, $\mathbf{F}^i$ and $\mathbf{F}^e$ are the 8 by 1 internal and external ($\mathbf{F}^e = [F_{11}\ F_{12}\ F_{21}\ F_{22}\ F_{31}\ F_{41}\ F_{32}\ F_{42}]^{\mathrm{T}}$) nodal force vectors, respectively, and $\mathbf{Q}^e$ is the 8 by 1 distributed force vector ($\mathbf{Q}^e = [Q_{11}\ Q_{12}\ Q_{21}\ Q_{22}\ Q_{31}\ Q_{41}\ Q_{32}\ Q_{42}]^{\mathrm{T}}$). Those various quantities are expressed as:

$$\mathbf{K}_0 = \int_{x_1=0}^{L}\mathbf{E}_0^{\mathrm{T}}\mathbf{C}\mathbf{E}_0 A_1 A_2 dx_1\,, \tag{5.14}$$

$$\mathbf{K}_1 = \int_{x_1=0}^{L}\left(\mathbf{E}_0^{\mathrm{T}}\mathbf{C}\mathbf{E}_1 - \mathbf{E}_1^{\mathrm{T}}\mathbf{C}\mathbf{E}_0\right)A_1 A_2 dx_1\,, \tag{5.15}$$

$$\mathbf{K}_2 = \int_{x_1=0}^{L}\left(\mathbf{E}_0^{\mathrm{T}}\mathbf{C}\mathbf{E}_2 - \mathbf{E}_1^{\mathrm{T}}\mathbf{C}\mathbf{E}_1 + \mathbf{E}_2^{\mathrm{T}}\mathbf{C}\mathbf{E}_0\right)A_1 A_2 dx_1\,, \tag{5.16}$$

$$\mathbf{K}_3 = \int_{x_1=0}^{L}\left(-\mathbf{E}_1^{\mathrm{T}}\mathbf{C}\mathbf{E}_2 + \mathbf{E}_2^{\mathrm{T}}\mathbf{C}\mathbf{E}_1\right)A_1 A_2 dx_1\,, \tag{5.17}$$

$$\mathbf{K}_4 = \int_{x_1=0}^{L}\mathbf{E}_2^{\mathrm{T}}\mathbf{C}\mathbf{E}_2 A_1 A_2 dx_1\,, \tag{5.18}$$

$$\mathbf{K}_0^0 = \int_{x_1=0}^{L}\left(\frac{N_{11}^0}{A_1^2}\frac{d\boldsymbol{\chi}_3}{dx_1}\frac{d\boldsymbol{\chi}_3^{\mathrm{T}}}{dx_1} - \frac{1}{A_1 A_2}\frac{\partial N_{12}^0}{\partial x_2}\boldsymbol{\chi}_3\frac{d\boldsymbol{\chi}_3^{\mathrm{T}}}{dx_1}\right)A_1 A_2 dx_1\,, \tag{5.19}$$

$$\mathbf{K}_1^0 = \int_{x_1=0}^{L} \left( -\frac{1}{A_2^2}\frac{\partial N_{22}^0}{\partial x_2}\boldsymbol{\chi}_3\boldsymbol{\chi}_3^{\mathrm{T}} + \frac{N_{12}^0}{A_1 A_2}\frac{d\boldsymbol{\chi}_3}{dx_1}\boldsymbol{\chi}_3^{\mathrm{T}} - \frac{N_{12}^0}{A_1 A_2}\boldsymbol{\chi}_3\frac{d\boldsymbol{\chi}_3^{\mathrm{T}}}{dx_1} \right) A_1 A_2 dx_1 \,, \tag{5.20}$$

$$\mathbf{K}_2^0 = \int_{x_1=0}^{L} -\frac{N_{22}^0}{A_2^2}\boldsymbol{\chi}_3\boldsymbol{\chi}_3^{\mathrm{T}} A_1 A_2 dx_1 \,, \tag{5.21}$$

$$\mathbf{M} = \int_{x_1=0}^{L} \rho h \boldsymbol{\chi}\boldsymbol{\chi}^{\mathrm{T}} A_1 A_2 dx_1 \,, \tag{5.22}$$

$$F_{m1} = N_{1m} A_1 A_2 \big|_{x_1=0} \; (m = 1,2,3) \,, \tag{5.23}$$

$$F_{m2} = N_{1m} A_1 A_2 \big|_{x_1=L} \; (m = 1,2,3) \,, \tag{5.24}$$

$$F_{41} = M_{11} A_1 A_2 \big|_{x_1=0} \,, \tag{5.25}$$

$$F_{42} = M_{11} A_1 A_2 \big|_{x_1=L} \,, \tag{5.26}$$

$$Q_{mn} = \int_{x_1=0}^{L} q_m \chi_{mn} A_1 A_2 dx_1 \; (m = 1,2,3) \,, \tag{5.27}$$

$$Q_{4n} = \int_{x_1=0}^{L} q_3 \chi_{4n} A_1 A_2 dx_1 \,, \tag{5.28}$$

where $q_m$ is the distributed force in the $x_m$-direction. Note that in Eqs. (5.23) to (5.26), it is assumed that there are four external point forces applied to the element; i.e., $N_{11}$, $N_{12}$, $N_{13}$, and $M_{11}$.

When more than one element is used to represent a system, a global system equation can be assembled from the individual element equations by applying conditions of displacement continuity and force balance at each node. Note that during the latter procedure, the internal force vectors that appear in Eq. (5.13) cancel out.

### 5.2.4 Solution Procedure

Once the global system equation is obtained, boundary conditions should be applied. To

obtain the initial stresses, the static equation, which does not include the mass matrix and the stiffness matrices associated with initial stresses, should first be solved under the appropriate static forcing condition to yield the static displacements. Then the resulting static displacements can be used to obtain the initial resultant forces by using Eq. (5.5) combined with Eq. (5.4). Based on those forces, the stiffness matrices associated with the initial stresses can be calculated by using Eqs. (5.19) to (5.21).

In a dynamic analysis, the natural frequencies and modes are first obtained from the global system equation without external forces. Note that the natural vibration response must satisfy the condition of circular symmetry. Thus, the natural modes can be represented as

$$\mathbf{u}_{mn}(x_1, x_2, t) = \mathbf{U}_{mn}(x_1)\exp(-inx_2 + i\omega_{mn}t), \tag{5.29}$$

where $x_2$ is the circumferential direction and $n$ is the circumferential mode number, which can be an arbitrary integer. By substituting Eq. (5.29) into the global system equation, an eigenvalue problem is formulated: i.e.,

$$\left(\sum_{m=0}^{4}\overline{\mathbf{K}}_m(-in)^m + \sum_{m=0}^{2}\overline{\mathbf{K}}_m^0(-in)^m - \overline{\mathbf{M}}\omega_{mn}^2\right)\mathbf{U}_{mn} = \mathbf{0}, \tag{5.30}$$

where the upper bar on the matrices indicates the global system matrices. The harmonic, forced response can then be represented by modal superposition as

$$\mathbf{u}(x_1, x_2, t) = \sum_m\sum_n \eta_{mn}\mathbf{U}_{mn}\exp(-inx_2 + i\omega t), \tag{5.31}$$

where the modal coefficient, $\eta_{mn}$, is

$$\eta_{mn} = \frac{f_{mn}}{-\omega^2 + \omega_{mn}^2 + i2\omega\omega_{mn}\xi}, \tag{5.32}$$

$\xi$ is the modal damping ratio,

$$f_{mn} = \frac{1}{\lambda_{mn}}\int_0^{2\pi}\mathbf{U}_{mn}^{\mathrm{H}}(\overline{\mathbf{F}}^e + \overline{\mathbf{Q}}^e)\exp(inx_2)dx_2, \tag{5.33}$$

and

$$\lambda_{mn} = \mathbf{U}_{mn}^{\mathrm{H}}\mathbf{M}\mathbf{U}_{mn}. \tag{5.34}$$

## 5.3 Tire Model

Both the tire treadband model (i.e., the circular cylindrical shell model) and the full FE

model described in Chap. 4 were analyzed by using hybrid, 2-D finite elements. The results obtained by using the hybrid, 2-D FE model were then compared with those obtained by using the analytical model and the 3-D FE model.

Figure 5.2 shows the circular cylindrical shell models: the 3-D FE model is shown in Fig. 5.2(a) (see also Fig. 4.2), while the corresponding hybrid, 2-D FE is shown in Fig. 5.2(b). Note that in the 2-D FE model, both the translational displacement in the $x_1$-direction and the rotational displacement in the $x_2$-direction at the node 13 were assumed to be zero to satisfy symmetric boundary conditions.

Figure 5.3 shows the cross-sectional geometry of a tire. The cross-sectional center points and thicknesses of an uninflated tire were measured at 42 points across a cross-section. Then the two sets of measured data were curve-fitted and 37 points were re-sampled from the resulting curves as shown in Fig. 5.3. Note that nodes 12 to 26 were used to define the treadband elements and nodes 1 to 12 and 26 to 37 were used to represent the sidewall elements. Note also that the treadband thickness is assumed to be constant (see Fig. 5.3(b)).

Based on the cross-sectional geometry, the tire was modeled by using both 2-D finite elements and 3-D finite elements: i.e., the 2-D FE model consisted of 36 elements (37 nodes) while 36×90 elements (90 elements around the half circle) was used for the 3-D FE model (see Fig. 5.4). Note that the 3-D FE model was implemented in ANSYS Version 6.0 and element type SHELL63 was used. Note also that only the upper half tire was modeled in the 3-D FE model since symmetric boundary conditions were applied. Different sets of orthotropic material properties were used for the treadband and sidewall as shown in Table 5.1: they were adapted from the literature [29], were based on physical reasoning, or were obtained by direct measurement of tires. All translational displacements at the edges of the sidewalls (i.e., at the bead) were constrained to be zero. An inflation pressure of 207 kPa (20 psi) was applied to the inside surface in the static analysis, and a point force at the center of the treadband was applied for the dynamic analysis.

## 5.4 Results and Discussion

Figure 5.5 shows the forced responses, represented in the wave number domain, of an isotropic, circular cylindrical shell obtained by using the analytical model, the 3-D FE model, and the 2-D FE model: the parameters of the treadband are shown in Table 5.2.

It can be seen that the results shown in Fig. 5.5 are nearly identical, although in the analytical result, the cut-on frequency (approximately 1 kHz) of the second flexural wave mode is higher than that of the corresponding cut-on frequency in the other results. It can also be seen that the result obtained by using the 3-D model with SHELL63 elements is very close to that obtained by using the 2-D FE model in terms of asymptotic wave speeds and cut-on frequencies.

Next, an orthotropic, circular cylindrical shell was analyzed by using both the 3-D ANSYS model and a 2-D FE model: parameters used for the orthotropic treadband are shown in Table 5.2. The resulting forced responses are shown in Fig. 5.6. For the ANSYS 3-D models, three element types were selected: i.e., SHELL63, SHELL 181, and SHELL99. Note that the second and third element types can be used to analyze layered (or composite) shells. It can be seen that the result of the 3-D FE model using the SHELL63 element agrees closely with the result of the 2-D FE model (see Figs. 5.6(a) and 5.6(d)). However, the 3-D FE models implemented by using SHELL181 and SHELL99 elements are more flexible than the 2-D FE model since their asymptotic wave speeds are slower than those of the 2-D FE model and the cut-on frequencies are lower.

A composite, circular cylindrical shell was also analyzed by using both the 2-D FE model and 3-D FE model implemented by using SHELL99 elements. Three layers having the thicknesses 0.002 m, 0.003 m, and 0.003 m (from the interior to exterior layer, respectively) were considered here. Each layer was specified to have the same material properties as those used for the orthotropic treadband as shown in Table 5.3: however, it was laminated at a different layer angle measured from the axial direction, i.e., to the $x_1$-direction, of the material (i.e., the direction of Young's modulus 1). The layer angles were 90°, 30°, and -30° (from the interior to the exterior layer, respectively). Figure 5.7 shows the resulting forced responses in the wave number domain. It can be seen that the asymptotic wave speeds in the result obtained by using SHELL99 elements are slower than those obtained by using 2-D FE elements and that the cut-on frequencies of the SHELL99 result are lower than those of the 2-D FE result: however, regardless of those differences, the pattern of the dispersion curves are very similar. Note that the differences between the two results can be accounted for by reference to the analogous behavior shown in the results for the orthotropic, circular cylindrical shell model (see Fig. 5.6).

The natural frequencies, $f_{mn} = \omega_{mn}/2\pi$, obtained by using the 2-D FE model of the full tire are shown in Fig. 5.8 as a function of circumferential mode number, $n$: Fig. 5.8(a) shows the results without inflation pressure while Fig. 5.8(b) is for the case with inflation

pressure. Note that each point in the frequency-circumferential mode number plane is associated with a particular wave type and cross-sectional mode shape [33,34]. Thus, the first index, $m$, in the natural frequency, $f_{mn}$, denotes both the wave type and cross-sectional mode shape, while the second index, $n$, denotes the circumferential mode number. It can be seen that when inflation pressure is applied, the first flexural wave, i.e., the trajectory having the lowest natural frequencies for all circumferential mode numbers behaves like a membrane wave: i.e., the points associated with this wave type "straighten out" when the inflation pressure is applied [33,34].

Forced responses in the frequency-circumferential mode number domain are shown in Figs. 5.9 and 5.10: the results in Fig. 5.9 were obtained by using the 3-D FE model while the results in Fig. 5.10 were obtained by using the hybrid, 2-D FE model. To obtain these results, vibrational velocities around the tire circumference at the treadband center points were first calculated by using the FE models and the resulting velocity data, represented in the spatial domain at each frequency, were then decomposed into wave number components, $k_\theta = n/R$, where $R$ is the radius of the tire circumference, by using spatial Fourier transforms. Note that the circumferential phase speed of a particular trajectory is represented by the ratio of angular natural frequency to circumferential wave number ($\omega_{mn}/k_\theta$). By comparing Figs. 5.9(a) and 5.9(b) (or Figs. 5.10(a) and 5.10(b)), the circumferential phase speeds of, in particular, the flexural wave types, increase when the inflation pressure is applied [33,34]. It can also be seen that the results obtained by using the hybrid, 2-D FE model are nearly identical to those obtained by using the 3-D FE model (compare Figs. 5.9(a) and 5.10(a) or Figs. 5.9(b) and 5.10(b)).

## 5.5 Conclusions

In this chapter, a hybrid 2-D finite element for a composite shell was formulated by using the variational principle. For the purpose of validating the hybrid 2-D finite element, both a tire treadband and a full tire were analyzed by using both the hybrid, 2-D FE and 3-D FE models. The FE analysis made by using the hybrid 2-D finite elements yields results in close agreement with the three-dimensional model although the hybrid 2-D FE model features a very small number of finite elements. Furthermore, since the hybrid 2-D FE model uses an exact solution in the circumferential direction, it may yield more accurate solutions.

Table 5.1: List of material properties used for full tire model.

| | Sidewall | Treadband |
|---|---|---|
| Young's Moduli | $E_1 = 1.0\times10^8$ Pa<br>$E_2 = 6.0\times10^7$ Pa | $E_1 = 3.2\times10^8$ Pa<br>$E_2 = 7.5\times10^8$ Pa |
| Shear Modulus | $G_{12} = 2.0\times10^6$ Pa | $G_{12} = 6.0\times10^7$ Pa |
| Poisson's Ratio | $\nu_{12} = 0.45$ | $\nu_{12} = 0.45$ |
| Density | 800 kg/m$^3$ | 1200 kg/m$^3$ |

Table 5.2: List of parameters used for isotropic, circular cylindrical shell model.

| | Treadband |
|---|---|
| Young's Modulus | $E = 4.8\times10^{8}$ Pa |
| Poisson's Ratio | $\nu_{12} = 0.45$ |
| Thickness | $h = 0.008$ m |
| Density | $\rho = 1200$ kg/m$^3$ |
| Radius | $a = 0.32$ m |

Table 5.3: List of parameters used for orthotropic, circular cylindrical shell model.

| | Treadband |
|---|---|
| Young's Moduli | $E_1 = 3.2\times10^8$ Pa<br>$E_2 = 7.5\times10^8$ Pa |
| Shear Modulus | $G_{12} = 5.0\times10^7$ Pa |
| Poisson's Ratio | $\nu_{12} = 0.45$ |
| Density | $\rho = 1200$ kg/m$^3$ |
| Radius | $a = 0.32$ m |
| Thickness | $h = 0.008$ m |

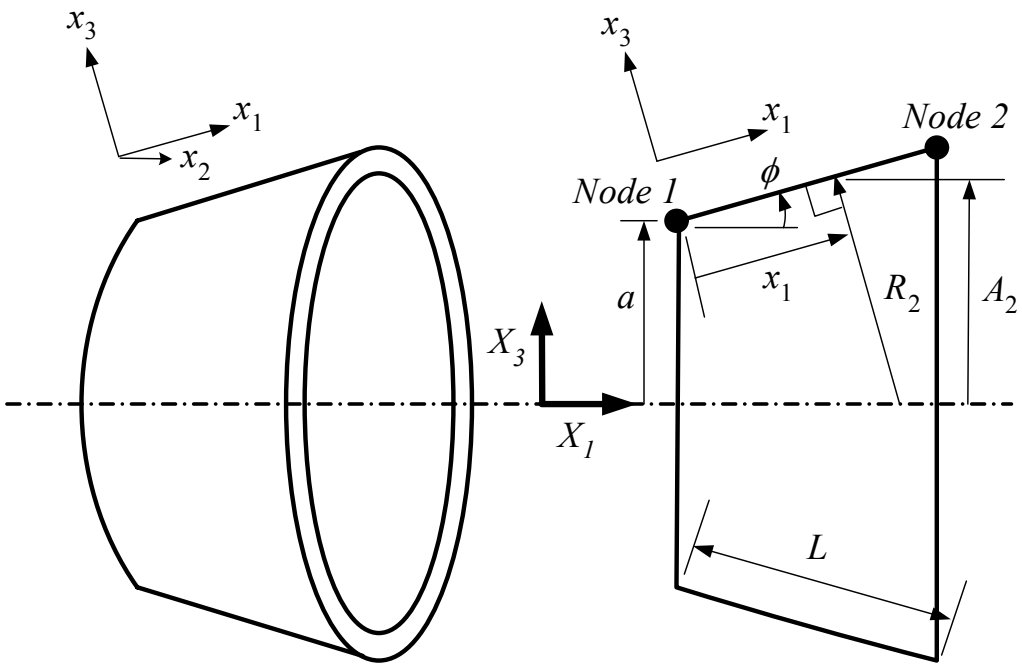


Figure 5.1: Sketch of circular conical shell element.

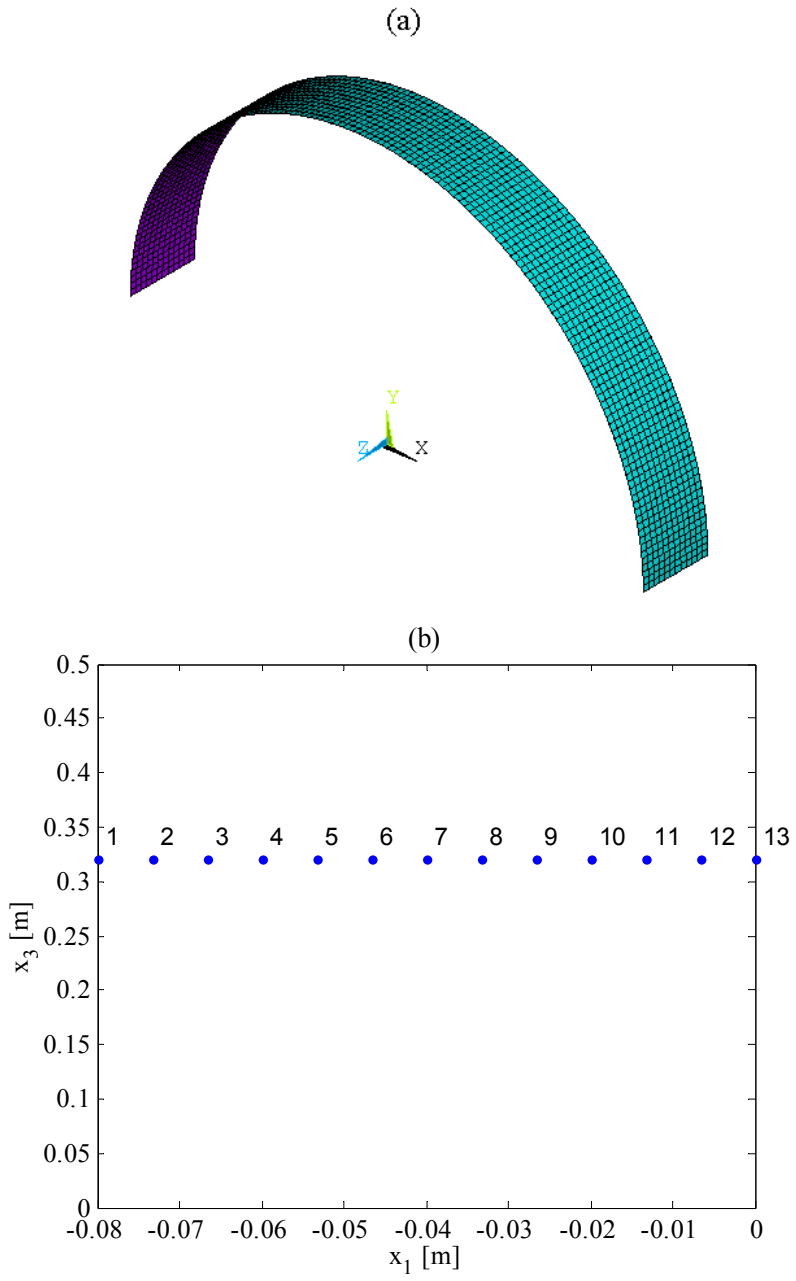


Figure 5.2: Circular cylindrical shell model: (a) 3-D FE model implemented in ANSYS (a quarter of the complete model is used) and (b) nodes used for hybrid, 2-D FE model (half of the complete model is used since symmetric boundary conditions are applied at node 13).

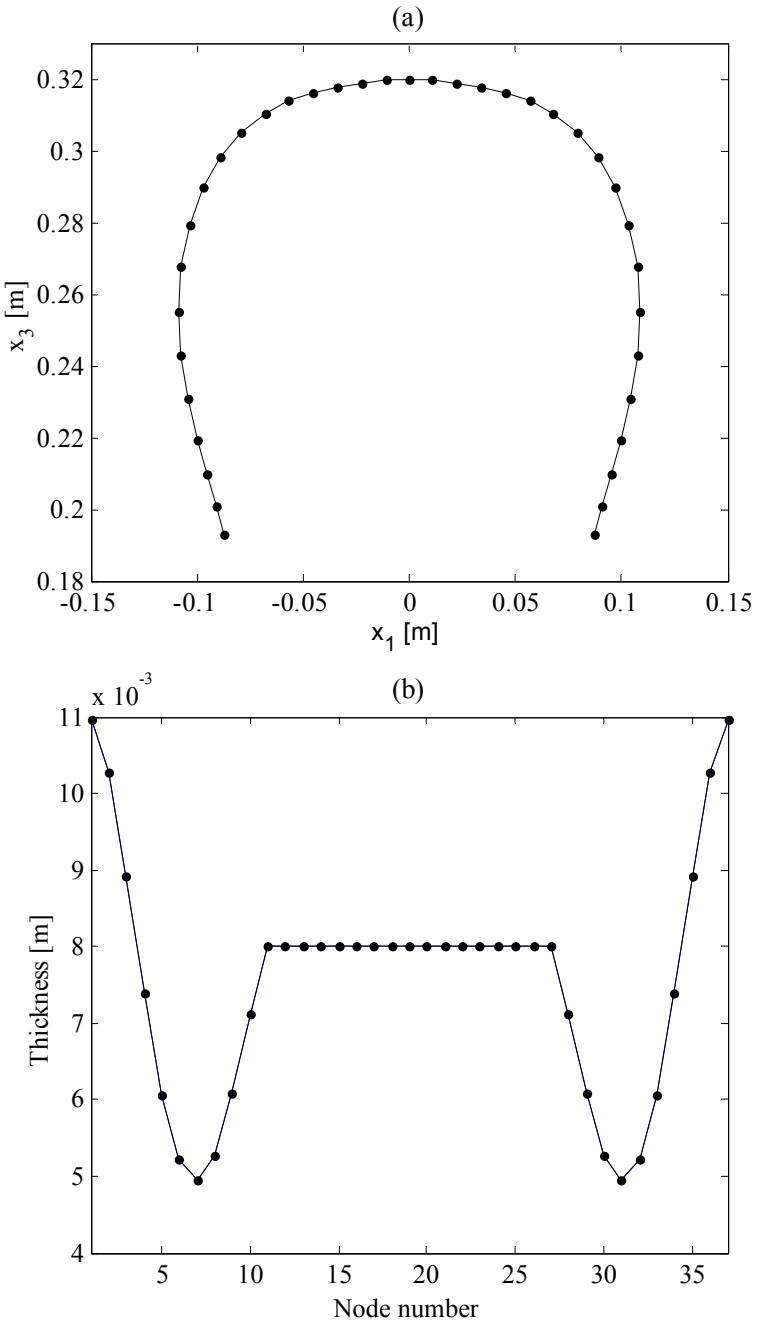


Figure 5.3: Cross-sectional geometry of tire: (a) center points of tire cross-section and (b) thickness.

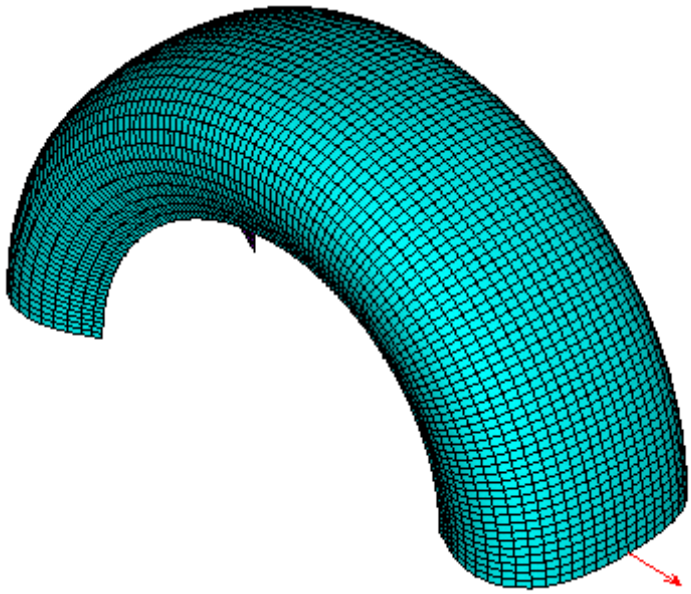

Figure 5.4: 3-D FE model of tire.

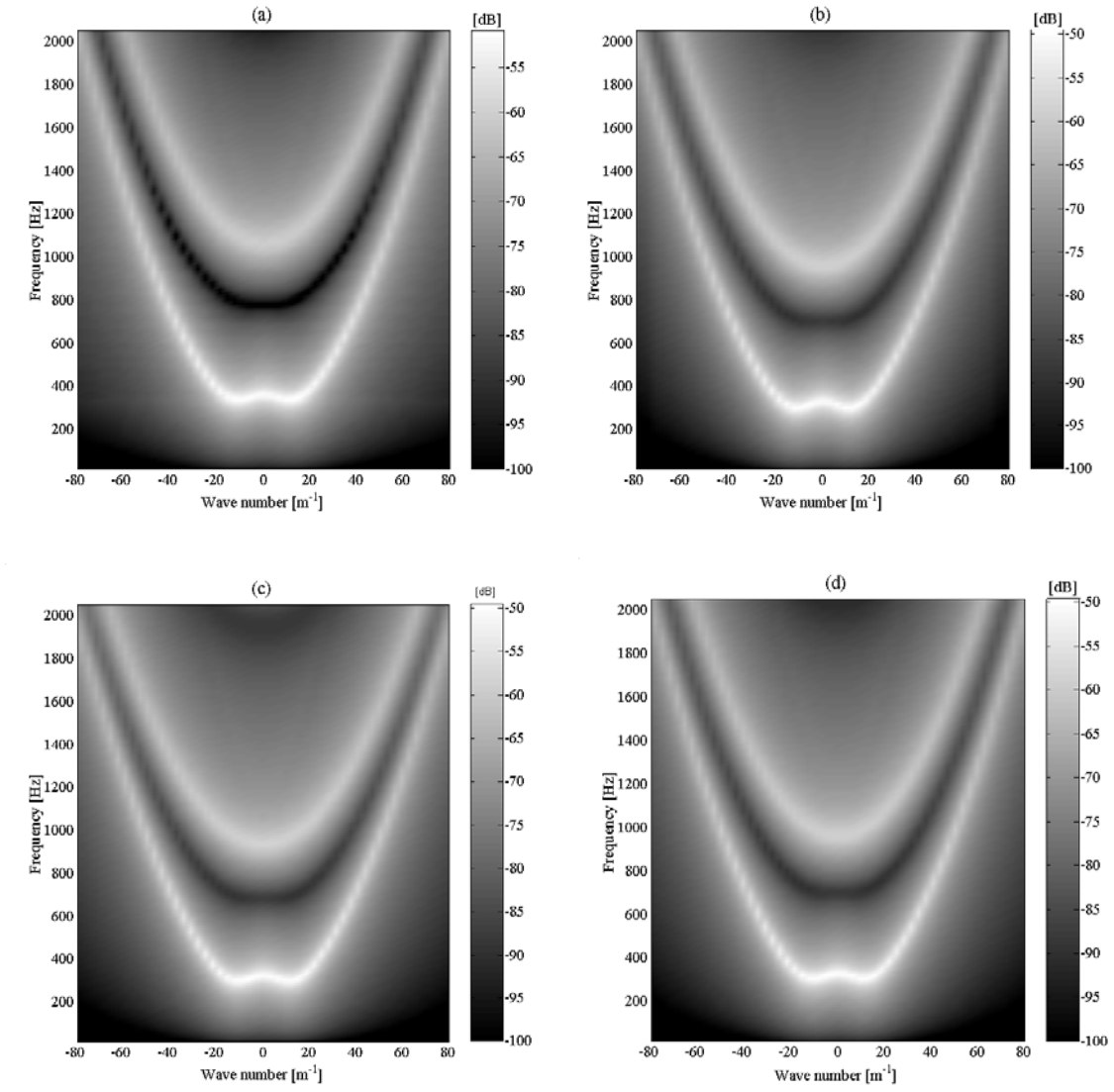


Figure 5.5: Isotropic, circular cylindrical shell model with the inflation pressure of 20 psi: (a) Analytical model, (b) 3-D FE model implemented in ANSYS with SHELL63 elements, (c) 3-D FE model implemented in ANSYS with SHELL181 elements, and (d) 2-D FE model.

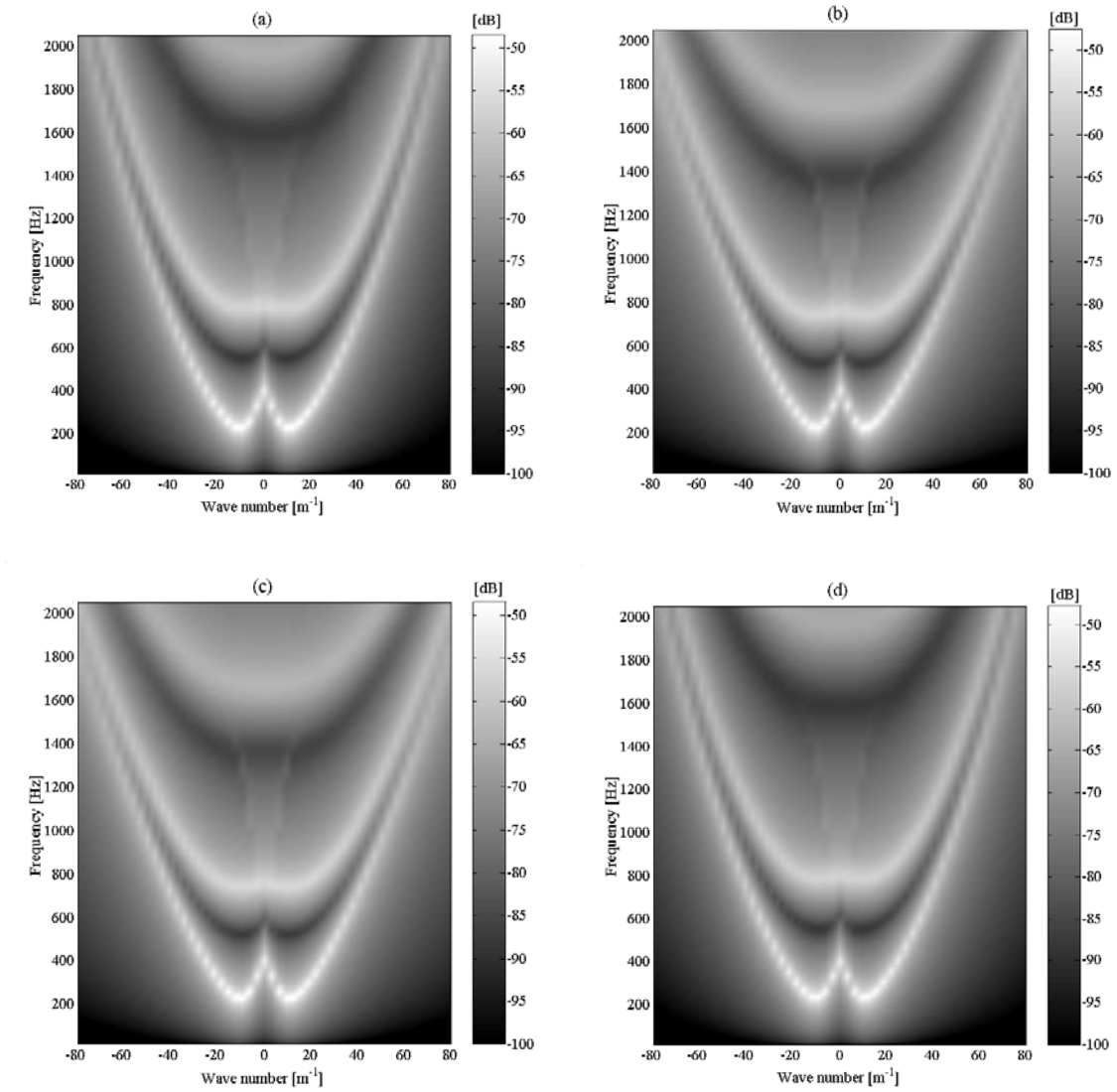


Figure 5.6: Orthotropic, circular cylindrical shell model with the inflation pressure of 20 psi: (a) ANSYS FE model with SHELL63, (b) ANSYS FE model with SHELL181, (c) ANSYS FE model with SHELL99, and (d) 2-D FE model.

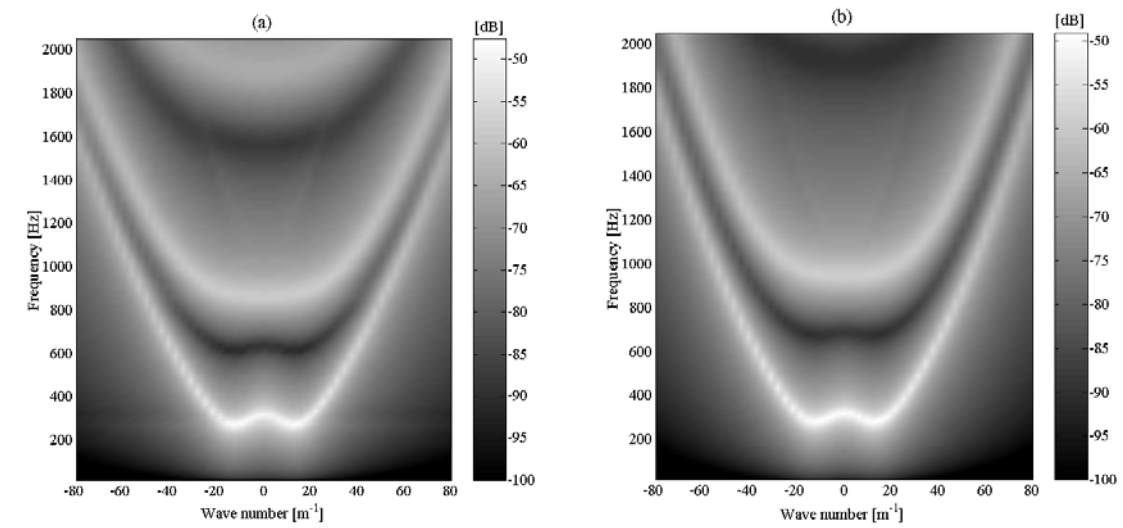


Figure 5.7: Composite, circular cylindrical shell model with the inflation pressure of 20 psi: (a) ANSYS FE model (SHELL99) and (b) 2-D FE model.

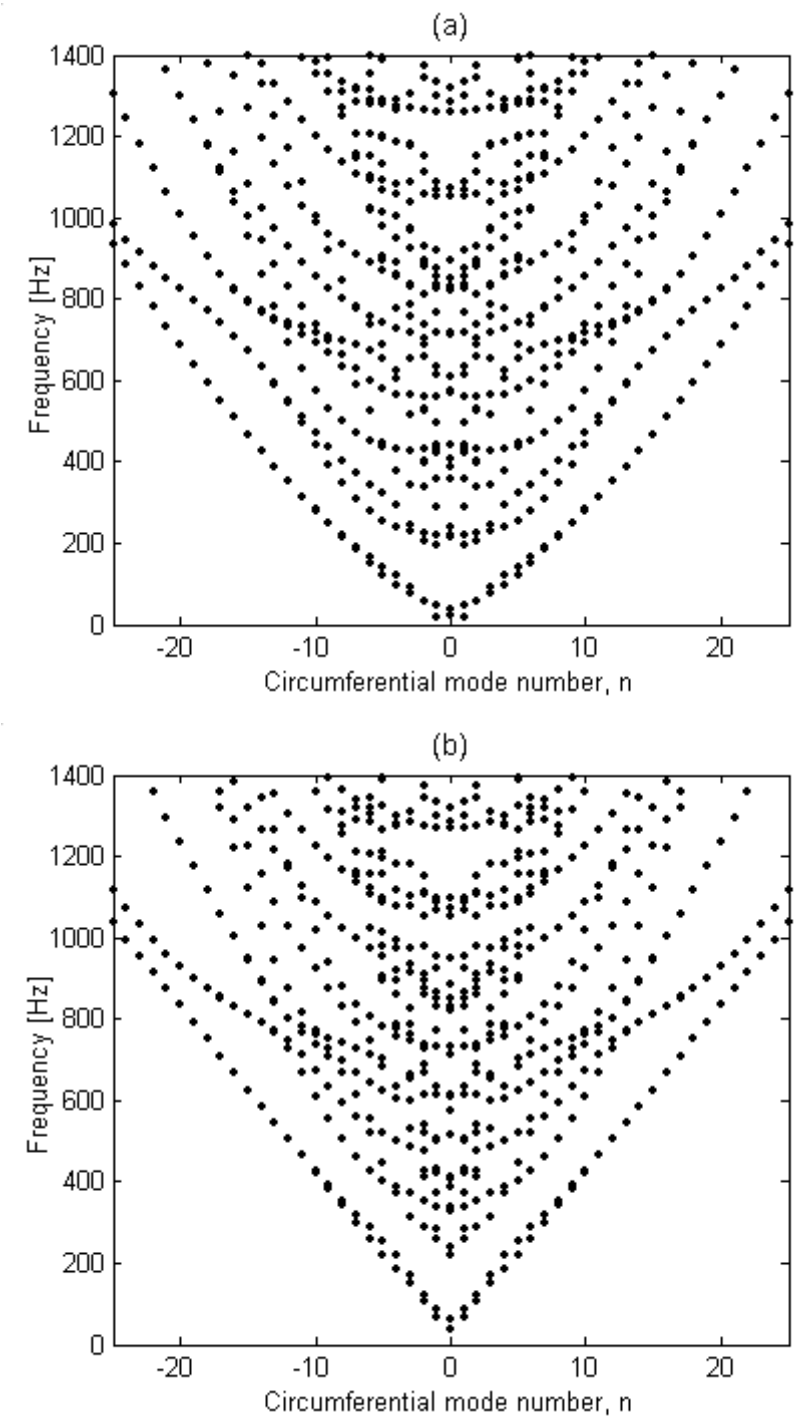


Figure 5.8: Natural frequencies and circumferential mode numbers obtained by using hybrid, 2-D FE model of full tire: (a) without inflation and (b) with inflation.

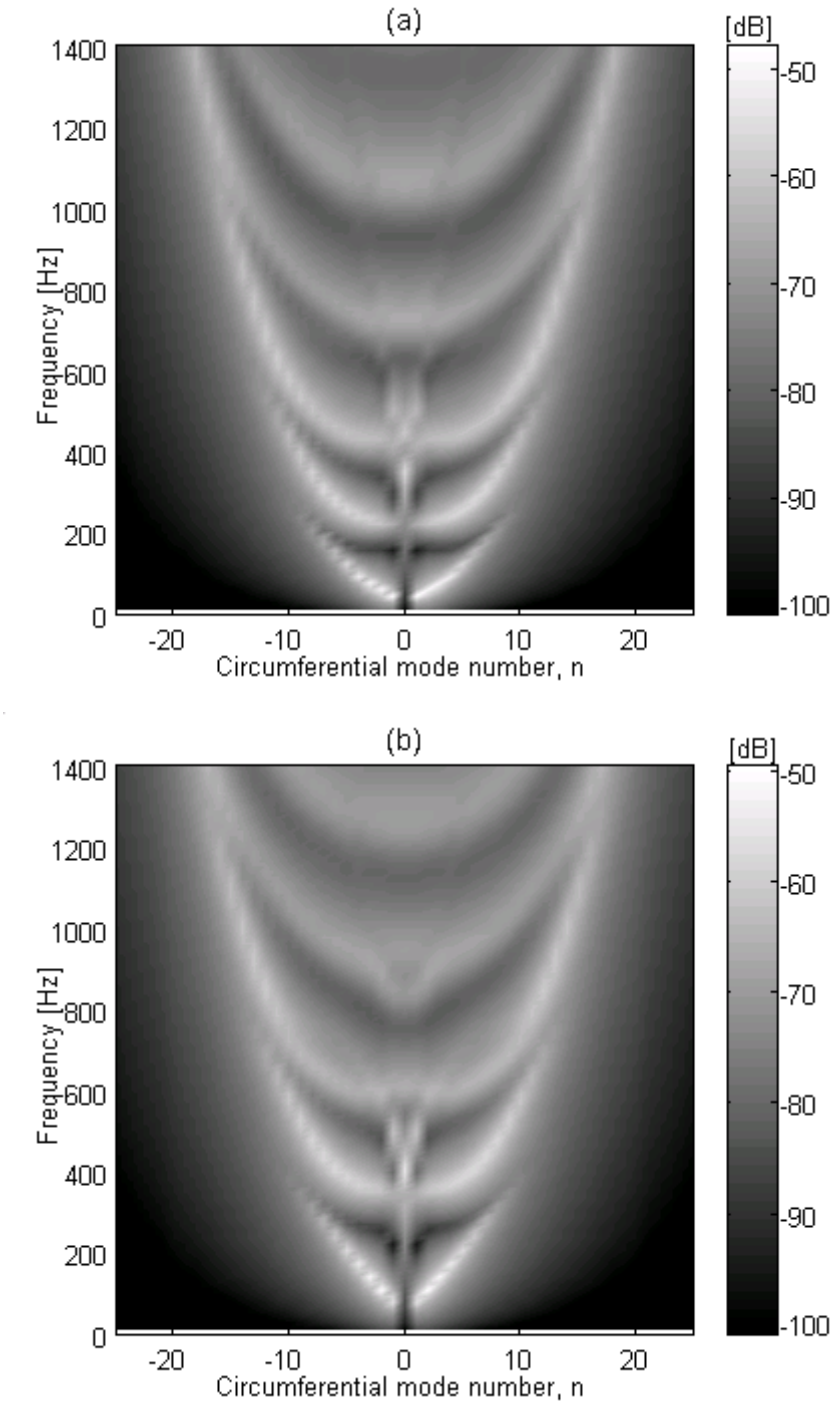


Figure 5.9: Forced response of 3-D FE model of full tire: (a) without inflation and (b) with inflation.

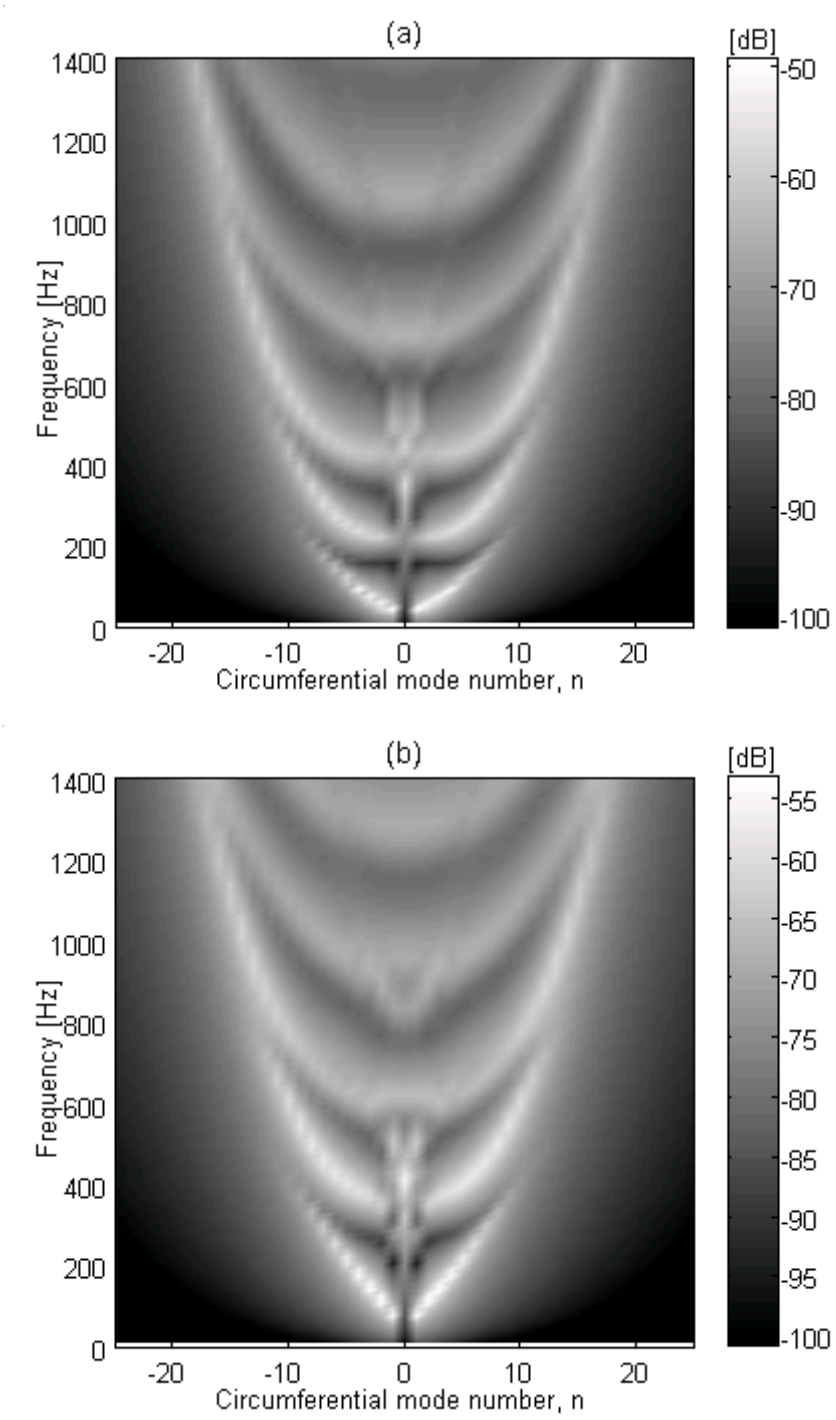


Figure 5.10: Forced response of hybrid, 2-D FE model of full tire: (a) without inflation and (b) with inflation.

# 6. EFFECTS OF ROTATION

For the purpose of understanding the effects of rotation on wave propagation within a tire's treadband, the vibration of an inflated, circular cylindrical shell, rotating about a fixed axis has been considered here. The equations of motion of the rotating shell are formulated in a fixed reference frame (i.e., Eulerian coordinates). By assuming wave-like solutions for the free vibration case, the natural frequencies and corresponding wave-like basis functions can then be obtained. A natural frequency selection procedure is introduced that can be used to associate each of the basis functions with a single natural frequency. The basis functions are then superimposed to represent the forced response of the system when driven by a point harmonic force at a fixed location in the reference frame. By using the procedure described here, the coefficients of the basis functions can be obtained directly by solving an uncoupled ordinary differential equation. Finally, the resulting forced responses are presented in both the spatial and wave number domains, and the wave number spectrum of the rotating shell is compared with that of a stationary shell. Based on the results presented here, it is suggested that at typical rotational speeds it may be possible to use a stationary tire analysis to predict the characteristics of a rotating tire after performing a simple kinematic compensation.

## 6.1 Introduction

Chapters 3 to 5 dealt with the stationary-tire dispersion relations that characterize a tire's dynamics and its potential for sound radiation. In Chap. 3, both an experimental measurement procedure and a wave number decomposition technique for analyzing the radial vibration of a tire were described. In Chaps. 4 and 5, analytical and numerical models of tire treadbands that were found to reproduce the significant features of measured tire dispersion relations were described. The objective of the work described in this chapter was to extend the earlier analytical model to illustrate the effects of

rotation on a tire's dispersion relations. For this purpose, a tire treadband has been modeled as a simply supported, rotating circular cylindrical shell. Both inflation pressure and rotational stiffening were accounted for in the model.

## 6.2 Background

In a rotating shell, a moving particle whose motion is described in local coordinates that rotate with the shell is subject to Coriolis acceleration. As a result, the circumferential phase speeds of the pair of positive- and negative-going waves in the local coordinates differ from each other (when the shell is stationary, they are identical regardless of the wave propagation direction). The latter difference is also observed when the shell motion is described in fixed reference coordinates (i.e., Eulerian coordinates), since, in addition to the effects of Coriolis acceleration, the circumferential phase speed of the positive-going wave increases by the rotation speed, while that of the corresponding negative-going wave decreases by the same amount. Since the natural frequency associated with a particular circumferentially-propagating wave can be related to both the circumferential wave number and the circumferential phase speed, the natural frequency associated with the positive-going wave in the rotating shell is different from that associated with the corresponding negative-going wave. Consequently, a single natural frequency that in the stationary shell case is associated with a pair of positive- and negative-going waves splits into two natural frequencies when the shell rotates. That is, in the stationary shell, the positive- and negative-going waves interfere with each other at a single natural frequency to yield a circumferential standing wave pattern (i.e., a mode shape); however, in the rotating case, a standing wave pattern cannot be generated at a single natural frequency.

When a rotating shell is analyzed by using a circumferential mode shape represented by a circumferential sine or cosine function, the pair of natural frequencies associated with that mode shape can be found; however, the natural frequencies cannot be associated with a particular circumferentially-propagating wave direction. Since the set of mode shapes represented by the circumferential sine and cosine functions is a complete set, as is the set of wave-like basis functions represented by the circumferential complex exponential functions (i.e., positive- and negative-going waves), the forced response can be represented with equal accuracy by the superposition of either the mode shapes or complex exponential functions. However, the modal solution procedure

requires one to solve the complete system differential equations to determine the modal coefficients since a pair of circumferential sine and cosine mode shapes share two natural frequencies (i.e., the modal coefficients are coupled with each other) [53,69,70]. Note that the circumferential mode number, $n$, must be an integer due to circular periodicity; thus, to obtain a complete set of circumferential sine and cosine functions, $n$ should range from zero to positive infinity, while a complete set of circumferential complex exponential functions is obtained by allowing $n$ to range from negative to positive infinity [68].

Padovan obtained the complete set of natural frequencies and corresponding mode shapes for rotating, prestressed circular cylindrical shells [68]. By using those natural modes, Huang and Soedel obtained the forced response of a rotating ring, a special case of a rotating circular cylindrical shell (i.e., no spatial variation was allowed in the axial direction) [69,70]. Note that a ring model can be used to analyze the vibrational characteristics of a rotating tire; however, such a model cannot account for the effects of the cross-sectional modes (in the axial direction). Note also that Kropp has modeled a stationary tire as a stationary ring [29].

Forced solutions for the case of a rotating, prestressed circular cylindrical shell were previously obtained by Huang and Soedel [53]. They expressed their forced responses in terms of sinusoidal and cosinusoidal modes; however, only circumferential sine *or* cosine functions were used to represent the forced responses, and the $n = 0$ circumferential mode (i.e., the breathing mode), that can be important in terms of sound radiation, was not considered. Unless the shell's motion is represented as a sum of both circumferential sine and cosine functions, including the $n = 0$ circumferential mode, spatial phase information in the circumferential direction cannot be represented accurately. Note, however, that in two earlier papers dealing with rotating rings, Huang and Soedel used a complete set of modes [69,70].

In the past, the equations of motion and the solutions for rotating shells were mainly formulated in a local coordinate system [53,68-70]. However, that type of formulation creates difficulties when applying a sinusoidal point force at a fixed point to simulate a contact patch excitation of a rotating tire since, in the local frame, the response is Doppler shifted. In contrast, a system described in fixed reference coordinates, as here, responds at the frequency of the input force.

Another approach to representing the effects of tire rotation was followed by Vinesse and Nicollet, who modeled a tire as a two-dimensional membrane [28]. They derived the equations of motion in a fixed reference frame, and obtained continuous

dispersion curves, each associated with a particular cross-sectional mode shape, by using a wave-like solution (expressed in terms of a continuously varying circumferential wave number). They also obtained an approximate forced response, which was expressed as a function of time and circumferential position (but not as a function of cross-sectional position), for the case of a rotating point force. In their work, however, effects of flexural stiffness and circumferential curvature were neglected, and in-plane motion was not allowed.

Here, it was decided to express the equations of motion for the case of a rotating, inflated circular cylindrical shell in fixed reference coordinates since the forced response in fixed reference coordinates can be used directly to perform a sound radiation analysis. A wave-like basis solution, which comprises a mode shape in the cross-sectional direction (i.e., the axial direction) and a wave-like solution in the circumferential direction, was then used to obtain the complete sets of natural frequencies and corresponding basis functions (the cross-sectional mode shape is represented by sine and cosine functions, and the circumferential wave-like solution is expressed by a complex exponential function). Here, a natural frequency selection procedure that can be used to associate each wave-like basis function with a single natural frequency is proposed. By the superposition of the basis functions, the forced response of the system can be obtained when the system is driven by a point harmonic force at a fixed location in the reference frame. Since a single basis function is associated with only one natural frequency, a basis function coefficient can be found by solving a single ordinary differential equation. In addition, the wave number decomposition procedure [33] has been applied to the resulting forced responses, thus allowing the dispersion relations for a rotating shell to be represented from the viewpoint of a fixed observer so that they can be easily compared with the dispersion relations for a stationary shell.

## 6.3 Analytical Model of Rotating Tire Treadband

Figure 6.1 shows a cylindrical shell model of a tire treadband: the shell is assumed to rotate about a fixed axis coincident with the origin of the reference coordinate system. Note that the local coordinate system, attached to the treadband, rotates with the treadband and that the reference coordinate system is fixed. In the present analysis, the effects of inflation pressure and rotational stiffening were accounted for through resultant in-plane residual stresses. However, static deformation of the shell due to either

inflation or rotation was neglected: i.e., the treadband was assumed to vibrate around its static, uninflated shape.

When shear deformation, rotary inertia, and non-linear effects are neglected, a set of equations describing the three-dimensional motion of the shell can be derived in local coordinates [52]. Those equations can be transformed into the reference coordinate system by application of Reynolds' theorem: i.e.,

$$\frac{\mathrm{D}}{\mathrm{D}t} = \frac{\partial}{\partial t} + \Omega \frac{\partial}{\partial \phi}, \tag{6.1}$$

where the left hand side represents the time derivative in the local (Lagrangian) coordinates, the first term on the right hand side is the time derivative in the reference (Eulerian) coordinates, $\Omega$ is the angular rotational speed and $\phi$ is the circumferential angle in the reference frame. After applying Eq. (6.1), the governing equations can be expressed as

$$\mathrm{L}_x(u_x, u_\phi, u_r) + \lambda \frac{\mathrm{D}u_x}{\mathrm{D}t} + \rho h \frac{\mathrm{D}^2 u_x}{\mathrm{D}t^2} = q_x(x, \phi, r) \tag{6.2}$$

$$\mathrm{L}_\phi(u_x, u_\phi, u_r) + \lambda \frac{\mathrm{D}u_\phi}{\mathrm{D}t} + \rho h \left( \frac{\mathrm{D}^2 u_\phi}{\mathrm{D}t^2} + 2\Omega \frac{\mathrm{D}u_r}{\mathrm{D}t} - \Omega^2 u_\phi \right) = q_\phi(x, \phi, r) \tag{6.3}$$

$$\mathrm{L}_r(u_x, u_\phi, u_r) + \lambda \frac{\mathrm{D}u_r}{\mathrm{D}t} + \rho h \left( \frac{\mathrm{D}^2 u_r}{\mathrm{D}t^2} - 2\Omega \frac{\mathrm{D}u_\phi}{\mathrm{D}t} - \Omega^2 u_r \right) = q_r(x, \phi, r) \tag{6.4}$$

$$\mathrm{L}_x(u_x, u_\phi, u_r) = -\frac{\partial N_{xx}}{\partial x} - \frac{1}{a} \frac{\partial N_{\phi x}}{\partial \phi} \tag{6.5}$$

$$\mathrm{L}_\phi(u_x, u_\phi, u_r) = -\frac{\partial N_{x\phi}}{\partial x} - \frac{\partial N_{\phi\phi}}{\partial \phi} - \frac{Q_{\phi r}}{a} \tag{6.6}$$

$$\mathrm{L}_r(u_x, u_\phi, u_r) = -\frac{\partial Q_{xr}}{\partial x} - \frac{1}{a} \frac{\partial Q_{\phi r}}{\partial \phi} + \frac{N_{\phi\phi}}{a} - N_{xx}^r \frac{\partial^2 u_r}{\partial x^2} - \frac{N_{\phi\phi}^r}{a^2} \frac{\partial^2 u_r}{\partial \phi^2}, \tag{6.7}$$

where $u$ is the displacement in the direction indicated by the subscript, $N_{ij}$ and $Q_{ij}$ ($i, j = x, \phi, r$) are the resultant in-plane and shear forces (see Appendix C), respectively, the superscript, $r$, denotes residual force, and $q$ is the external force applied in the direction indicated by the subscript. In addition, $\rho$ is the density of the treadband, $h$ is its thickness, $\lambda$ is the damping constant, and $a$ is the tire radius. In Eq. (6.7), the circumferential resultant, in-plane force is related to inflation pressure and rotational speed by

$$N_{\phi\phi}^{r} = ap + \rho h a^2 \Omega^2 , \tag{6.8}$$

where $p$ is the inflation pressure [52].

The linear operators, $L_i$ ($i = x,\phi, r$), are associated with the system's stiffness and thus Eqs. (6.7) and (6.8) indicate how inflation pressure and rotation affect the treadband's stiffness. When the magnitudes of the two terms on the right hand side of Eq. (6.8) are compared, it can be concluded that stiffening effects associated with rotation may be ignored compared to the stiffening effect of inflation pressure at speeds typical of those experienced by a car tire running at normal speeds, at least for the model considered here. The latter result will be demonstrated by calculation later.

## 6.4 Natural Vibration

Simple support conditions were considered to apply constraints in the radial and circumferential, but not the $x$-direction, at the treadband edges. In that case, a set of displacements satisfying those boundary conditions, i.e., sinusoidal or cosinusoidal functions in the $x$-direction, as appropriate, can be identified [52,53]. That set must also be periodic in the circumferential direction. Based upon these various conditions, the set of displacements were assumed to have the wave-like forms

$$u_{xmn}(x,\phi,t) = A_{mn} \cos\left(\frac{m\pi x}{L}\right) \exp\left(i\omega_{mn} t - in\phi\right) \tag{6.9}$$

$$u_{\phi mn}(x,\phi,t) = iB_{mn} \sin\left(\frac{m\pi x}{L}\right) \exp\left(i\omega_{mn} t - in\phi\right) \tag{6.10}$$

$$u_{rmn}(x,\phi,t) = C_{mn} \sin\left(\frac{m\pi x}{L}\right) \exp\left(i\omega_{mn} t - in\phi\right), \tag{6.11}$$

where the coefficients $A$, $B$ and $C$ are assumed to be real. By substituting Eqs. (6.9) to (6.11) into Eqs. (6.2) to (6.4), and setting the input force and damping to zero, a matrix equation similar to that defining an eigenvalue problem can be obtained: i.e.,

$$\begin{bmatrix} k_{11} - \rho h \varpi_{mn}^{\ 2} & k_{12} & k_{13} \\ k_{12} & k_{22} - \rho h(\varpi_{mn}^{\ 2} + \Omega^2) & k_{23} + 2\rho h \Omega \varpi_{mn} \\ k_{13} & k_{23} + 2\rho h \Omega \varpi_{mn} & k_{33} - \rho h(\varpi_{mn}^{\ 2} + \Omega^2) \end{bmatrix} \begin{bmatrix} A_{mn} \\ B_{mn} \\ C_{mn} \end{bmatrix} = \begin{bmatrix} 0 \\ 0 \\ 0 \end{bmatrix}, \tag{6.12}$$

where

$$\varpi_{mn} = \omega_{mn} - n\Omega , \tag{6.13}$$

$$k_{11} = K\left[\left(\frac{m\pi}{L}\right)^2 + \frac{1-\nu}{2}\left(\frac{n}{a}\right)^2\right], \tag{6.14}$$

$$k_{12} = -K\frac{1+\nu}{2}\left(\frac{m\pi}{L}\right)\left(\frac{n}{a}\right), \tag{6.15}$$

$$k_{13} = -\frac{K\nu}{a}\left(\frac{m\pi}{L}\right), \tag{6.16}$$

$$k_{22} = \left(K + \frac{D}{a^2}\right)\left[\frac{1-\nu}{2}\left(\frac{m\pi}{L}\right)^2 + \left(\frac{n}{a}\right)^2\right], \tag{6.17}$$

$$k_{23} = \frac{nK}{a^2} + \frac{nD}{a^2}\left[\left(\frac{m\pi}{L}\right)^2 + \left(\frac{n}{a}\right)^2\right], \tag{6.18}$$

and

$$k_{33} = D\left[\left(\frac{m\pi}{L}\right)^2 + \left(\frac{n}{a}\right)^2\right]^2 + \frac{K}{a^2} + N^r_{xx}\left(\frac{m\pi}{L}\right)^2 + N^r_{\phi\phi}\left(\frac{n}{a}\right)^2. \tag{6.19}$$

In Eq. (6.12), the stiffness terms, $k_{ij}$ ($i,j$=1,2,3), are associated with the linear operators, $L_i$ ($i = x,\phi, r$), and they are given in Eqs. (6.14) to (6.19), where $K$ is the membrane stiffness, $D$ is the bending stiffness, and $\nu$ is the Poisson's ratio. Here, the membrane stiffness is $K = Eh/(1-\nu^2)$ and the bending stiffness is $D = Eh^3/[12(1-\nu^2)]$, where $E$ is the Young's modulus. Further, in Eq. (6.13) the left hand side is the natural frequency in local coordinates while the first term on the right hand side is the natural frequency in the reference coordinate system. For future reference, Eq. (6.13) will be referred to as the "kinematic relation".

The characteristic equation obtained from Eq. (6.12) is sixth order: i.e., there are six natural frequencies associated with the ($m$,$n$)th wave-like solution. However, the six local natural frequencies, of the negative-going, i.e., ($m$,-$n$) wave-like solutions, where $n > 0$, each have the same magnitude but opposite sign of those of the positive-going ($m$,$n$) wave-like solutions. Thus, when a local natural frequency is defined to be positive, the sign convention used in the assumed displacements (see Eqs. (6.9) to (6.11)) means that a positive $n$ denotes a positive-going wave and a negative $n$ a negative-going wave. Thus, for each positive or negative $n$, the three positive local natural frequencies are chosen and the negative natural frequencies are discarded. There are then only three distinct local natural frequencies associated with each ($m$,$n$) wave mode, whether $n > 0$ or $n < 0$. Each

of those frequencies is primarily associated with a particular wave type: i.e., flexural, longitudinal, or shear [34]. Note that the two local natural frequencies associated with the pair of wave-like basis functions propagating in opposite circumferential directions are different even in the local frame owing to the effects of Coriolis acceleration, as will be shown later: this phenomenon is referred to as "bifurcation" [68].

The natural frequencies for all possible combinations of $m$ and $n$ (for both positive and negative $n$) can be found by numerically solving the characteristic equation derived analytically from Eq. (6.12). By applying the sign convention described above, the three distinct natural frequencies associated with each $n$ can then be identified. The associated vectors represented by $[A_{mnl}\ B_{mnl}\ C_{mnl}]^{\mathrm{T}}$, where the index $l$ ($l$ = 1 to 3) denotes the three natural frequencies for each $n$, can also be derived by using Eq. (6.12): i.e., the three sets of vectors can be calculated by substituting each of the natural frequencies in sequence into Eq. (6.12). As a result, a single natural frequency, $\omega_{mnl}$, can be associated with a particular wave-like basis vector function represented by

$$\mathbf{\Psi}_{mnl}(x,\phi) = \begin{bmatrix} A_{mnl}\cos\left(\dfrac{m\pi x}{L}\right) \\ iB_{mnl}\sin\left(\dfrac{m\pi x}{L}\right) \\ C_{mnl}\sin\left(\dfrac{m\pi x}{L}\right) \end{bmatrix} \exp(-in\phi). \tag{6.20}$$

## 6.5 Forced Vibration

The forced response can be then expressed as a superposition of the basis functions given in Eq. (6.20): i.e.,

$$u_x(x,\phi,t) = \sum_{m=1}^{\infty}\sum_{n=-\infty}^{\infty}\sum_{l=1}^{3} A_{mnl}\cos\left(\frac{m\pi x}{L}\right)\exp(-in\phi)\eta_{mnl}(t), \tag{6.21}$$

$$u_\phi(x,\phi,t) = \sum_{m=1}^{\infty}\sum_{n=-\infty}^{\infty}\sum_{l=1}^{3} iB_{mnl}\sin\left(\frac{m\pi x}{L}\right)\exp(-in\phi)\eta_{mnl}(t), \tag{6.22}$$

and

$$u_r(x,\phi,t) = \sum_{m=1}^{\infty}\sum_{n=-\infty}^{\infty}\sum_{l=1}^{3} C_{mnl}\sin\left(\frac{m\pi x}{L}\right)\exp(-in\phi)\eta_{mnl}(t). \tag{6.23}$$

Note that for the purpose of compactness, the index, $mnl$ is replaced by $k$ in the following equations. The weighting function (i.e., the coefficient of the basis function), $\eta_k(t)$, can

be calculated by substituting Eqs. (6.21) to (6.23) into Eqs. (6.2) to (6.4) and then applying Eqs. (6.12) and (6.13) with damping and forcing terms included. The result is

$$\ddot{\eta}_k + \left(\frac{\lambda_k}{\rho h} - i2\Omega(n+2\gamma_k)\right)\dot{\eta}_k + \left(\omega_k^2 - 2\Omega\omega_k(n+2\gamma_k) - in\Omega\frac{\lambda_k}{\rho h}\right)\eta_k = \frac{F_k}{\rho h W_k}, \quad (6.24)$$

where

$$W_k = \pi L\left(A_k^2 + B_k^2 + C_k^2\right), \quad (6.25)$$

$$\gamma_k = \frac{B_k C_k}{A_k^2 + B_k^2 + C_k^2}, \quad (6.26)$$

and

$$F_k = \int_0^{2\pi}\int_0^L \left[q_x A_k \cos\left(\frac{m\pi x}{L}\right) + iq_\phi B_k \sin\left(\frac{m\pi x}{L}\right) + q_r C_k \sin\left(\frac{m\pi x}{L}\right)\right] e^{in\phi} dx d\phi . \quad (6.27)$$

Equation (6.24) may then be solved to give $\eta_k(t)$ for arbitrary temporal input forces. Note that the modal damping constant, $\lambda_k$, in Eq. (6.24) is here expressed in terms of a constant modal damping ratio, $\xi$, and the natural frequency, $\omega_k$, as

$$\lambda_k = 2\rho h \xi \omega_k . \quad (6.28)$$

Note also that the coefficient of the basis function can be found directly by solving the ordinary differential equation, Eq. (6.24).

Next, consider a harmonic point force applied in the radial direction at a fixed point while the forces in the other directions are assumed to be zero (i.e., $q_x = 0$ and $q_\phi = 0$). This radial force applied at the center of the treadband simulates a contact patch excitation of a rotating tire and it can be expressed as

$$q_r(x,\phi,t) = f_0 \delta\left(x = \frac{L}{2}, \phi = 0\right)\exp(i\omega t), \quad (6.29)$$

where $f_0$ is the constant amplitude of the force and $\delta$ is the Dirac delta function. Given a harmonic force as expressed in Eq. (6.29), the $k$-th response function, $\eta_k(t)$, can also be expressed in harmonic exponential form: i.e.,

$$\eta_k(t) = X_k \exp(i\omega t), \quad (6.30)$$

where $X_k$ is the amplitude of the $k$-th basis function. By substituting Eqs. (6.29) and (6.30) into Eqs. (6.24) to (6.28), the amplitude is obtained as

$$X_k = \frac{f_0 C_k \sin(m\pi/2)}{\rho h W_k\left[\omega_k^2 - \omega^2 - 2\Omega(n+2\gamma_k)(\omega_k - \omega) + i2(\omega - n\Omega)\omega_k\xi\right]}. \quad (6.31)$$

## 6.6 Results And Discussion

The tire treadband parameters used for the calculation presented here are listed in Table 6.1: they were adapted from the literature [29], were based on physical reasoning, or were obtained by direct measurement of tires.

Figure 6.2 shows the dispersion relations obtained by solving the system characteristic equation for each combination of $m$ and $n$; the dispersion relations are therefore defined at a set of discrete points. Note that the $x$-axis of Fig. 6.2 et seq. is the circumferential wave number, $k_\phi$, which is related to the circumferential mode number, $n$, by $k_\phi = n/a$. In Fig. 6.2, each trajectory of the dispersion relation is associated with a particular cross-sectional mode index: i.e., $m = 1$, etc. as shown in Fig. 6.2(a).

For each combination of $m$ and $n$, there are three natural frequencies associated primarily with flexural, shear, and longitudinal motions in order of increasing frequency [34]. The stationary dispersion relations are plotted in Fig. 6.2(a). In Fig. 6.2(b), the local natural frequencies are plotted when the rotation speed was set to the artificially large value of $\Omega = 500$ rad/s to exaggerate the effects of rotation: a more typical range for automotive applications is from $\Omega = 0$ to $\Omega = 100$ rad/s. By comparison of Fig. 6.2(b) with Fig. 6.2(a), two phenomena can be observed. First, it can be seen that the speed of the flexural waves is increased by rotational stiffening (i.e., the slope of the flexural modal trajectories is increased.). In contrast, the change of the speeds of the shear and longitudinal waves is essentially negligible. Secondly, on close examination, it can be seen that rotation causes the dispersion curves to be very slightly asymmetrical with respect to the zero wave number axis: this is the so-called “bifurcation” effect. The latter asymmetry means that the speeds of waves propagating in opposite circumferential directions with the same wavelengths are different even when observed in the local coordinate system. However, the present results indicate that this effect is negligible for the model considered here under normal circumstances (see Fig. 6.2(c)). Results in local coordinates for a more typical rotational speed, $\Omega = 100$ rad/s, are plotted in Fig. 6.2(c). By comparison with the $\Omega = 0$ results in Fig. 6.2(a), it can be seen that the stiffening due to rotation is not very significant in this case, as explained earlier in connection with Eq. (6.8).

Finally, the dispersion relations in the reference frame are plotted in Fig. 6.2(d), also for $\Omega = 100$ rad/s. Note that the latter results were obtained from those of Fig. 6.2(c) by applying the kinematic relation, Eq. (6.13). In Fig. 6.2(d), the asymmetry resulting from the kinematic effect of tire rotation is very clear in contrast with the

bifurcation effect in local coordinates (Fig. 6.2(c)).

For the purpose of validating the modeling and solution procedures, the stationary model ($\Omega = 0$) was reproduced by using a FE model [34]. The corresponding wave number-transformed forced solutions (presented as radial velocity magnitude) for a radial point force on the treadband centerline calculated using FE and analytical procedures are plotted in Fig. 6.3. The two results are identical for practical purposes.

The spatial distributions of the centerline radial velocities for a fixed-location radial point force applied on the shell centerline are plotted at selected frequencies in the reference frame in Fig. 6.4, and the complete set of results, along with the corresponding circumferentially wave number-transformed results are shown in Fig. 6.5. Note that zero deg. in Figs. 6.4 and 6.5(a) indicates the drive point. One interesting aspect of these results is that clear stationary wave patterns (with respect to the fixed frame) appear even under rotation. In a sense, the stationary waves are strengthened by damping, since the latter causes the dispersion trajectories to be broader, thus making it more likely that there will be wave components propagating in opposite directions with the same wavelength at the same frequency. It can also be seen in Fig. 6.4 that the rate of decay with distance increases as the damping ratio is increased (compare Figs. 6.4(a) and 6.4(b)) and that the effect of damping increases with frequency. Thus, at high frequencies the response becomes similar to a free-field response as the damping is increased: e.g., at $f = 3200$ Hz, $\xi = 0.05$, the response level drops by approximately 40 dB by half-way around the treadband. The latter result is consistent with measurements made on stationary tires [33,43]. Further, a comparison of the responses in the positive- and negative-$\phi$ regions of Fig. 6.4 (i.e., in the upstream and downstream directions, respectively) shows that the levels are generally higher in the downstream direction. The latter effect becomes clearer as the rotational speed increases (compare Figs. 6.4(b) and 6.4(c)). These various effects can also be seen in Fig. 6.5(a). In the higher frequency region of Fig. 6.5(a) it is also clear that several wave modes, each having different wavelengths, contribute significantly to the response simultaneously. The latter is also clear in the wave number-transformed results shown in Fig. 6.5(b). It can also be seen that the even cross-sectional modes (i.e., $m = 2,4,6,\cdots$) are absent from the results of Fig. 6.5(b) (compare with Fig. 6.2(d)) since the point force was applied at the center of treadband. Also note that the trajectories in Fig. 6.5(b) are continuous (not discrete, as in Fig. 6.2), in part because of the effect of damping. The asymmetry of the trajectory slopes in Fig. 6.5(b) also indicates that waves travel more quickly downstream ($k_\phi > 0$) than upstream, as expected.

Finally, the input point mobility, $i\omega u_r/q_r$, associated with the negative- and positive-going wave components is shown in Fig. 6.6. The results were calculated by summing Eq. (6.23) separately over positive and negative $n$, and assigning half of the $n$ = 0 component to each summation. The mobility associated with the positive-going (i.e., downstream) components is generally larger than that associated with the negative-going components (except near the cut-on frequencies of progressively higher order cross-sectional modes) which is consistent with the relative magnitudes of the responses in the up- and downstream sections shown in Fig. 6.4. The sequence of small peaks in the mobility from approximately 400 Hz to 900 Hz (most clearly visible in the positive-going result) are related to the circumferential modes associated with the first cross-sectional mode ($m$ = 1). The contributions of individual modes are not easily visible in the frequency ranges above the cut-on frequencies of the $m$ = 3 and $m$ = 5 cross-sectional modes (near 1000 Hz and 2600 Hz, respectively). The latter observation is also consistent with measured results for tires [43].

Since both the rotational stiffness and bifurcation effects are essentially negligible under the conditions considered here, it is possible to map the stationary forced response (Fig. 6.3(b)) onto the rotational response by using Eq. (6.13) when the local natural frequency is assumed to be the natural frequency of the stationary tire. In the latter case, Eq. (6.13) can be modified to compensate for rotational effects in the wave number-frequency domain: i.e.,

$$f = f_s + \frac{k_\phi a}{2\pi}\Omega, \tag{6.32}$$

where $f$ and $f_s$ are the rotation-compensated and stationary tire natural frequencies, respectively.

For the purpose of validating Eq. (6.32), parametric representations of the dispersion relations were obtained first by applying the Prony series procedure described in Refs. [33,49]: the resulting real wave numbers are overlaid on the previous results (Figs. 6.3(b) and 6.5(b)) in Fig. 6.7. It can be seen that the real wave numbers thus identified lie on the local maxima of the dispersion relations obtained by application of the spatial Fourier transform. The stationary real wave numbers of Fig. 6.7(a) were then modified by applying Eq. (6.32) to compensate for rotational effects: the results are shown in Fig. 6.8 along with the direct results for the rotational case. It can be seen that the compensated stationary dispersion relations are essentially identical with those of the rotational case.

## 6.7 Conclusion

In the work described here, the treadband of a tire was modeled as an inflated, rotating circular cylindrical shell in order to identify the effects of rotation. A wave-based solution procedure was used to obtain analytical solutions for both free and forced vibration cases. In particular, it was shown that a natural frequency selection procedure described here could be used to select the natural frequencies based on circumferentially-propagating wave characteristics in the rotating shell. Additionally, the forced solutions were obtained by the superposition of wave-like basis functions: in the latter procedure, the superposition coefficient could be determined by solving an uncoupled ordinary differential equation.

The results presented here show that rotation has two principal effects: stiffening of the treadband and kinematic "tilting" of the dispersion curves. It was found, however, that the rotational stiffening effect was not significant compared with the effect of inflation pressure, for the model considered here, at typical rotational speeds. In contrast, the kinematic tilting effect was found to be significant. Thus, it was concluded that a linear function, Eq. (6.32), could be used to adjust stationary shell dispersion curves for the effects of rotation: the latter curves may then be used to analyze the potential of a rotating tire to radiate sound.

Table 6.1: Parameters for tire treadband.

| | |
|---|---|
| Young's Modulus | $E = 4.8\times10^{8}$ N/m$^2$ |
| Density | $\rho = 1200$ kg/m$^3$ |
| Thickness | $h = 0.008$ m |
| Poisson's ratio | $v = 0.45$ |
| Radius | $a = 0.32$ m |
| Width | $L = 0.16$ m |
| Damping ratio | $\xi = 0.05$ |
| Inflation pressure | $p = 206910$ Pa ($p = 30$ psi) |
| Sidewall tension | $N^{r}_{xx} = 2\times10^{4}$ N/m |

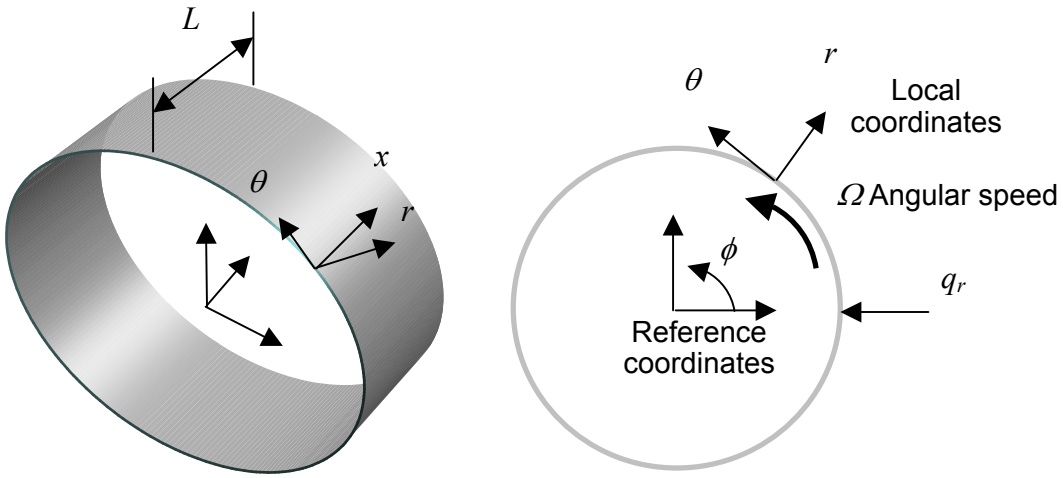


Figure 6.1: Model of tire treadband: a circular cylindrical shell with simply-supported edges.

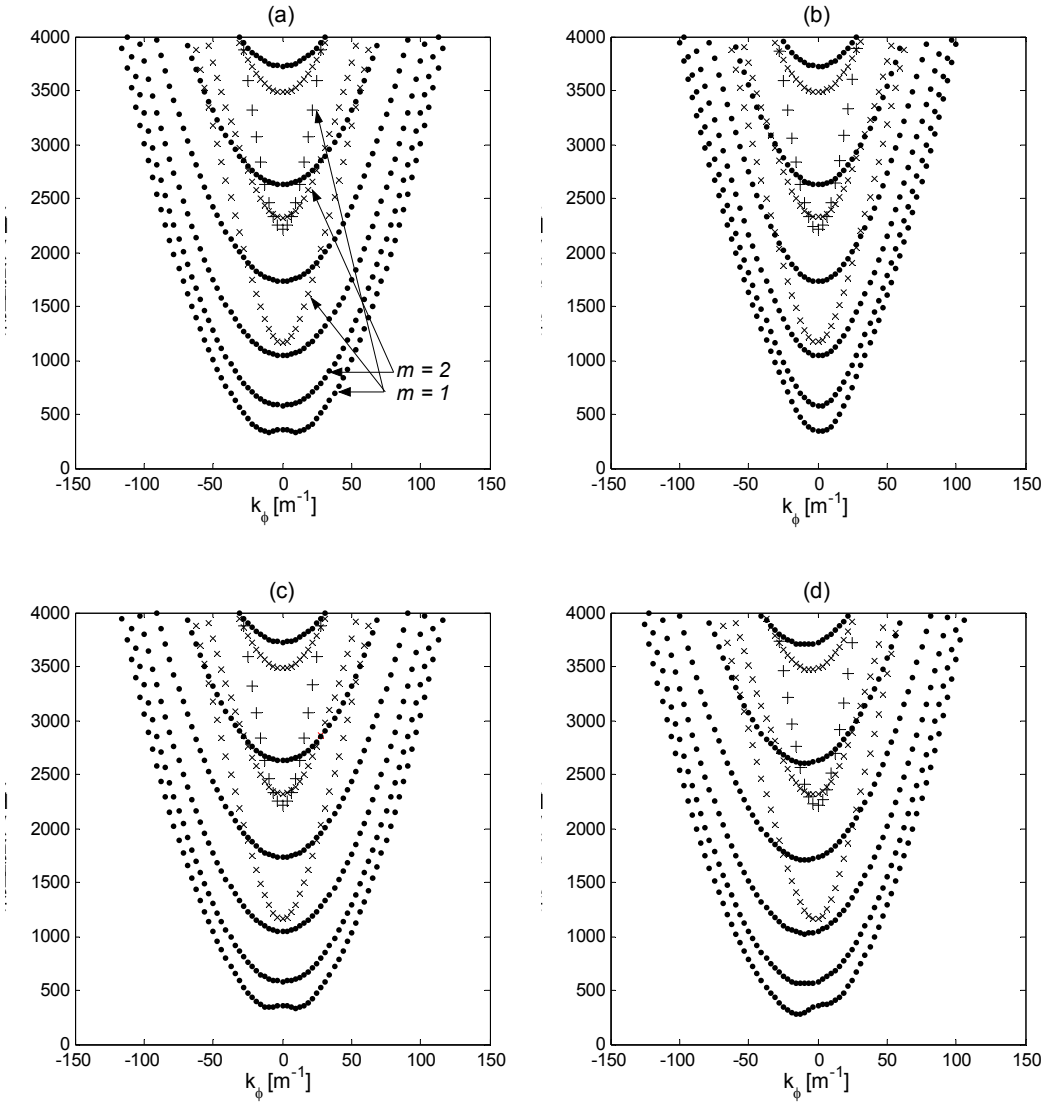


Figure 6.2: Dispersion relations derived from characteristic equation: • - flexural wave, × - shear wave, and + - longitudinal wave: (a) $\Omega = 0$, (b) natural frequencies in local coordinates when $\Omega$ = 500 rad/s, (c) natural frequencies in local coordinates when $\Omega$ = 100 rad/s, and (d) natural frequencies in reference coordinates when $\Omega = 100$ rad/s.

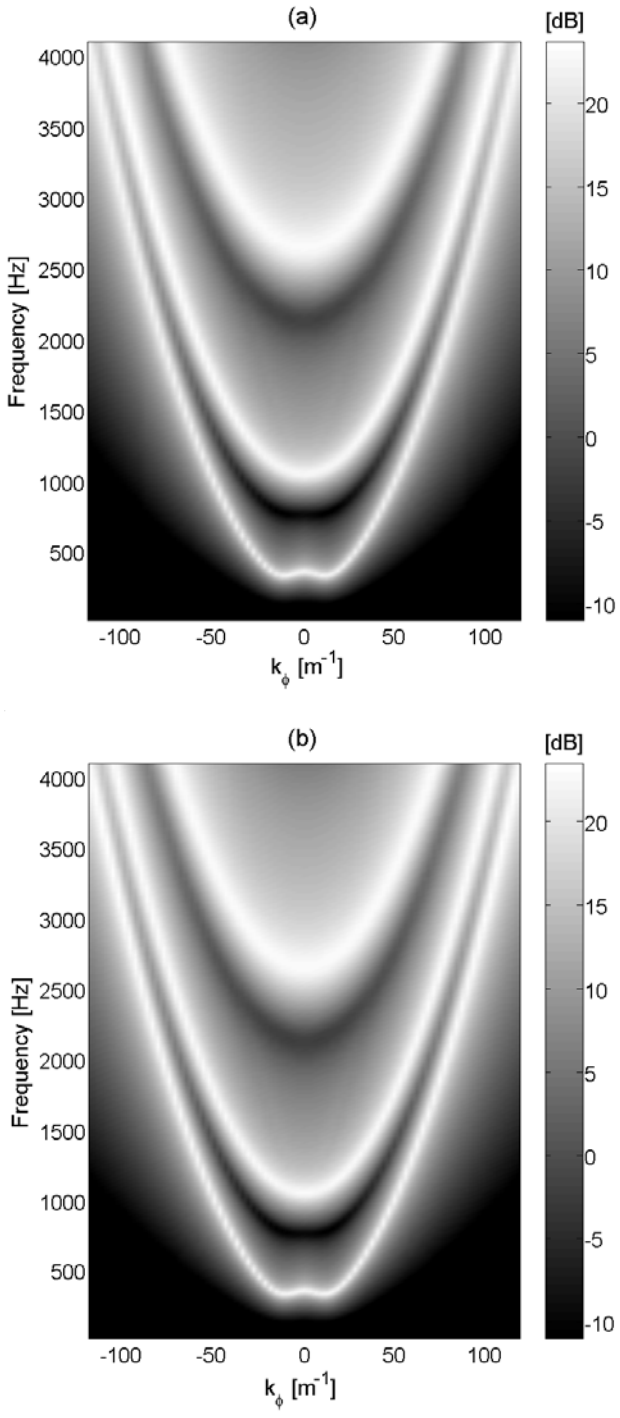


Figure 6.3: Comparison of analytical forced response (radial velocity) with FE simulation when $\Omega$ = 0 rad/s and $\xi$ = 0.05: (a) FE simulation and (b) analytical solution.

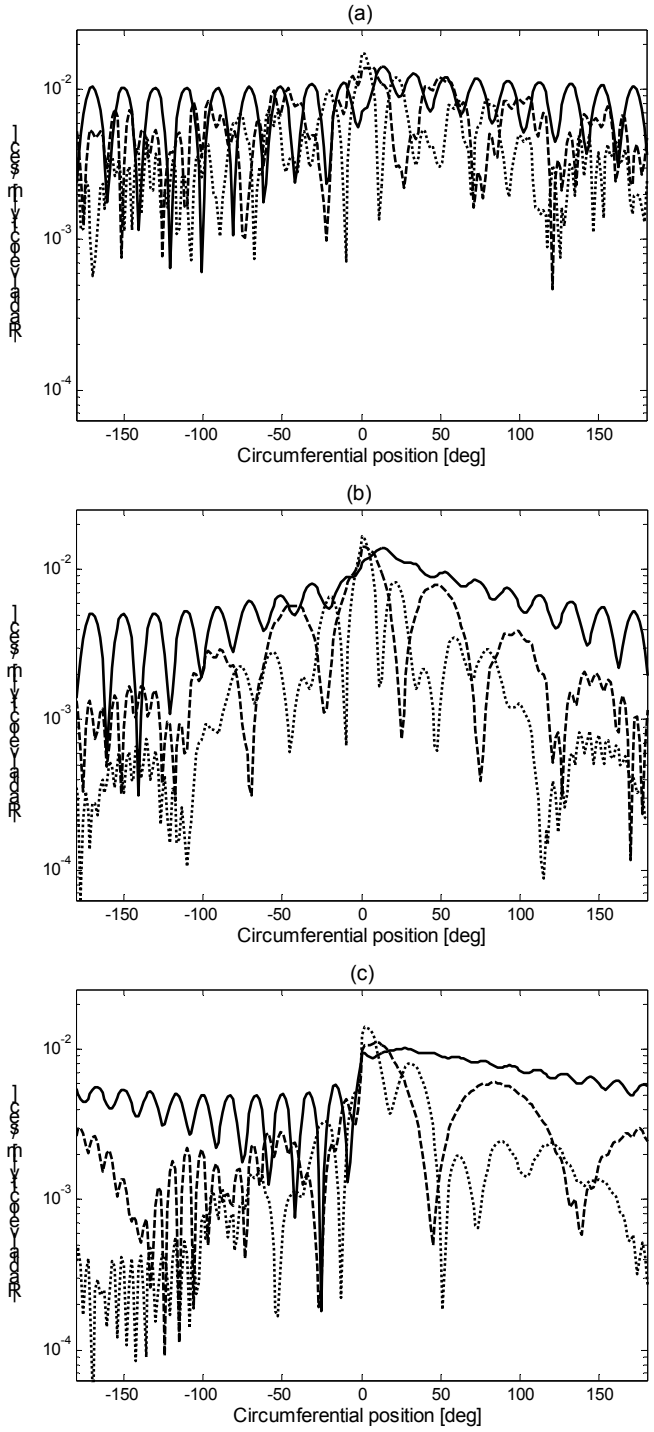


Figure 6.4: Forced responses at 512 Hz (solid line), 1600 Hz (dashed line), and 3200 Hz (dotted line): (a) $\Omega = 100$ rad/s and $\xi = 0.02$, (b) $\Omega = 100$ rad/s and $\xi = 0.05$, and (c) $\Omega = 500$ rad/s and $\xi = 0.05$.

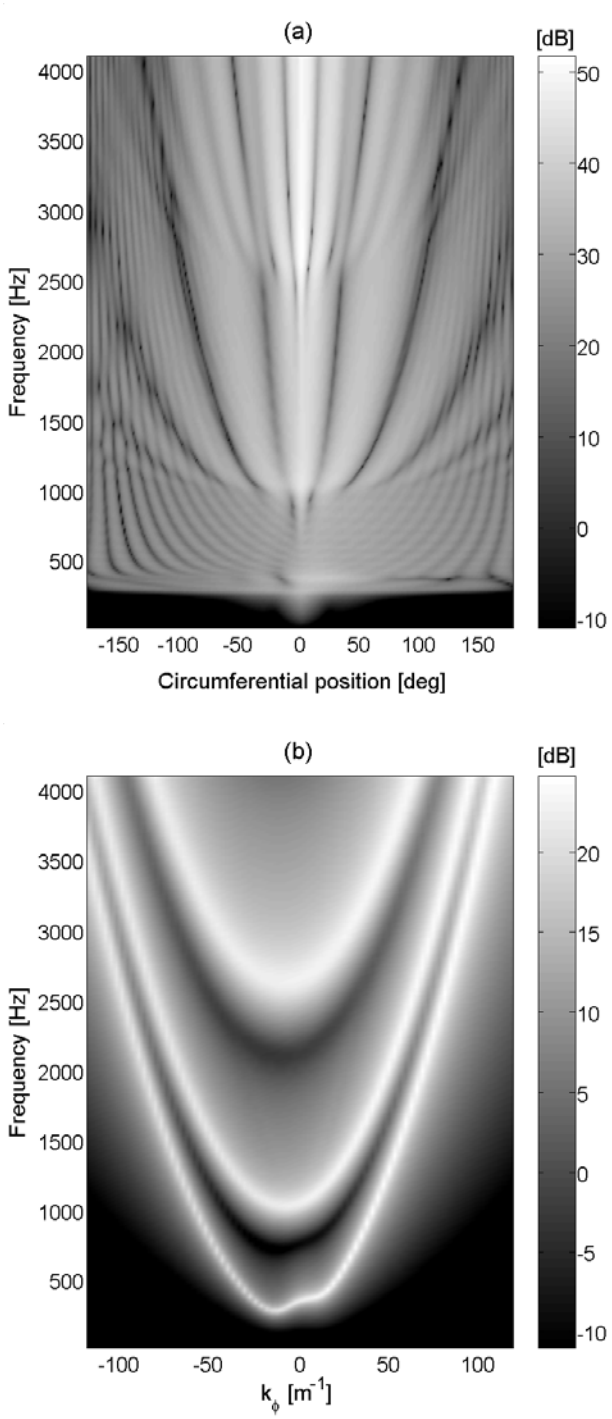


Figure 6.5: Forced response when $\Omega = 100$ rad/s and $\xi = 0.05$: (a) magnitude of vibration (radial velocity) at treadband center and (b) dispersion relation obtained by circumferential wave number transform.

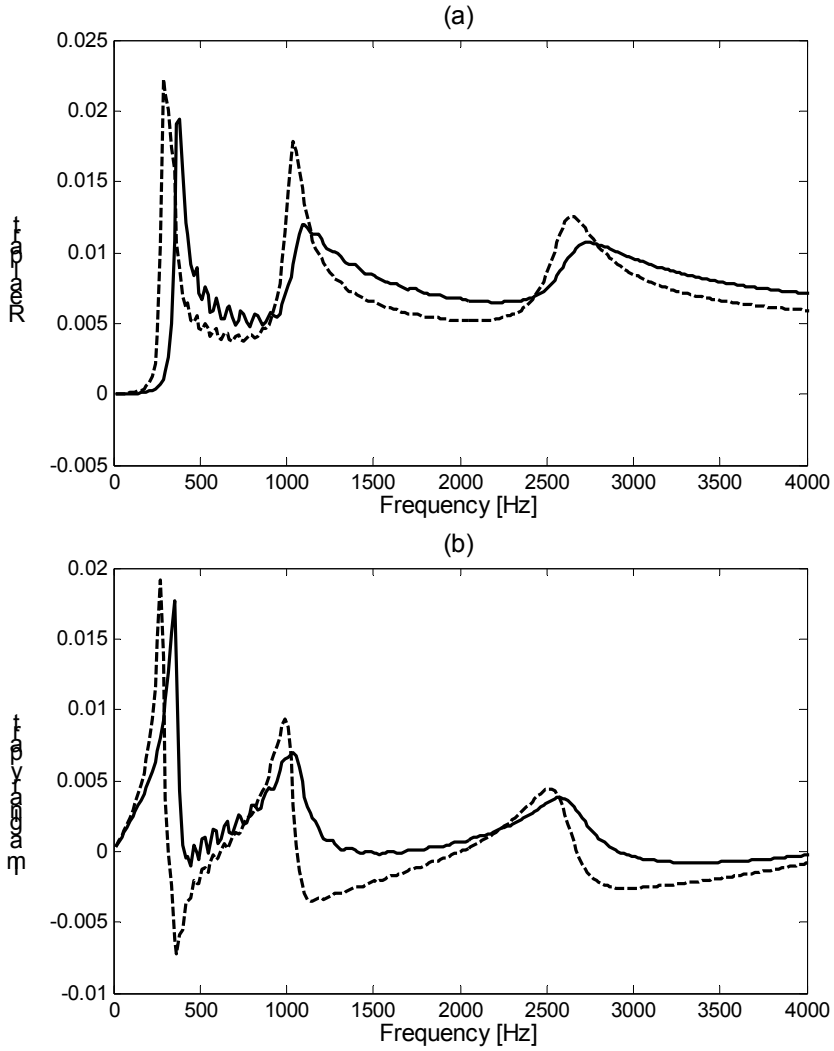


Figure 6.6: Input point mobility, $i\omega u_r/q_r$. Solid line indicates modal summation of positive-going wave components ($n > 0$) and half of $n = 0$ component, and dashed line indicates negative-going wave components ($n < 0$) and half of $n = 0$ component: (a) real part and (b) imaginary part.

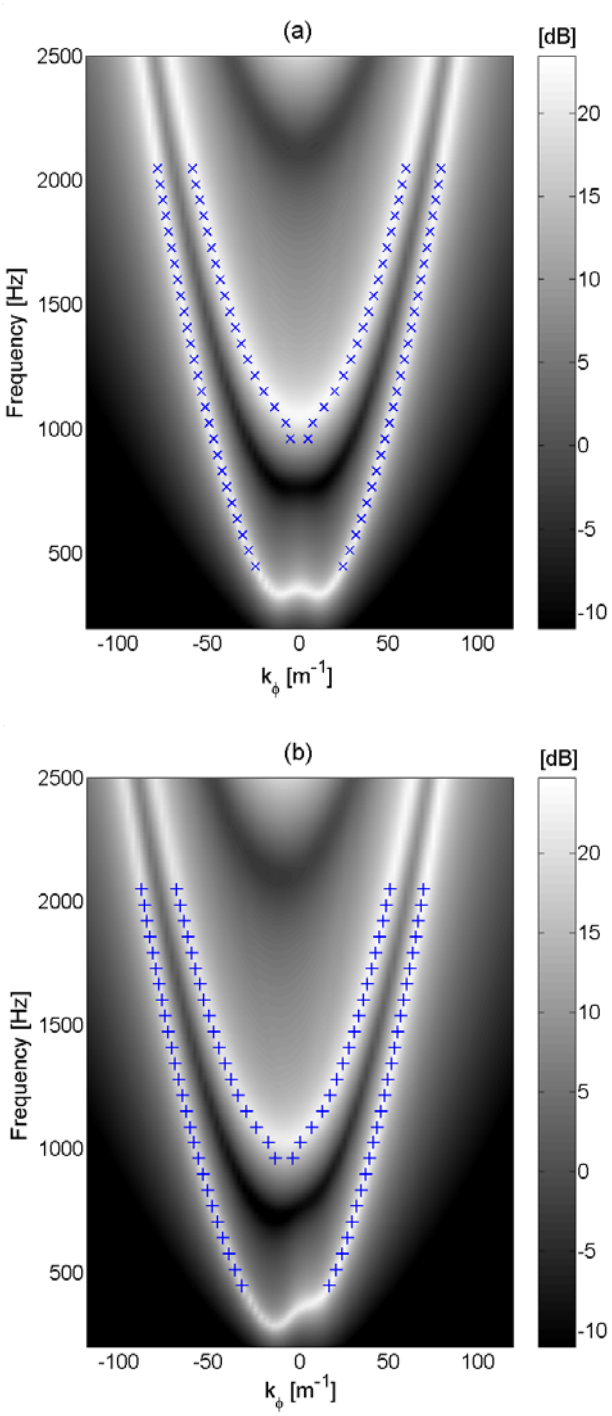


Figure 6.7: Real wave numbers (• and +) obtained from Prony series identification when $\xi = 0.05$: (a) stationary case ($\Omega = 0$ rad/s) and (b) rotating case ($\Omega = 100$ rad/s).

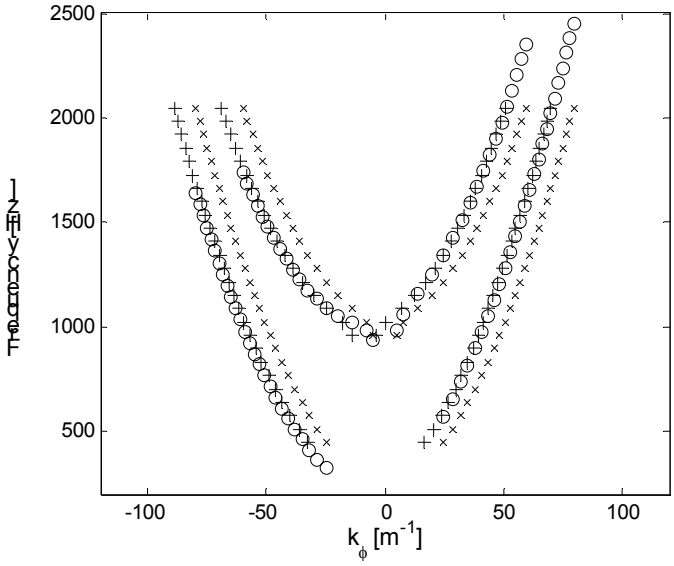


Figure 6.8: Compensation of stationary dispersions relations by using Eq. (32): • - stationary case, + - rotational case, and o - compensated case.

# 7. CONCLUSIONS

Multi-reference, scan-based NAH procedure was applied to a rolling tire: it has been shown that sound radiation originates close to the contact patch of the tire. These measurements were enabled by several new technologies. In particular, a compensation procedure for source non-stationarity was introduced and applied to the rolling tire experiment resulting in enhanced acoustical images in narrow frequency bands. In addition, a post-processing procedure was developed that makes it possible both to identify optimal reference microphone locations and to place virtual references at those locations. The latter procedure was successfully applied to separate sound radiation from the contact patch leading and trailing edges and the sidewall of the rolling tire.

Tire treadband vibration has been measured and studied by using wave decomposition techniques at frequencies below 1000 Hz. It has been concluded that tires can be effectively modeled as waveguides since the carcass vibration is controlled by no more than six propagating waves. It was also pointed out that a fast extensional wave mode that cuts-on at the circumferential ring frequency has the potential to radiate sound effectively owing to its relatively high phase speed.

For the purpose of identifying tire design parameters that can control tire vibration characteristics, circular cylindrical shell models and full tire models have been considered. These models were analyzed by using both 3-D finite elements and 2-D finite elements: a two-dimensional finite element method was developed to model a tire at low computational cost. It has been shown that by using the 2-D finite elements, both inflation pressure and composite material properties can be considered. It was also found that the tire models considered here successfully reproduce the major features of the experimental tire dispersion relations. Furthermore, two wave types that are known to contribute significantly to tire dynamic response could be identified in the tire models: flexural wave modes and a fast extensional wave mode that cuts-on at the circumferential ring frequency. It was also observed that fiber reinforcement of the treadband can account for the existence of modes having negative group speeds at small wave numbers.

Finally, the treadband of a tire was modeled as a rotating circular cylindrical shell in order to identify the effects of rotation. It has been shown that rotation has two principal effects: stiffening of the treadband and "tilting" of the dispersion curves. It has been found, however, that the rotational stiffening effect was not significant compared with the stiffening effect of inflation pressure at typical rotational speeds. In contrast, the kinematic tilting effect was found to be significant. Thus, it was concluded that a linear function could be used to adjust the stationary dispersion curve which could then be used to analyze the potential of a rotating tire to radiate sound.

In the future, rotation effects should also be implemented in the 2-D finite elements. The coupling effects between acoustical responses in the cavity of a tire and vibrational responses of the tire will also be considered. Based on the vibrational responses obtained from the coupled problem ananlysis, sound radiation from a tire can then be analyzed by using a boundary element method.

# LIST OF REFERENCES


1. W.A. Leasure and E.K. Bender, 1975, "Tire-road interaction noise," *Journal of the Acoustical Society of America*, Vol. 58, pp. 39-50.
2. U. Sandberg, 1982, "Will tire/road noise limit future vehicle noise reductions?" *Proceedings of Inter-Noise 82*, pp. 127-130.
3. J.S. Bolton, H.R. Hall, R.F. Schumacher, and J. Stott, 1995, "Correlation of tire intensity levels and passby sound pressure levels," *SAE Paper 951355*, *Proceedings of the SAE Noise and Vibration Conference*, pp. 981-989.
4. R.F. Schumacher, K.G. Phaneuf, and W.J. Haley, 1995, "SAE and ISO noise test site variability," *SAE Paper 951361*, *Proceedings of the SAE Noise and Vibration Conference*, pp. 1037-1044.
5. G. Rimondi, 1995, "Tire contribution in the context of automobile noise reduction," *Tire Science and Technology*, TSTCA 23, pp. 189-208.
6. M.G. Richards, 1974, "Automotive tire noise - a comprehensive study," *Sound and Vibration*, May 1974, pp. 42-47.
7. A.C. Eberhardt and W.F. Reiter, 1977, "Use of coherence and frequency response functions to locate and define vibration noise sources in rolling tires," *SAE Paper 770027*, *Society of Automotive Engineers*.
8. M. Jennewein and M. Bergmann, 1984, "Investigations concerning tyre/road noise sources and possibilities of noise reduction," Paper C150/84, *Proceedings of the Institute of Mechanical Engineering Conference - Vehicle Noise and Vibration*.
9. M. Heckl, 1986, "Tyre noise generation," *Wear*, Vol. 113, pp. 157-170.
10. P. M. Nelson, 1986, "Rubber tyre noise generation," *Wear*, Vol. 113, pp. 171-174.
11. P.R. Donavan, 1993, "Tire-pavement interaction noise measurement under vehicle operating conditions of cruise and acceleration," *SAE Paper 931276*, *Proceedings of the SAE Noise and Vibration Conference*, pp. 113-123.
12. U. Sandberg and J.A. Ejsmont, 2002, *Tire/Road Noise Reference Book*, INFORMEX, Harg, SE-59040 Kisa, Sweden.

13. R.C. Chanaud, 1969, “Experimental study of aerodynamic sound from a rotating disc,” *Journal of the Acoustical Society of America*, Vol. 45(2), pp. 392-397.
14. R.E. Hayden, 1971, “Roadside noise from the interaction of a rolling tire with the road surface,” *Proceedings of the Purdue Noise Control Conference*, pp. 62-67.
15. J.A. Ejsmont, 1984, “Influence of tread on tire/road noise,” *SAE paper 841238*, *Society of Automotive Engineers*.
16. F.E. Timmons, 1976, “An industry viewpoint of tire sound reduction and measurement methodology,” *SAE Paper 762020*, *Proceedings of SAE Highway Tire Noise Symposium*, *Society of Automotive Engineers*.
17. J.A. Ejsmont, 1990, “Side force influence on tire/road noise,” *Proceedings of International Tire/Road Noise Conference 90*.
18. O. Bschorr, 1985, “Reduction of tire noise,” *Proceedings of Inter-Noise 85*, pp. 271-274.
19. R.W. Scavuzzo, L.T. Charek, P.M. Sandy, and G.D. Shteinhauz, 1994, “Influence of wheel resonance on tire acoustic cavity noise, *SAE Paper 940533*, *Proceedings of the SAE Noise and Vibration Conference*.
20. W. Kropp, F.X. Becot, and S. Barrelet, 2000, “On the sound radiation from tyres,” *Acustica*, Vol. 86, pp. 769-779.
21. L. Cremer, M. Heckl, and E.E. Ungar, 1988, *Structure-Borne Sound*, 2nd Ed., Springer-Verlag, Berlin.
22. W. Soedel, 1975, “On the dynamic response of rolling tires according to thin shell approximations,” *Journal of Sound and Vibration*, Vol. 41, pp. 233-246.
23. M. Hirano and T. Akasaka, 1976, “Natural frequencies of the bias tire,” *Tire Science and Technology*, TSTCA 4, pp. 86-114.
24. T. Akasaka and K. Kabe, 1977, “Deformation and cord tension of a bias tire in contact with the road,” *Tire Science and Technology*, TSTCA 5, pp. 171-201.
25. R.F. Keltie, 1982, “Analytical model of the truck tire vibration sound mechanism,” *Journal of the Acoustical Society of America*, Vol. 71(2), pp. 359-367.
26. S. Saigal, T.Y. Yang, H.W. Kim, and W. Soedel, 1986, “Free vibrations of a tire as a toroidal membrane,” *Journal of Sound and Vibration*, Vol. 107, pp. 71-82.
27. T.G. Clapp and A.C. Eberhardt, 1987, “Incorporating the effects of tread pattern in a dynamic tire excitation mechanism,” *Transportation Research Record 1117*, pp. 114-120.
28. E. Vinesse and H. Nicollet, 1988, “Surface waves on the rotating tyre: an application of functional analysis,” *Journal of Sound and Vibration*, Vol. 126, pp. 85-

96.

29. W. Kropp, 1989, “Structure-borne sound on a smooth tyre,” *Applied Acoustics*, Vol. 26, pp. 181-192.
30. S.C. Huang, 1992, “The vibration of rolling tyres in ground contact,” *International Journal of Vehicle Design*, Vol. 13, pp. 78-95.
31. J.M. Cuschieri, S. Gregory, and M. Tournour, 1996, “Open grid bridge noise from grid and tire vibrations,” *Journal of Sound and Vibration*, Vol. 190, pp. 317-343.
32. P. Bremner, J. Huff, and J.S. Bolton, 1997, “A model study of how tire construction and materials affects vibration-radiated noise,” *SAE Paper 972049*, *Proceedings of the SAE Noise and Vibration Conference*, pp. 1415-1422.
33. J.S. Bolton and Y.-J. Kim, 2000, “Wave number domain representation of tire vibration,” *Paper 713*, *Proceedings of Inter-Noise 2000*, Vol. 1, pp. 184-190.
34. Y.-J. Kim and J.S. Bolton, 2001, “Modeling tire treadband vibration,” *Paper 716*, *Proceedings of Inter-Noise 2001*.
35. Y.-J. Kim and J.S. Bolton, 2002, “Effect of Rotation on the Vibration Characteristics of Tires,” *Paper 434*, *Proceedings of Inter-Noise 2002*.
36. J.D. Maynard, E.G. Williams, and Y. Lee, 1985, “Nearfield Acoustical Holography: I. Theory of Generalized Holography and the Development of NAH,” *Journal of the Acoustical Society of America*, Vol. 74(4), pp. 1395-1413.
37. H.-S. Kwon, Y.-J. Kim, and J.S. Bolton, 2002, “Compensation for source non-stationarity in multi-reference, scan-based Nearfield Acoustical Holography,” *Paper 436*, *Proceedings of Inter-Noise 2002*.
38. H.-S. Kwon, Y.-J. Kim, and J.S. Bolton, 2003, “Compensation for source non-stationarity in multi-reference, scan-based Nearfield Acoustical Holography,” *Journal of the Acoustical Society of America*, Vol. 113, pp. 360-368.
39. H.-S. Kwon and J.S. Bolton, 1998, “Partial field decomposition in Nearfield Acoustical Holography by the use of singular value decomposition and partial coherence procedures,” *Proceedings of Noise-Con 98*, pp. 649-654.
40. J. Hald, 1988, *STSF - A Unique Technique for Scan-Based Nearfield Acoustical Holography without Restriction on Coherence*, B&K Technical Review No. 1.
41. D.L. Hallman and J.S. Bolton, 1994, “A comparison of multi-reference Nearfield Acoustical Holography procedures,” *Proceedings of Noise-Con 94*, pp. 929-934.
42. F.J. Fahy, 1989, *Sound and Structural Vibration*, corrected paper back edition, Aca demic Press, London.

43. J.S. Bolton, H.J. Song, Y.K. Kim, and Y.J. Kang, 1998, "The wave number decom position approach to the analysis of tire vibration," *Proceedings of Noise-Con 98*, pp. 97-102.
44. F.B. Hildebrand, 1956, *Introduction to Numerical Analysis*, McGraw-Hill, New York.
45. P. Davies and J.K. Hammond, 1984, "A comparison of Fourier and parametric methods for structural system identification," *Journal of Vibration Acoustics Stress and Reliability in Design*, Vol. 106, pp. 40-48.
46. S. Braun and Y.M. Ram, 1987, "Determination of structural modes via the Prony model: System order and noise induced poles," *Journal of the Acoustical Society of America*, Vol. 81, pp. 1447-1459.
47. K. Grosh and E.G. Williams, 1993, "Complex wave-number decomposition of structural vibrations," *Journal of the Acoustical Society of America*, Vol. 93, pp. 836-848.
48. C.W. Therrien and C.H. Velasco, 1995, "An iterative Prony method for ARMA signal modeling," *IEEE Transactions on Signal Processing*, Vol. 43, pp. 358-361.
49. Y.-J. Kim, J.S. Bolton, S.-Y. Lee, and Y.J. Kang, 2000, "Identification of complex dispersion relations in cylindrical, foam-lined ducts," *Proceedings of the Korean Society for Noise and Vibration Engineering*, pp. 1729-1734.
50. J.G. McDaniel and W.S. Shepard, Jr., 2000, "Estimation of structural wave numbers from spatially sparse response measurements," *Journal of the Acoustical Society of America*, Vol. 108(4), pp. 1674-1682.
51. R.J. Pinnington and A.R. Briscoe, 2001, "A wave model for a pneumatic tyre belt", *Journal of Sound and Vibration*, Vol. 253(5), pp. 941-959.
52. W. Soedel, 1993, *Vibrations of Shells and Plates*, 2nd Ed., Marcel Dekker Inc.
53. S.C. Huang and W. Soedel, 1988, "Effects of Coriolis acceleration on the forced vibration of rotating cylindrical shells," *Journal of Applied Mechanics*, Vol. 55, pp. 231-233.
54. E. Vinesse and H. Nicollet, 1988, "Surface waves on the rotating tyre: An application of functional analysis," *Journal of Sound and Vibration*, Vol. 126(1), pp. 85-96.
55. M.S. Kompella, P. Davies, R.J. Bernhard, and D.A. Ufford, 1994, "A technique to determine the number of incoherent sources contributing to the response of a system," *Mechanical Systems and Signal Processing*, Vol. 8(4), pp. 363-380.
56. K.-U. Nam and Y.-H. Kim, 2001, "Visualization of multiple incoherent sources by

the backward prediction of near-field acoustic holography," *Journal of the Acoustical Society of America*, Vol. 109(5), pp. 1808-1816.

57. J.M. Danthez and R. Aquilina, 1997, "Separation of broadband sources processing concept of the Labrador software," *Mechanical Systems and Signal Processing*, Vol. 11, pp. 91-106.
58. S. Finnveden, 1997, "Spectral finite element analysis of the vibration of straight fluid-filled pipes with flanges," *Journal of Sound and Vibration*, Vol. 199(1), pp. 125-153.
59. Y.-J. Kim and J.S. Bolton, 2003, "Effects of rotation on the dynamics of a circular cylindrical shell with application to tire vibration," in press, *Journal of Sound and Vibration*.
60. G. Strang, 1993, *Linear Algebra and Its Application*, 3rd Ed., Prentice-Hall.
61. D.H. Johnson and D.E. Dudgeon, 1993, *Array Signal Processing: Concepts and Techniques*, Prentice-Hall.
62. Y.-J. Kim, J.S. Bolton, and H.-S. Kwon, 2003, "Partial sound field decomposition in multi-reference Nearfield Acoustical Holography by using optimally-located virtual references," manuscript submitted to *Journal of the Acoustical Society of America* for publication.
63. Y.K. Cheung, 1976, *Finite Strip Method in Structural Analysis*, Pergamon Press.
64. T.L. Richards, 1991, "Finite element analysis of structural-acoustic coupling in tyres," *Journal of Sound and Vibration,* Vol. 149, pp. 235-243.
65. R.A. Brockman, J.H. Champion, and J.P. Medzorian, 1992, "Finite element analysis of tire critical speeds," *Computers and Structures*, Vol. 43, pp. 581-593.
66. C.-M. Nilsson and S. Finnveden, 2002, "Tyre vibration analysis with conical waveguide finite elements," *Proceedings of Inter-Noise 2002*.
67. J.N. Reddy, 1993, *Finite Element Method*, 2nd Ed., McGraw Hill, Inc.
68. J. Padovan, 1973, "Natural frequencies of rotating prestressed cylinders," *Journal of Sound and Vibration*, Vol. 31(4), pp. 469-482.
69. S.C. Huang and W. Soedel, 1987, "Effects of Coriolis acceleration on the free and forced in-plane vibrations of rotating rings on elastic foundation," *Journal of Sound and Vibration*, Vol. 115(2), pp. 253-274.
70. S.C. Huang and W. Soedel, 1987, "Response of rotating rings to harmonic and periodic loading and comparison with the inverted problem," *Journal of Sound and Vibration*, Vol. 118(2), pp. 253-270.

## Appendix A

Expressions for the strains of thin shells are derived in Ref. [43] and they are presented here for completeness. They can be separated in terms of membrane strains and bending strains: i.e.,

$$\varepsilon_{11} = \varepsilon_{11}^0 + x_3\kappa_{11}, \tag{A1}$$

$$\varepsilon_{22} = \varepsilon_{22}^0 + x_3\kappa_{22}, \tag{A2}$$

and

$$\varepsilon_{12} = \varepsilon_{12}^0 + x_3\kappa_{12}, \tag{A3}$$

where the membrane strains are

$$\varepsilon_{11}^0 = \frac{1}{A_1}\frac{\partial u_1}{\partial x_1} + \frac{u_2}{A_1A_2}\frac{\partial A_1}{\partial x_2} + \frac{u_3}{R_1} + \frac{1}{2A_1^2}\left(\frac{\partial u_3}{\partial x_1}\right)^2, \tag{A4}$$

$$\varepsilon_{22}^0 = \frac{1}{A_2}\frac{\partial u_2}{\partial x_2} + \frac{u_1}{A_1A_2}\frac{\partial A_2}{\partial x_1} + \frac{u_3}{R_2} + \frac{1}{2A_2^2}\left(\frac{\partial u_3}{\partial x_2}\right)^2, \tag{A5}$$

$$\varepsilon_{12}^0 = \frac{A_2}{A_1}\frac{\partial}{\partial x_1}\left(\frac{u_2}{A_2}\right) + \frac{A_1}{A_2}\frac{\partial}{\partial x_2}\left(\frac{u_1}{A_1}\right) + \frac{1}{A_1A_2}\left(\frac{\partial u_3}{\partial x_1}\right)\left(\frac{\partial u_3}{\partial x_2}\right), \tag{A6}$$

the bending strains are

$$\kappa_{11} = \frac{1}{A_1}\frac{\partial \beta_1}{\partial x_1} + \frac{\beta_2}{A_1A_2}\frac{\partial A_1}{\partial x_2}, \tag{A4}$$

$$\kappa_{22} = \frac{1}{A_2}\frac{\partial \beta_2}{\partial x_2} + \frac{\beta_1}{A_1A_2}\frac{\partial A_2}{\partial x_1}, \tag{A5}$$

$$\kappa_{12} = \frac{A_2}{A_1}\frac{\partial}{\partial x_1}\left(\frac{\theta_2}{A_2}\right) + \frac{A_1}{A_2}\frac{\partial}{\partial x_2}\left(\frac{\theta_1}{A_1}\right), \tag{A6}$$

and the rotational displacements are

$$\beta_1 = \frac{u_1}{R_1} - \frac{1}{A_1}\frac{\partial u_3}{\partial x_1}, \tag{A7}$$

and

$$\beta_2 = \frac{u_2}{R_2} - \frac{1}{A_2}\frac{\partial u_3}{\partial x_2}, \tag{A8}$$

where $A_m$ and $R_m$ are the radius of curvature and Lamé parameter, respectively, in the $x_m$-direction. The quadratic, non-linear terms at the end of the membrane strain expressions are presented for the purpose of accommodating the case in which large initial stresses are present.

## Appendix B

Expressions for the normal and shear forces are derived in Ref. [43] and they are presented here for completeness. The in-plane forces are expressed as

$$N_{xx} = K(\varepsilon_{xx}^0 + \nu\varepsilon_{\theta\theta}^0) \tag{B1}$$

$$N_{x\theta} = \frac{K(1-\nu)}{2}\varepsilon_{x\theta}^0 \tag{B2}$$

$$N_{\theta\theta} = K(\varepsilon_{\theta\theta}^0 + \nu\varepsilon_{xx}^0), \tag{B3}$$

where the membrane strains are

$$\varepsilon_{xx}^0 = \frac{\partial u_x}{\partial x} \tag{B4}$$

$$\varepsilon_{x\theta}^0 = \frac{\partial u_\theta}{\partial x} + \frac{1}{a}\frac{\partial u_x}{\partial \theta} \tag{B5}$$

$$\varepsilon_{\theta\theta}^0 = \frac{u_r}{a} + \frac{1}{a}\frac{\partial u_\theta}{\partial \theta}. \tag{B6}$$

The shear forces are represented in terms of moments: i.e.,

$$Q_{xr} = \frac{\partial M_{xx}}{\partial x} + \frac{1}{a}\frac{\partial M_{x\theta}}{\partial \theta} \tag{B4}$$

$$Q_{\theta r} = \frac{\partial M_{x\theta}}{\partial x} + \frac{1}{a}\frac{\partial M_{\theta\theta}}{\partial \theta}, \tag{B5}$$

where the moments can be expressed in terms of curvatures as

$$M_{xx} = D(\kappa_{xx} + \nu\kappa_{\theta\theta}) \tag{B6}$$

$$M_{x\theta} = \frac{D(1-\nu)}{2}\kappa_{x\theta} \tag{B7}$$

$$M_{\theta\theta} = D(\kappa_{\theta\theta} + \nu\kappa_{xx}), \tag{B8}$$

and where the curvatures are expressed in terms of rotation angles as

$$\kappa_{xx} = -\frac{\partial \beta_x}{\partial x} \tag{B9}$$

$$\kappa_{x\theta} = \frac{\partial \beta_\theta}{\partial x} + \frac{1}{a}\frac{\partial \beta_x}{\partial \theta} \tag{B10}$$

$$\kappa_{\theta\theta} = \frac{1}{a}\frac{\partial \beta_\theta}{\partial \theta}, \tag{B11}$$

and

$$\beta_x = -\frac{\partial u_r}{\partial x} \tag{B12}$$

$$\beta_\theta = \frac{u_\theta}{a} - \frac{1}{a}\frac{\partial u_r}{\partial \theta}. \tag{B13}$$

## Appendix C

Expressions for the normal and shear forces in local coordinates were derived in Ref. [43]. They can also be used in Eqs. (6.5) to (6.7) described in the reference frame when the circumferential angle, $\theta$, in local coordinates is replaced by the circumferential angle, $\phi$, in global coordinates. Then the in-plane forces are expressed as

$$N_{xx} = K(\varepsilon_{xx}^0 + \nu\varepsilon_{\phi\phi}^0) \tag{C1}$$

$$N_{x\phi} = \frac{K(1-\nu)}{2}\varepsilon_{x\phi}^0 \tag{C2}$$

$$N_{\phi\phi} = K(\varepsilon_{\phi\phi}^0 + \nu\varepsilon_{xx}^0)\,, \tag{C3}$$

where the membrane strains are

$$\varepsilon_{xx}^0 = \frac{\partial u_x}{\partial x} \tag{C4}$$

$$\varepsilon_{x\phi}^0 = \frac{\partial u_\phi}{\partial x} + \frac{1}{a}\frac{\partial u_x}{\partial \phi} \tag{C5}$$

$$\varepsilon_{\phi\phi}^0 = \frac{u_r}{a} + \frac{1}{a}\frac{\partial u_\phi}{\partial \phi}\,. \tag{C6}$$

The shear forces are represented in terms of moments: i.e.,

$$Q_{xr} = \frac{\partial M_{xx}}{\partial x} + \frac{1}{a}\frac{\partial M_{x\phi}}{\partial \phi} \tag{C4}$$

$$Q_{\phi r} = \frac{\partial M_{x\phi}}{\partial x} + \frac{1}{a}\frac{\partial M_{\phi\phi}}{\partial \phi}\,, \tag{C5}$$

where the moments can be expressed in terms of curvatures as

$$M_{xx} = D(\kappa_{xx} + \nu\kappa_{\phi\phi}) \tag{C6}$$

$$M_{x\phi} = \frac{D(1-\nu)}{2}\kappa_{x\phi} \tag{C7}$$

$$M_{\phi\phi} = D(\kappa_{\phi\phi} + \nu\kappa_{xx})\,. \tag{C8}$$

In Eqs. (C6) to (C8), the curvatures are expressed in terms of rotation angles as

$$\kappa_{xx} = -\frac{\partial \beta_x}{\partial x} \tag{C9}$$

$$\kappa_{x\phi} = \frac{\partial \beta_\phi}{\partial x} + \frac{1}{a}\frac{\partial \beta_x}{\partial \phi} \tag{C10}$$

$$\kappa_{\phi\phi} = \frac{1}{a}\frac{\partial \beta_\phi}{\partial \phi}, \tag{C11}$$

and

$$\beta_x = -\frac{\partial u_r}{\partial x} \tag{C12}$$

$$\beta_\phi = \frac{u_\phi}{a} - \frac{1}{a}\frac{\partial u_r}{\partial \phi}. \tag{C13}$$

## Appendix D

In the hybrid, 2-D FE formulation, the in-plane displacements, $u_1$ and $u_2$, are approximated by using linear polynomials (i.e., Lagrange linear interpolation functions [67]) while the surface normal displacement, $u_3$, was represented by cubic polynomials (i.e., Hermite cubic interpolation functions [67]) which are normally used for the finite element formulation of an Euler-Bernoulli beam: i.e.,

$$u_1 = \chi_{11} u_{11} + \chi_{12} u_{12}, \tag{C1}$$

$$u_2 = \chi_{21} u_{21} + \chi_{22} u_{22}, \tag{C2}$$

and

$$u_3 = \chi_{31} u_{31} + \chi_{41} \beta_{11} + \chi_{32} u_{32} + \chi_{42} \beta_{12}. \tag{C3}$$

By using a linear coordinate transform, the $x_1$-axis ($x_1$ = 0 to $L$) can be mapped onto the $\zeta$-axis ($\zeta$ = -1 to 1): i.e.,

$$\zeta = \frac{2}{L} x_1 - 1. \tag{C4}$$

Since the two nodes of an element are located at $\zeta$ = -1 and $\zeta$ = 1, as shown in Fig. 5.1, the interpolation functions are [67]

$$\chi_{11} = 1/2(1-\zeta), \tag{C5}$$

$$\chi_{12} = 1/2(1+\zeta), \tag{C6}$$

$$\chi_{21} = \chi_{11}, \tag{C7}$$

$$\chi_{22} = \chi_{12}, \tag{C8}$$

$$\chi_{31} = 1 - 3[(1+\zeta)/2]^2 + 2[(1+\zeta)/2]^3, \tag{C9}$$

$$\chi_{41} = -(1+\zeta)[1-(1+\zeta)/2]^2, \tag{C10}$$

$$\chi_{32} = 3[(1+\zeta)/2]^2 - 2[(1+\zeta)/2]^3, \tag{C11}$$

and

$$\chi_{42} = (1+\zeta)[\{(1+\zeta)/2\}^2 - (1+\zeta)/2]. \tag{C12}$$

By substituting Eq. (C4) into Eqs. (C5) to (C12), the interpolation functions can be represented in terms of $x_1$.